Strojniški vestnik

Journal of Mechanical Engineering

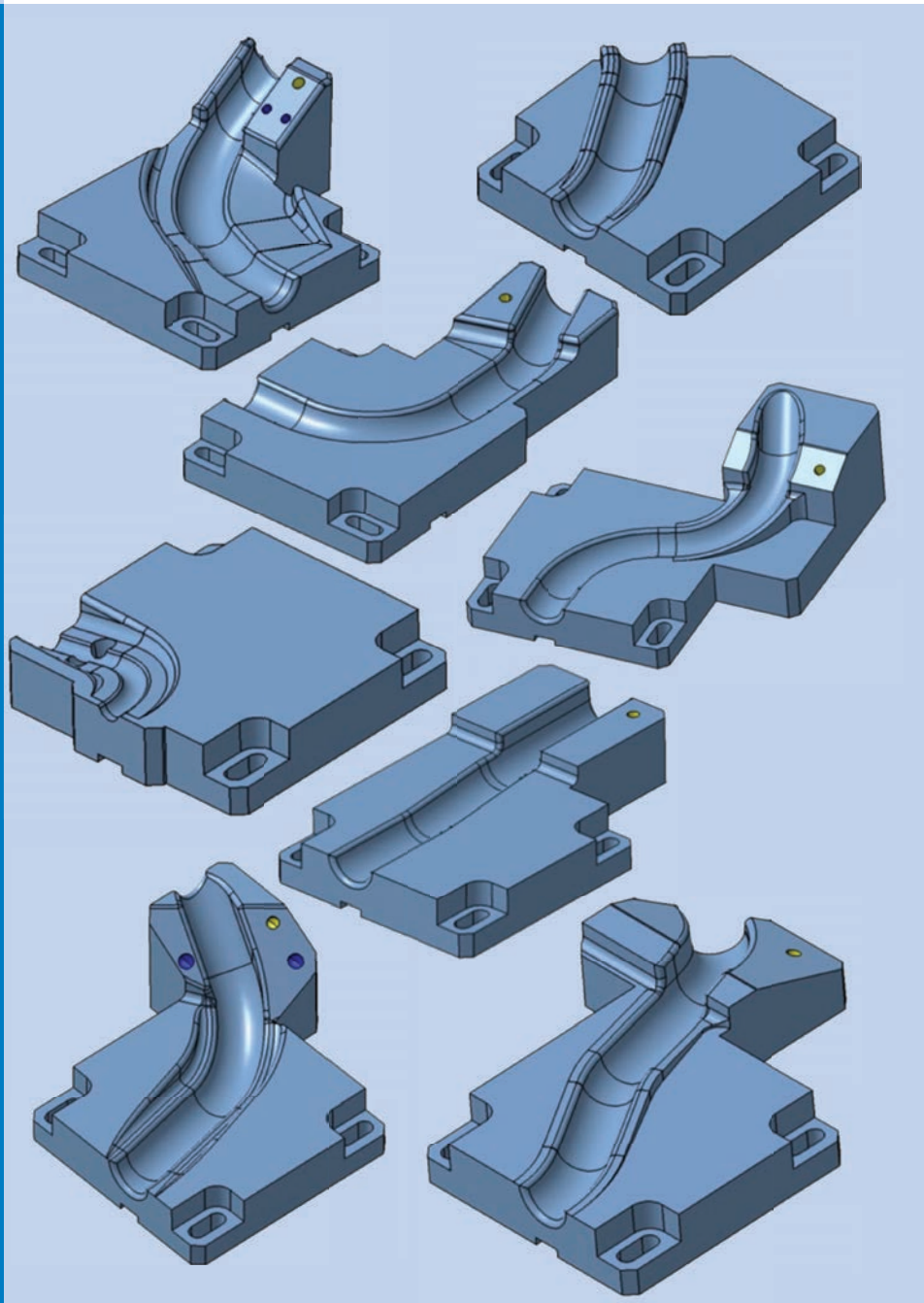

no. 10
year 2021
volume 67

Strojniški vestnik – Journal of Mechanical Engineering (SV-JME)

Aim and Scope

The international journal publishes original and (mini)review articles covering the concepts of materials science, mechanics, kinematics, thermodynamics, energy and environment, mechatronics and robotics, fluid mechanics, tribology, cybernetics, industrial engineering and structural analysis.

The journal follows new trends and progress proven practice in the mechanical engineering and also in the closely related sciences as are electrical, civil and process engineering, medicine, microbiology, ecology, agriculture, transport systems, aviation, and others, thus creating a unique forum for interdisciplinary or multidisciplinary dialogue.

The international conferences selected papers are welcome for publishing as a special issue of SV-JME with invited co-editor(s).

Editorial Office
University of Ljubljana, Faculty of Mechanical Engineering
SV-JME, Aškerčeva 6, SI-1000 Ljubljana, Slovenia
Phone: 386 (0)1 4771 137
Fax: 386 (0)1 2518 567
info@sv-jme.eu, http://www.sv-jme.eu

Print: Demat d.o.o., printed in 250 copies

Founders and Publishers
University of Ljubljana, Faculty of Mechanical Engineering, Slovenia
University of Maribor, Faculty of Mechanical Engineering, Slovenia
Association of Mechanical Engineers of Slovenia
Chamber of Commerce and Industry of Slovenia, Metal Processing Industry Association

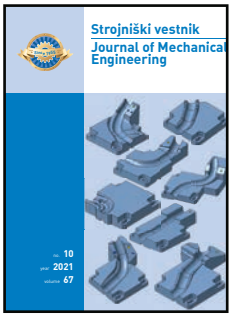

Cover: The issue of intelligent production of special production tooling is one of the topics that relate to the Smart Factory paradigm. Using knowledge engineering techniques and advanced CAM system tools, it becomes possible to automate the process of preparing a machining program for entire families of similar products. The image shows the special tooling family - assembly equipment for plastic pipes, for which a method of automatic CAM programming, called ACPUT, was developed. The paper aims to present results of testing the effectiveness of the use of ACPUT by technicians with different levels of experience (expert and beginner).

Image Courtesy: Maciej Kowalski, MK-Tech Company, Poland, and Przemysław Zawadzki, Phd, Poznan University of Technology, Faculty of Mechanical Engineering, Poland

General information

Strojniški vestnik – Journal of Mechanical Engineering is published in 11 issues per year (July and August is a double issue).

Institutional prices include print & online access: institutional subscription price and foreign subscription €100,00 (the price of a single issue is €10,00); general public subscription and student subscription €50,00 (the price of a single issue is €5,00). Prices are exclusive of tax. Delivery is included in the price. The recipient is responsible for paying any import duties or taxes. Legal title passes to the customer on dispatch by our distributor. Single issues from current and recent volumes are available at the current single-issue price. To order the journal, please complete the form on our website. For submissions, subscriptions and all other information please visit: *http://www.sv-jme.eu.*

You can advertise on the inner and outer side of the back cover of the journal. The authors of the published papers are invited to send photos or pictures with short explanation for cover content.

We would like to thank the reviewers who have taken part in the peer-review process.

ISSN 0039-2480, ISSN 2536-2948 (online)

The journal is subsidized by Slovenian Research Agency.

Strojniški vestnik - Journal of Mechanical Engineering is available on *https://www.sv-jme.eu.*

Contents

Strojniški vestnik - Journal of Mechanical Engineering
volume 67, (2021), number 10
Ljubljana, October 2021
ISSN 0039-2480

Published monthly

Papers

Strojniški vestnik - Journal of Mechanical Engineering 67(2021)10, 475-488
DOI:10.5545/sv-jme.2021.7285
Original Scientific Paper
Received for review: 2021-05-28
Received revised form: 2021-08-17
Accepted for publication: 2021-08-18

Effectiveness of Automatic CAM Programming Using Machining Templates for the Manufacture of Special Production Tooling

Maciej Kowalski[1,2] – Przemysław Zawadzki[1,*] – Adam Hamrol[1]
[1] Poznan University of Technology, Faculty of Mechanical Engineering, Poland
[2] MK-Tech Company, Poland

The paper presents the methodology and implementation of original Automatic CAM programming using machining templates (ACPUT) dedicated to manufacturing special technological tooling. The development of ACPUT was inspired by the observation that although modern computer-aided design (CAD) / computer-aided manufacturing (CAM) systems can automatically create CAM programs, their universality makes them both difficult to use and inefficient because the programs created this way often contain errors. The presented programming procedure includes the development of specific machining templates based on technological knowledge gathered in a specially prepared database. These templates are dedicated to a group of parts characterized by the similarity of their geometric features. ACPUT makes it possible to reduce(in comparison to traditional CAM programming) the time required to develop a machining program, thereby positively impacting the total cost of tooling production. The paper aims to present results of testing the effectiveness of the use of ACPUT by technicians with different levels of experience (expert and beginner). The tests were carried out on special tooling - assembly equipment for plastic pipes, and compared program preparation time, machining time, and production costs.

Keywords: generative CAM process, CNC programming, technology design automation, knowledge-based engineering

Highlights

- *Automatic CAM programming using machining templates (ACPUT) is dedicated to the manufacture of special technological tooling that consists of technologically similar parts.*
- *ACPUT makes it possible to shorten the time needed to develop a machining program and to reduce the total cost of tooling production.*
- *The effectiveness of the ACPUT procedure depends on the experience of programmers preparing the machining templates.*

0 INTRODUCTION

Nowadays, manufacturing companies must respond quickly to diverse and dynamically changing market needs and expectations. This situation is related to, among other factors, the increasingly common personalization of products, which requires rapid responses to changes in demand in terms of volume and assortment while maintaining high product quality and highly efficient production processes **[1]** to **[3]**.

To meet the expectations of the mass personalization of products, it is necessary to develop systems that allow for the extensive use of various data contained in product designs and their production technologies **[4]** to **[6]**. Such systems,including functions ensuring efficient data exchange between departments involved in production preparation, have been a standard in mass personalization-oriented companies for many years **[7]** and **[8]**. In addition, designers and technicians can use tools that make it possible to use the knowledge gained in previously implemented projects (i.e., knowledge-based engineering (KBE)) **[9]** and **[10]**. Examples of this are found in the automotive sector, household appliances, sanitary and electronic products, and other industry sectors where similar components with the same purpose may differ due to different vehicle variants.

One of the stages to prepare for product manufacture is the design and implementation of special technological tooling, which complements the standard equipment of production machines and equipment and is essential for manufacturing products whose design specifics need to be considered. Due to their intended use, universal (general purpose) and special (dedicated to specific machines, processes, and products) equipment can be distinguished **[10]** to **[12]**.

The production of special technological tooling is an example of custom-made production, asmake-to-order (MTO) and engineering to order (ETO), in which the design of the device is based on the product model provided by the customer.

The process of production special technological tooling is carried out in stages and includes (Fig. 1):

1. Analysis of the three-dimensional (3D) CAD model of the product provided by the customer.
2. Development of a tooling model in the 3D CAD program adapted to the product's shape.
3. Export of designed 3D CAD models of tooling to the CAM program.

*Corr. Author's Address: Poznan University of Technology, Piotrowo St. 3, 60-965 Poznan, Poland, przemyslaw.zawadzki@put.poznan.pl

4. Development of machining programs in CAM for individual parts of the tooling.
5. Manufacture of tooling parts on a computer numerical control (CNC) machine.
6. Tooling assembly and delivery to the customer.

This process is time-consuming and quite often inefficient (in the case of manufacturing groups of products) because despite containing similar manufacturing actions, it must be carried out for each unique product model separately [13].

Using previously acquired engineering knowledge, advanced parametric design methods in CAD systems make it possible to create special models, known as "generative models" in the literature. Such models enable the automation of the operations in Stages 1 and 2 (Fig. 1) related to the development of the tooling design.

Based on this approach in a small Polish company (MK-Tech Company), designing and producing special equipment for advanced technical companies from the automotive industry, a procedure for creating machining templates in the CAM system - Automatic CAM Programming Using Machining Templates (ACPUT) [14] was developed, which, in conjunction with a machining knowledge base, makes it possibleto automate the operations in stage 4 (Fig. 1). Since the ACPUT method is limited to a specified product group, the rules it creates are effective and efficient. The templates can be developed using any integrated CAD/CAM class software that allows the parametric construction of CAD models and programming in a scripting language (e.g., Visual Basic for applications (VBA).Sincemachine programming in CAM systems is a time-consuming and high-cost process (it requires the involvement of highly qualified engineering staff), the aimof the ACPUT was to reduce time and minimize human participation in the programming of CNC machines (in the manufactureof special production equipment).

This work aims to describe the basic properties of ACPUT and to present results of its testing on effectiveness and efficiency in relation to traditional programming of CNC machines.It should be emphasized that ACPUT is theprocedure of implementation of CAM programming automation, not a specific information system (IT) tool, so the essence of the tests was to compare it with the traditional programming approach (realized by technicians/CAM programmers), who can use any tools and methods in their work, evenfeature recognition (FR) [15] or well-known group technology (GT) assumptions [16].

1 PROGRAMMING IN CAM SYSTEMS

Generally, regardless of the type of CAM software used, programming in CAM systems can be divided into tasks relating to:

1. the definition of the workpiece shape,
2. the determination of subsequent machining operations,
3. the simulation and verification of the machining program.

In the beginning, the general geometric features are defined (i.e., the shape of the workpiece and the shape of the blank from which the part will be made). The user also defines his coordinate system with the zero position so that it is possible to orient the workpiece in the working space of the CNC machine.

The programming process involves determining the course of the machining process, depending on the complexity of the workpiece and its size. In individual machining operations, the technological engineer determines:

- the specific geometric elements of the CAD model for processing (planes, edges, points),
- the machining tool type and features,
- the machining strategy determining the machining tool path,

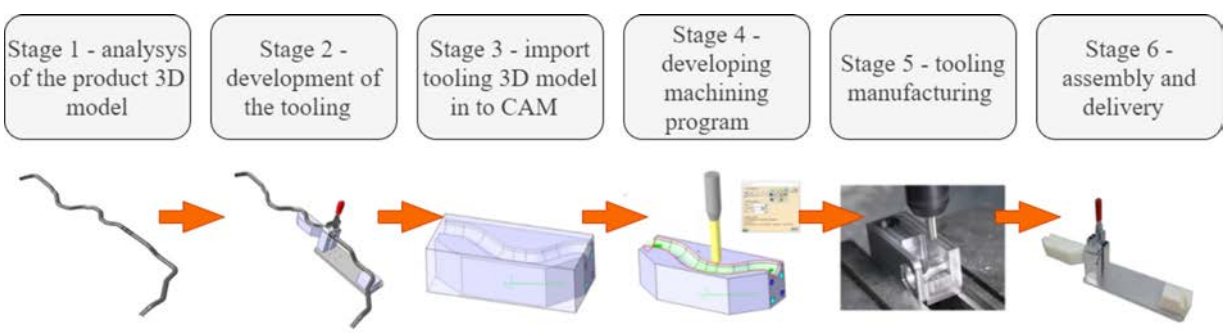

Fig. 1. *Example of special production tooling manufacture according to ETO* [14]

- the technological parameters of the operation (speeds and the input/output paths of the machining tool relative to the workpiece).

All the settings must undergo initial verification and evaluation in the CAM program (in order to detect possible errors at the operational level). Then, the tool path for the specific operation is generated and saved in the part's program structure. This process is repeated separately for each operation, andthe geometric changes resulting from previously generated operations are considered. Finally, the whole process is simulated, and if the program requires corrections, the necessary changes are made in the selected operations. After verification, using a special translator, the so-called postprocessor creates a numerical control (NC) code that will be implemented on a specific machine tool.

The level of effectiveness of programming CAM depends on the opportunity to develop dedicated solutions to support and automation presented above sequence of activities. Most often, it is carried out using specific tools of the given CAM program (most recent systems offersuch functions). The most popular functions are based on recognizing the characteristic features of a CAD model FR and assigning appropriate machining cycles to them [17]. In practice, these tools can accelerate the work on program preparation but are only effective for models with relatively simple shapes. In the case of advanced surface models (such as the forms with shaping cavities described in this article), the proportion of automatic recognition of geometric features decreases, and the "manual" work of the technician increases to a large extent. These tools are, therefore, a hybrid solution that works well in a single case. Therefore, for a group of families of similar products (several to several dozen items), their use does not significantly affect the effectiveness of the CAM programming process.

Although the FR technology has been known for three decades, it remains the subject of various works [18]. The authors focus on the development of various algorithms that can more accurately analyse 3D models and more effectively indicate possible technological operations [19] and [20]. In turn, Zhou et al. [21] presented the FR method (supported by deep learning) for the selection of cutting tools, increasing the effectiveness and efficiency of this task. Another example is the use of FR for spot welding recognition. It should be noted that these works do not deal with the issue of the automation of CAM programming in a general perspective, which can actually improve the efficiency of this process, but only develops algorithms for searching for specific geometric features of 3D models.

Moreover, analysing the literature relating to the programming of CNC machines, it can be seen that not much attention has beenpaid to methods forautomating of CAM programming process. Most recent research mainly concerns the improvement of the manufacturing process itself.An example would be the study by Andrankaja et al. [22], in which the decision support method in CAD/CAM design is described based on analysis of the data recorded in the NC code. In the opinion of Zhou and Wu [23], an important problem is the exchange of data between different CAD and CAM systems. They focused their attention on developing a method supporting a data exchange between various CAD/CAM systems, based on the "stl" universal data format. This means that their studyconcerns the third stage of programming related to data export within the process.

De Lacalle et al. [24] and [25] have presented methods for improving the CAM generation process in the production of special tooling (forging dies and injection moulds) according to high-speed milling (HSM) requirements. The main objective was to achieve a good surface quality directly from machining, without any additional, tedious, manual work. The authors have achieved the goal using a special postprocessor coded in C language. Once the CAM user had to define (on the CAD model) the theoretical boundaries of the tempered areas, the insert blocks, or the deposition material areas, the CNC program was changed automatically.

According to Zahid et al. [26], the effectiveness of NC program preparation is largely dependent on the experience of the user who manually prepares the machining plan. This author developed a special tool for recording, analysing, and improving the code during programming. As a result, both the planning time for machining and its complexity were reduced. Similar studies were presented by Deja and Siemiatkowski [27].

In turn, Tan and Ismail [28] described the methodology for recognizing the features of the CAD model, based on which appropriate operations in the CAM program are selected. Similar considerations were described in papers [29] to [31], presenting different approaches to the data exchange between the CAD and CAM programs, as well as to the recognition of the features of the objects processed, using the universal STEP files format.

In all the studies cited above, the CNC machine programming process had a low level of automation. The methods presented wereusually testedon

simple examples, which makes it difficult to assess their usefulness in practice in industry, where the manufactured parts very often have complicated shapes, and the machining process must not only include shaping, but also surface treatment.

The automation of CNC machine programming is discussed in the study by Xu et al. [32]. They presented a method forautomatically generating machining tool paths, based on the data in the integrated CAD/CAPP/CAM system. Recording the technological knowledge in the CAPP system and its further implementation in the CAM system was undertaken by Wang et al. [33]. In their study, Li et al. [34] developed a method that allows the shortening of machining planning time, demonstrating the relationship between machining data and the models used in the manufacturing process. Ma et al. [35] presented a similar approach in their study. In some studies, methods based on artificial intelligence were discussed [36] and [37], although automation in these cases concerned rather the tasks relating to the process of machining planning, and not merely program generation.

Kumar [38] presented an original system in which the automation of CNC code generation eliminated the need for specialist human knowledge and minimized the time required tocreate the program. Appropriate recording of technological knowledge wasimportant here, not only because of the quality of the tooling produced but also the quality of the CNC machine programming process in the CAM program. Li [39] provided an overview of the methods used in the recording of the technological knowledge used to prepare the machining process. Although he emphasized the importance of knowledge and the need to write it into the work, he did not specify a universal solution. It can be concluded that the selection of a tool for recording technological knowledge should be adapted to the case in question. More examples on this subject can also be found in [19] and [40] to [44].

In the literature of the subject, no reports confirm the effectiveness of the implementation of automation of CAM programming process in the case of manufacturing a group of products. Therefore, it can be assumed that systems dealing with such cases are not implemented at all or are prepared on an ad hoc basis. The ACPUT methodology fills this gap.

2 PROGRAMMING CAM WITH THE USE OF ACPUT

The basis of ACPUT [12] is the development of a special machining template that represents all the technological operations possible for a given group of products. Data and information needed to prepare such a template are stored in the special knowledge base. Knowledge acquired mainly from specialists in a given field is accumulated and written formally, so as to be understood by the computer program. To ensure the correct operation of the machining template, and thus the automation of the preparation process in the CAM environment, 3D models for the tooling must be properly described in the CAD program (i.e., categorization of features and their assignationto the model). Based on this description, the template later automatically selects the appropriate features for the given part.

ACPUT is presented in the form of a procedure and includes the following steps (Fig. 2):

1. Analysis of 3D CAD models of a given group of tooling parts.
2. Preparation of the technological knowledge base.
3. Defining the geometry necessary to build the machining template and publishing it.
4. Preparation of machining template.
5. Preparation of machining program for each part of the given group of tooling parts (with simulation in CAM program).
6. Preparation of NC program.

Step 1 is an analysis of all the CAD models of tooling (i.e., variants) included in a given group, which means checking the technological design of the individual parts and determining the types of machining operations required. The geometric similarities of the parts should be identified, and any variants determined. Once the objects have been analysed, the next step is a description of the technological process in the form of a knowledge base.

In Step 2, the knowledge base is built by breaking the technological knowledge down into basic units (i.e., detailed data), divided into two categories. The metadata of databaseis presented in Table 1.

Step 3 introduces modifications into the structure of the CAD models, adding a special description for those geometric elements associated with specific machining operations. It can be considered that such a description is a kind of record of metadata in the CAD model, after which geometric elements can be identified and specific actions performed in them in the CAM program (e.g., automatic connection of selected geometric elements of a given model (surface, line, and point) with a specific machining operation, saved onthe machining template). The advantage of this approach is that regardless of the geometric differences of the described elements in different variants of the parts, they will always be interpreted

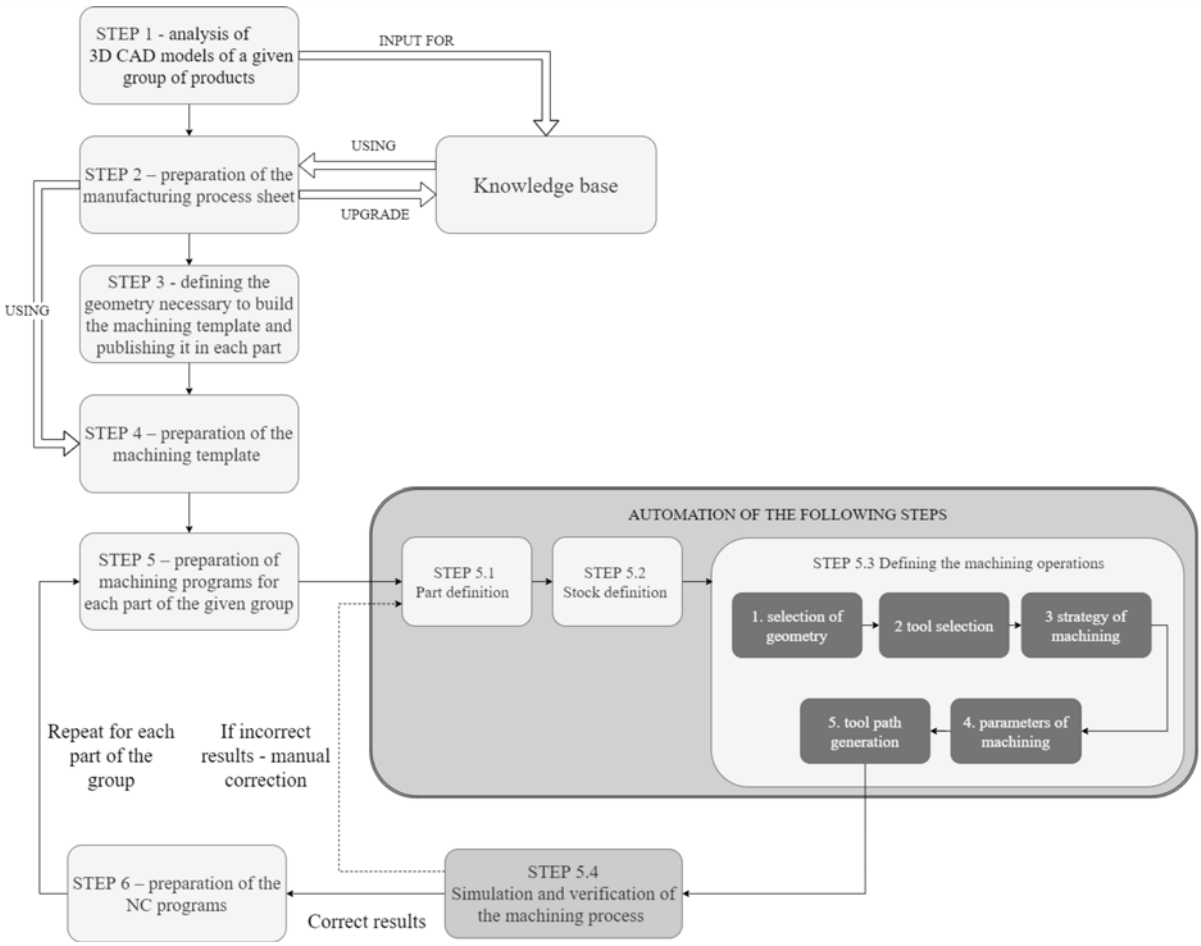

Fig. 2. *ACPUT procedure*

Table 1. *Metadata of manufacturing database*

Knowledge Database	
Basic data (general for whole process)	Machining operations (gathering for each operation separately)
I. Definition of machine tool	I. Selection of type of machining operation
a) Number of controlled axes	II. Choice of machining strategy
b) Workspace	a) The way the tool moves
c) Shifts along individual axes	b) Milling direction
d) Type of control	III. Choice of geometry
II. Definition of the workpiece	IV. Selection of machining tool
a) Workpiece geometry	a) Tool Type
III. Definition of the stock	b) Type of frame
a) Stock geometry	c) Dimensions
b) Position of the stock relative to the workpiece	V. Determination of cutting parameters
IV. Definition of workpiece position in the machine tool	a) Depth of cut
a) Position of workpiece coordinate system	b) Cutting width
b) Orientation of workpiece coordinate system (X axis, Z axis)	c) Cutting speed
V. Definition of how to mount the blank in the machine tool	d) Feed speed
a) Fastening geometry	VI. Tool path generation
VI. Definition of the safe plane	
a) Location of the safe plane	

in the same way. This is one of the conditions for the correct operation of ACPUT.

The next step (Step 4) consists of the use of the data contained in the knowledge base and, specifically, described CAD models to create a machining template in the CAM program for a given type of part. Data entered into the knowledge base, including all the basic data such as machine and workpiece data, as well as describing all possible operations to be performed, along with a definition of the machining parameters, tools, etc., are then added to the CAM template. The CAM template automates the generation of a machining program (Step 5 and Step 6) and only requires the selection of the machined part. The appropriate algorithm in CAM then adapts the machining process to it.

The automatically generated process should be simulated, assessing the compliance of the results with the assumptions for the given process. In case of any discrepancies, the knowledge record in the database should be improved. The end of the procedure is the preparation of programs specifically for the selected CNC machine.

Executing the ACPUT procedure requires different skills in manufacturing knowledge and CAD/CAM systems operation. It is therefore assumed that Step 1 and 2 are realized by an experienced technical. Step 3 can be carried out by even a novice CAM programmer; however, Step4 requires skills at the expert CAM programmer level. The last two steps can be also realized by novice CAM programmers.

3 ACPUT EFFECTIVENESS TEST

3.1 Research Methodology

Preliminary tests of ACPUT [8] showed that proceeding according to the ACPUT procedure leads to achieving an effective machining program, meaning that it is compliant with the requirements, according to the manufacturing sheet (ACPUT methodology does not concern optimizing manufacturing program).

However, the question arises whether ACPUT is equally efficient if used in everyday industrial practice. To answer this question, a comparative study of the programming efficiency of machining selected group of production tools by operators with various experience (using any tools) was conducted.

For comparison of ACPUT efficiency to the traditional way of programming a test was performed. The test was carried out with 10 CAM programmers, five of whom were experts with several years of experience and five were beginners with several months of experience. The following programming outcomes were compared in the analysis:

1. the time needed to prepare the machining programs for individual tooling part T_i [min],
2. cumulative machining time for preparing all tooling groups T_c [min],
3. sum of the cost of programming and the cost of machiningof eachtoolC_m [EUR].

Additionally, the tests were madeas to whether the parts machined in accordance with the prepared programs meet the quality requirements (geometric accuracy and surface roughness).

The following activities were considered by measuring the programming time [T_i]:

- for the first part – becoming acquainted with the whole family of products; detailed familiarization with the first part of the family; becoming acquainted with the manufacturing processsheet for the first part of the family, direct time to prepare the program for the first part in the CAM program (experts and beginners)/preparation time for the machining template (ACPUT procedure),
- for each subsequent part of the family - becoming acquainted with the n^{th} part of the family, getting to know the manufacturing process sheet for the n^{th} part of the family; direct program preparation time for the n^{th} part of the family in the CAM program (experts and beginner)/starting the machining template for the n^{th} part (ACPUT procedure).

Tooling for plastic pipes assembly, consisting of 50 parts (Fig. 3 – presents only part of them)and manufactured by milling on a CNC machine, was selected for testing. Acting in accordance with the assumptions of ETO (the tooling model was provided by the customer), it was assumed that when preparing programs, it was not possible to interfere with the geometry of the 3D models of the tools, and the files were saved in the universal STEP file format.

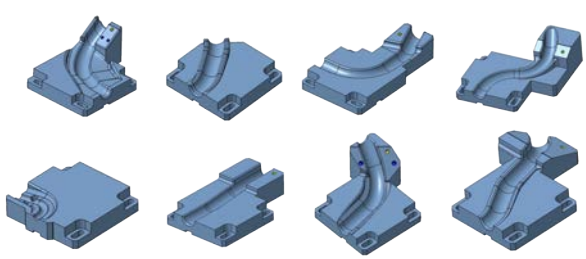

Fig. 3. *Part of the group of special tooling - assembly equipment for plastic pipes*

In accordance with the ACPUT procedure, the different geometric elements of each tool in the group

were first recognized (e.g., Fig. 4), and then described by machining operations, for which the detailed course of the machining process was recorded in the knowledge base. Based on that, the manufacturing process sheets were prepared, consisting of detailed data about machining for each part. All those initial steps (Steps 1 and 2) were made by a specialist (technician).

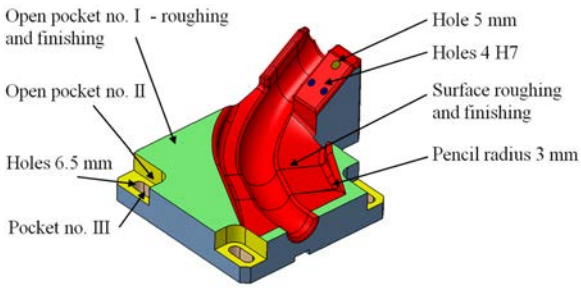

Fig. 4. *Recognized geometric elements of single tool*

The next step consisted in modification of the 3D models for each part, and the addition of a special description of those geometric elements associated with specific machining operations. These are so-called publications in CATIA V5. Publications are a description enabling the program to refer to the objects they concern. They can be considered a kind of metadata (or tags), after which geometric elements can be identified and other actions performed on them. In the case described, the publications made it possible, for example, to make a later automatic connection of selected geometric elements of a given model (surface, line, and point) with a specific machining operation, saved in the machining template. The advantage of this approach is that, regardless of the geometric differences of the published elements in different variants of the parts, they will always be interpreted in the same way in the program. This is necessary to ensure the correct operation of the automated method described. The list of publications is added to the structure of the given CAD model.

Having properly described the 3D models and the knowledge base for the machining process, a CAM process template was prepared in the CATIA V5 program. Data stored in the knowledge base was rewritten to the template, including basic machine and workpiece data, and those describing all the possible operations to be carried out along with a definition of

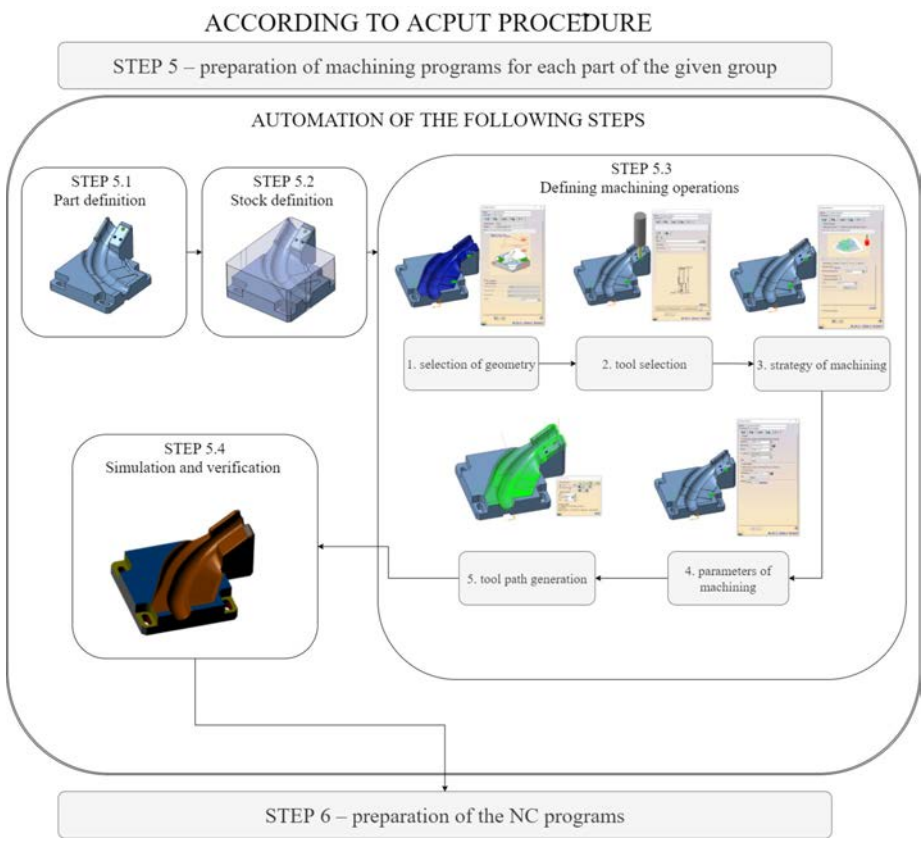

Fig. 5. *Process of programming CNC machine with automatic solution using ACPUT procedure*

the machining parameters, tools, etc. The use of the template makes it possible to automate the generation of the machining program, requiring only an indication of the workpiece variant. The appropriate algorithm in the CAM program then adapts the machining process to it. All the stages in the development of the machining program usingthe automatic method areshown in Fig. 5.

3.2 Results and Discussion

Machining programs were developed for each of the 50 parts according to:

a. the ACPUT procedure
b. the standard procedure:
   - by beginner CAM programmers,
   - by expert CAM programmers.

The manufacturing process sheets, developed by a technician in Step 2 of ACPUT, were also made available to the programmers (beginners and experts) so that the data forthe machining process were the same in all cases. In order to verify the surface quality and the accuracy of execution, one variant of the part was created according to the automatic program (ACPUT method) along with programs developed traditionally by an expert and a novice programmer. The machining quality obtained in all three cases was similar (the differences did not exceed the demands and tolerances assumed in the technological card). This is because in each case, it was based on a common data source: a knowledge base describing how a given part should be made. The differences between the programs (ACPUT procedure/expert programmers/ beginner programmers) mainly concerned the use of various functions of the CAM program to perform specific operations and the settings of the individual treatments, which in the analysed case did not affect the accuracy of the part.

3.2.1 Program Preparation Time

The preparation times of the machining programs for all three cases are presented in Table 2. The automatic programming according to ACPUT requires developing the template (Step 4 in Fig. 2); therefore, the preparation time for the first part was much longer in this case than the preparation times for the subsequent parts. A difference can also be seen in the case of the programmers (both expert and beginner), programming in the traditional manner, but it not as striking as in the ACPUT case. The differences between the programming time of an expert and beginner programmers are related to their different proficiency in using the CAM program.

The total time of the beginner programmers amounts to 2018 min (226 % of the ACPUT time), while the experts had a working time of 1175 min (132 % of ACPUT). The results presented in Table 2 are also shown in Fig. 6. This shows that the ACPUT procedure is already justified when the group of parts is greater than four.

Table 2. *Comparison of preparation time for machining programs*

Part No.	CAM preparation time [min]							
	ACPUT procedure		Standard procedure – Beginners (average for 5 participants)			Standard procedure - Experts (average for 5 participants)		
	Ti	rising	Ti	rising	Range	Ti	rising	Range
1	224	224	145	145	43	79	79	17
2	12	236	58	203	7	28	107	11
3	14	250	42	245	10	29	136	6
4	11	261	42	287	21	18	154	8
5	13	274	41	328	15	32	186	7
6	11	285	35	363	8	25	211	3
7	12	297	39	402	18	28	240	13
8	10	307	44	445	9	20	260	8
9	13	320	40	485	14	27	287	11
10	10	330	37	522	19	22	309	6
…	...	...	…	…	…	…	…	
20	11	460	38	914	7	18	519	3
30	14	606	29	1286	9	16	727	11
40	19	752	41	1673	15	26	955	19
50	10	891	30	2018	14	18	1175	7

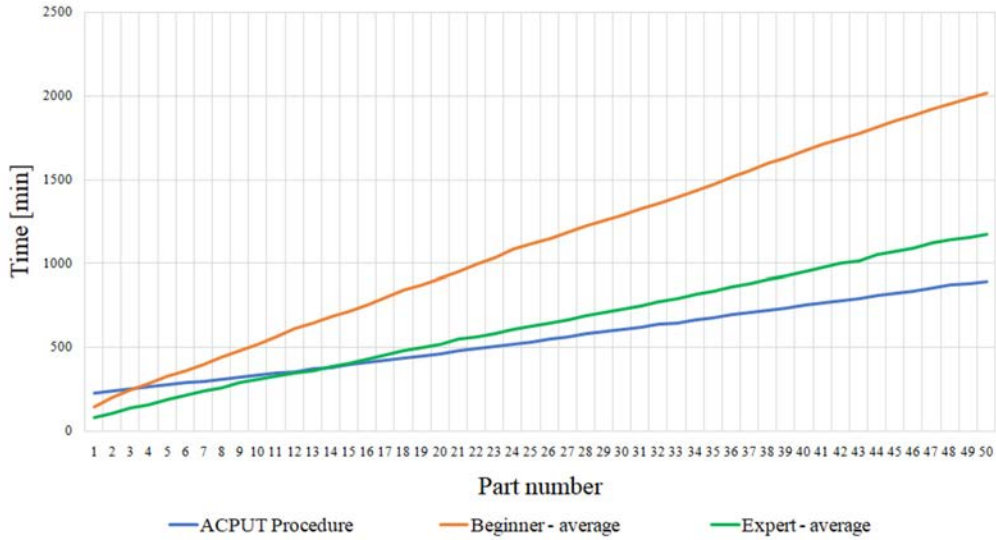

Fig. 6. *CAM preparation time -rising*

A summary of the machining times from the simulation for each part separately and rising are presented in Table 3 and Fig. 7. Because the parameters and the method of processing were specified in the technological knowledge base, and each of the programmers operated using the same data, the differences in the machining times for individual parts were insignificant. The difference between the ACPUT procedure and the expert programmers was 3.3 %, while between the ACPUT procedure and the beginner programmers amounted to 5.3 %. This mainly resulted from the selection of other speeds and the tool's path of movement during its approach and departure from the workpiece. It should be emphasized here that these parameters were not specified in the technological knowledge base.

The total time for the preparation of the machining programs and the machining for all 50 parts was 4863 min in the case of the programming using ACPUT procedure, 6200 min (representing 127.5 %

Table 3. *Part machining time on CNC machine based on simulation in CAM program*

Part No.	Machining time [min]					
	ACPUT procedure		Standard procedure – Beginner (average for 5 participants)		Standard procedure – Expert (average for 5 participants)	
	for each	Tc	for each	Tc	for each	Tc
1	141	141	147	147	126	126
2	87	228	86	233	94	220
3	119	347	127	360	123	343
4	43	390	47	407	44	387
5	77	467	80	486	78	465
6	42	509	46	533	44	509
7	86	595	90	622	85	594
8	43	638	47	669	45	639
9	99	737	106	775	98	737
10	45	782	49	824	44	780
…	…	…	…	…	…	…
20	82	1800	85	1885	83	1826
30	51	2610	55	2740	51	2673
40	59	3292	58	3471	66	3408
50	49	3972	52	4182	49	4102

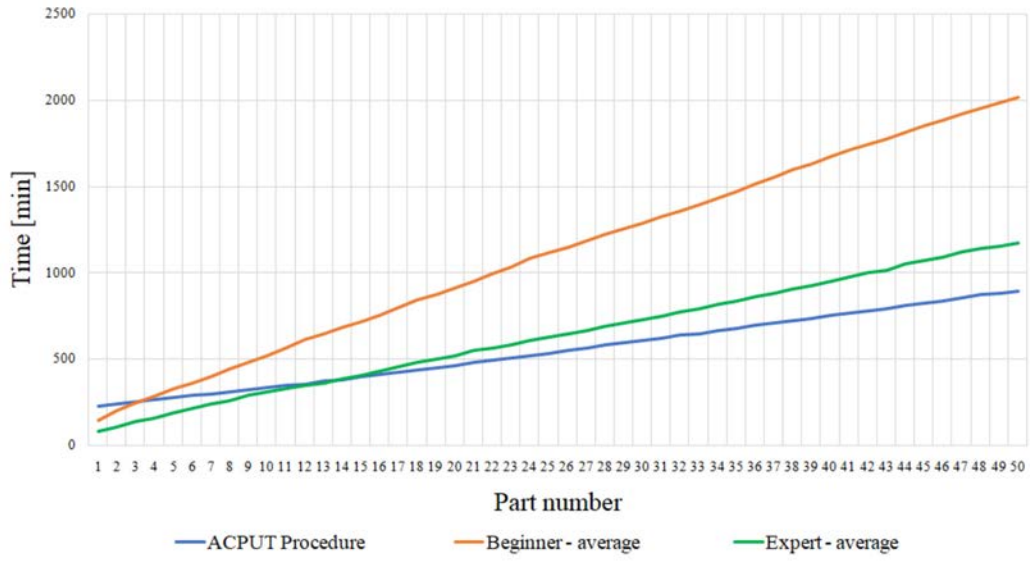

Fig. 7. *Machining time - rising*

of the working time of the ACPUT procedure) for the beginner technicians and 5277 min (108.5 % of the working time of the automatic solution) for the expert technicians. The above data are presented in Table 4.

3.2.2 Manufacturing Costs

The average cost for the machine programming for a single part (*MPc*) for a given number of parts in the group (*Gs*), where (*Pr*) is a pay rate for the CAM programmer/technician is:

$$MPc = (\Sigma T_i / 60 \times Pr) / Gs. \quad (1)$$

Supposing the pay rate for the beginner programmer (*Prb*) was € 60/h and the expert's pay rate (*Pre*) was € 80/h, it emerged that the average cost for the machine programming for a single part (*MPc*) from a given group of parts (*Gs*), was respectively, € 40 for the beginner and € 31 for the expert.

In the case of the ACPUT procedure, to build a machining template, expert knowledge is necessary, while to program the machining of subsequent parts,

Table 4. *Total manufacturing time*

Part No.	CAM preparation and machining time [min]					
	ACPUT procedure		Standard procedure – Beginner (average for 5 participants)		Standard procedure – Expert (average for 5 participants)	
	for each	Tc	for each	Tc	for each	Tc
1	365	365	292	292	205	205
2	99	464	144	436	123	328
3	133	597	169	605	151	479
4	54	651	89	694	62	541
5	90	741	121	815	109	651
6	53	794	81	896	69	720
7	98	892	128	1024	113	833
8	53	945	90	1114	66	899
9	112	1057	146	1260	125	1024
10	55	1112	86	1347	65	1089
…	…	…	…	…	…	…
20	93	2260	122	2798	101	2344
30	65	3216	83	4026	67	3400
40	78	4044	99	5145	92	4363
50	59	4863	82	6200	67	5277

the knowledge of a beginner programmer is sufficient. Thus:

$$MPc = [T_1 / 60 \times Pre + (\Sigma (T_i - T_1)) / 60 \times Prb] / Gs. \quad (2)$$

In the case above, the first part of the procedure assumed a man-hour cost of € 80/h while for the next it totalled € 60/h. It follows that for the ACPUT procedure, the average programming cost for machining a single part was € 19.

Assuming a pay rate of € 35/h, the average cost of the machining for a single part in ACPUT procedure was € 46, by beginner programmer (average) € 49 and for the expert programmer € 48.

The individual cost of tool manufacture C_m [EUR], consisting of the cost of preparing the machining programs (*MPc*) and the cost of machining itself, was the lowest for the ACPUT procedure - an average of €66 per part (€ 3300 for all 50 parts). In the case of the beginner technicians, the C_m was € 89 (135.8% of ACPUT C_m, € 4450 for all 50 parts) and € 79 (120.6% 35.8% of ACPUT C_m, € 3950 for all 50 parts) for the experts. A summary of C_m is presented in Fig. 8.

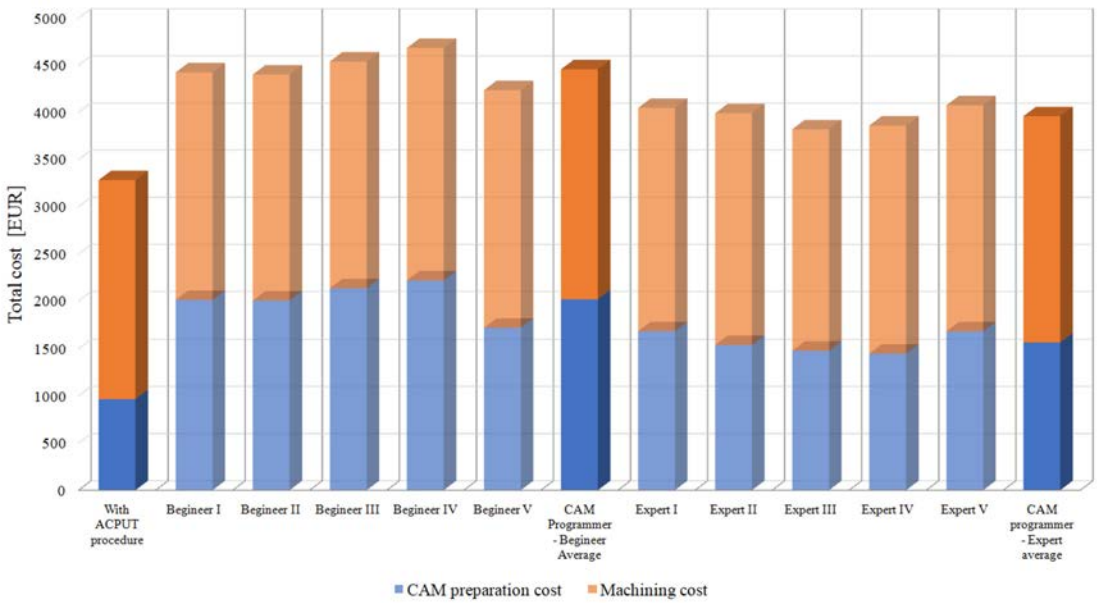

Fig. 8. *Special production tooling manufacture costs*

4 SUMMARY AND CONCLUSIONS

In the present paper, a CAM programming procedure, called ACPUT, was presented. ACPUT is dedicated to the manufacture of special technological tooling, which consists of technologically similar parts. The procedure includes the development of special machining templates in the CAM program, supported by the technological knowledge gathered in a specially prepared database.

The theoretical functionality of ACPUT was studied in earlier work, but it was necessary to validate its practical effectiveness, taking time and cost of manufacturing the group of tooling into account. Therefore, the main aim of this research was to check when the automatic CAM programming method would be better than the traditional CAM programming approach.

Testing under industrial conditions showed that the ACPUT procedure makes it possible to reduce the time needed to develop a machining program. This has a positive effect on the total cost of tooling production.

The effectiveness of ACPUT was tested based on the analysis of the time needed to prepare the CNC program and the machining operation time itself (based on the simulation in CAM). The preparation time of the program is a direct (next to the quality conditions) indicator of the effectiveness of ACPUT. Analysing Table 2 and Fig. 6, it can be seen that the time benefits of using an automatic solution are significant, especially when compared to a less experienced technician.

It should be emphasized that the effectiveness of the ACPUT procedure depends on the experience of those who prepare the templates. For the tests

carried out, ten CAM programmers were invited to participate: five with several years' experience and five with limited experience (working in this position for only a few months). The first group was considered an expert and the second asa beginner. The aim of the study was not to indicate the predictable differences between them but to evaluate ACPUT which constituted a reference. Separating the technicians into more experienced and less experienced groups had one more purpose: to assess whether, after preparing the machining templates according to ACPUT, someone with less experience would be able to use the automatic solution successfully. The study revealed that it was possible: the results obtained using the automatic solution was even better than the work produced by expert.

The ACPUT procedure is, in its assumption, universal; it does not require the use of any specific CAM system or knowledge base construction program, because it does not indicate the use of specific tools to prepare the machining templates. In this study, the CATIA V5 program was used to build the machining template, but it should be considered an example of the possible software that can be used. Machining templates can also be built in other systems of this type. However, it is worth emphasizing that it is best to use integrated CAD/CAM software for these purposes (thereby facilitating data exchange).

However, attention should be paid to certain limitations related to the practical application of the proposed method. Firstly, the automation of CNC machine programming according to the ACPUT method assumes the preparation of machining templates for a given family of parts. Their development is, of course, possible in advanced CAD/CAM programs. However, it requires skills in the field of VB programming in order to develop algorithms that allow for automatic recognition of specific geometric features of the machined part and appropriate technological operations in CAM to be assigned to them. In addition, the implementation of programming automation according to ACPUT requires the development and description of standards for the technology used within production companies. For the correct, automatic generation of machining programs in the future, it is advisable to create a knowledge base dependent on the experience of the employees and the analysis of archival works.

The achieved results are satisfying, and the conclusions seem useful for practical use. The automation of CAM programming is laborious, complicated and, therefore, difficult to implement in practice. In many cases, the automation of CAM programming does not achieve the assumed results (e.g., the program preparation time gain is not significant) because it is difficult to evaluate the labour intensity for the whole group of manufacturing tools. Research of the ACPUT method complements the knowledge in this field.

In terms of further research, it would be worth checkingthe possibility of generating programs for specific types of CNC machine controls. However, in the meantime, more immediate research will focus on the development of a method for the rapid assessment of the technological similarity of the parts for which the preparation of a machining template is planned. It is expected that if the difference between the parts is too great, it will not be profitable to prepare the template and apply the ACPUT procedure. In such a case, it would be preferable to use the traditional programming procedure.

5 ACKNOWLEDGEMENTS

We thank the all technology team from Mk-Tech Company for providing a special tooling project for our research, for sharing knowledge about holding milling processes and for helping us during the tests. We also thank Radoslaw Paszkiewicz from Poznan University of Technology for valuable tips and tricks used in CAM programming in the Catia system.

The presented results were financed from statutory scientific research conducted by the Faculty of Mechanical Engineering, Poznan University of Technology, Poland, supported by the Polish Ministry of Science and Higher Education from the financial means in 2021, no.0613/SBAD/4677.

6 REFERENCES

[1] Lu, Y. (2017). Industry 4.0: A survey on technologies, applications and open research issues. *Journal of Industrial Information Integration*, vol. 6, p. 1-10, **DOI:10.1016/j.jii.2017.04.005**.

[2] Alcacer, V., Cruz-Machado, V. (2019). Scanning the Industry 4.0: A Literature Review on Technologies for Manufacturing Systems. *Engineering Science and Technology, an International Journal*, vol. 22, no. 3, p. 899-919, **DOI:10.1016/j.jestch.2019.01.006**.

[3] Brettel, M., Friederichsen, N., Keller, M., Rosenberg, M.(2014). How virtualization, decentralization and network building change the manufacturing landscape: An Industry 4.0 perspective. *International Journal of Mechanical, Aerospace, Industrial, Mechatronic and Manufacturing Engineering*, vol. 8, no. 1, **DOI:10.5281/zenodo.1336426**.

[4] Hamrol, A., Gawlik, J., Sładek, J. (2019). Mechanical engineering in Industry 4.0. *Management and Production*

Engineering Review, vol. 10, no. 3, p. 14-28, **DOI:10.24425/mper.2019.129595**.

[5] Gök, A., Gök, K., Bilgin, M.B., Alkan, M.A. (2017). Effects of cuttingparameters and tool-pathstrategies on toolacceleration in ball-end milling. Materials and Technology, vol. 51, no. 6, p. 957-965, **DOI:10.17222/mit.2017.039**.

[6] Gok, A. (2015). A newapproachtominimization of thesurfaceroughness and cuttingforce via fuzzy TOPSIS, multi-objectivegrey design and RSA. *Measurement*, vol. 70, p. 100-109, **DOI:10.1016/j.measurement.2015.03.037**.

[7] Liu, Y., Xu, X. (2017). Industry 4.0 and cloud manufacturing: A comparative analysis. *Journal of Manufacturing Science and Engineering*, vol. 139, no. 3, art ID: 034701, **DOI:10.1115/1.4034667**.

[8] Fogliatto, F.S., Da Silveira, G.J.C., Borenstein, D. (2012). The mass customization decade: An updated review of the literature. *International Journal of Production Economics*, vol. 138, no. 1, p. 14-25, **DOI:10.1016/j.ijpe.2012.03.002**.

[9] Zawadzki, P., Żywicki, K. (2016). Smart product design and production control for effective mass customization in the Industry 4.0 concept. *Management and Production Engineering Review*, vol. 7, no. 3, p. 105-112, **DOI:10.1515/mper-2016-0030**.

[10] Zawadzki, P. (2018). Methodology of KBE system development for automated design of multivariant products. In: Hamrol, A., Ciszak, O., Legutko, S., Jurczyk, M. (eds). *Advances in Manufacturing, Lecture Notes in Mechanical Engineering*, p. 239-248, Springer, Cham, **DOI:10.1007/978-3-319-68619-6_23**.

[11] Kowalski, M., Zawadzki, P. (2019). Tooling CAD models preparation process for automated technology design system. In: Hamrol, A., Kujawińska, A., Barraza, M. (eds.). *Advances in Manufacturing II. MANUFACTURING. Lecture Notes in Mechanical Engineering*, Springer, Cham, **DOI:10.1007/978-3-030-18789-7_4**.

[12] Kowalski, M., Zawadzki, P. (2019). Decomposition of knowledge for automatic programming of CNC machines. *Management and Production Engineering Review*, vol. 10, no. 1, **DOI:10.24425/mper.2019.128248**.

[13] Strandhagen, J.W., Vallandingham, L.R., Alfnes, E., Strandhagen, J.O. (2018). Operationalizing lean principles for lead time reduction in engineer-to-order (ETO) operations: A case study. *IFAC-PapersOnLine*, vol. 51, no. 11, p. 128-133, **DOI:10.1016/j.ifacol.2018.08.246**.

[14] Kowalski, M. (2020). Method of automatic CAM programming using machining templates. *Mechanik*, vol. 93, no. 1, p. 48-52, **DOI:10.17814/mechanik.2020.1.4**.

[15] Verma, A.K., Rajotia, S. (2010). A review of machining feature recognition methodologies. *International Journal of Computer Integrated Manufacturing*, vol. 23, no. 4, p. 353-368, **DOI:10.1080/09511921003642121**.

[16] Chevalier, P.W. (1984). Group technology as a CAD/CAM integrator in batch manufacturing. *International Journal of Operations & Production Management*, vol. 4, no. 3, p. 3-12, **DOI:10.1108/eb054715**.

[17] Babic, B., Nesic, N., Miljkovic, Z. (2008). A review of automated feature recognition with rule-based pattern recognition. *Computers in Industry*, vol. 59, no. 4, p. 321-337, **DOI:10.1016/j.compind.2007.09.001**.

[18] Zhang, Z., Jaiswal, P., Rai, R. (2018). Featurenet: Machining feature recognition based on 3D convolution neural network. *Computer-Aided Design*, vol. 101, p. 12-22, **DOI:10.1016/j.cad.2018.03.006**.

[19] Sateesh, P., Mahesh, P.V. (2017). A methodology for feature extraction and recognition for CAD/CAM integration using step file. *International Journal of Research and Innovation*, vol. 4, no. 1, p. 711-725.

[20] Skvortsov, V., Proletarsky, A., Arzybaev, A. (2019). Feature recognition module of the CAPP system. *IEEE Conference of Russian Young Researchers in Electrical and Electronic Engineering*, p. 1769-1772, **DOI:10.1109/EIConRus.2019.8656655**.

[21] Zhou, G., Yang, X., Zhang, C., Li, Z., Xiao, Z. (2019). Deep learning enabled cutting tool selection for special-shaped machining features of complex products. *Advances in Engineering Software*, vol. 133, p. 1-11, **DOI:10.1016/j.advengsoft.2019.04.007**.

[22] Andriankaja, H., Le Duigou, J., Eynard, B. (2015). Sustainable machining approach by integrating the environmental assessment within the CAD/CAM/CNC Chain. In Chakrabarti, A. (ed). *ICoRD'15-Research into Design Across Boundaries Volume 2. Smart Innovation, Systems and Technologies*, p. 227-236. Springer, New Delhi, **DOI:10.1007/978-81-322-2229-3_20**.

[23] Zhou, H., Wu, J. (2016). Research on CAD/CAM Integration Methods Based on the STL Model. In *Proceedings of the 5th International Conference on Electrical Engineering and Automatic Control, Lecture Notes in Electrical Engineering*, vol. 367. p. 1201-1207, Springer, Berlin, Heidelberg, **DOI:10.1007/978-3-662-48768-6_134**.

[24] De Lacalle, L.L., Lamikiz, A., Muñoa, J., Salgado, M.A., Sánchez, J.A. (2006). Improving the high-speed finishing of forming tools for advanced high-strength steels (AHSS). *The International Journal of Advanced Manufacturing Technology*, vol. 29, p. 49-63, **DOI:10.1007/s00170-004-2482-z**.

[25] De Lacalle, L.L., Lamikiz, A., Salgado, M.A., Herranz, S., Rivero, A. (2002). Process planning for reliable high-speed machining of moulds. *International Journal of Production Research*, vol. 40, no. 12, p. 2789-2809, **DOI:10.1080/00207540210140068**.

[26] Zahid, M.N.O., Case, K., Watts, D. (2017). Rapid process planning in CNC machining for rapid manufacturing applications. *International Journal of Mechanical Engineering and Robotics Research*, vol. 6, no. 2, p. 118-121, **DOI:10.18178/ijmerr.6.2.118-121**.

[27] Deja, M., Siemiatkowski, M.S. (2013). Feature-based generation of machining process plans for optimised parts manufacture. *Journal of Intelligent Manufacturing*, vol. 24, p. 831-846, **DOI:10.1007/s10845-012-0633-x**.

[28] Tan, C.F., Kher, V.K., Ismail, N. (2013). Design of a feature recognition system for CAD/CAM integration. *World Applied Sciences Journal*, vol. 21, no. 8, p. 1162-1166, **DOI:10.5829/idosi.wasj.2013.21.8.2126**.

[29] Sivakumar, S., Dhanalakshmi, V. (2013). An approach towards the integration of CAD/CAM/CAI through STEP file using feature extraction for cylindrical parts. *International Journal*

of Computer Integrated Manufacturing, vol. 26, no. 6, p. 561-570, **DOI:10.1080/0951192X.2012.749527**.

[30] Miao, H.K., Sridharan, N., Shah, J.J. (2002). CAD-CAM integration using machining features. *International Journal of Computer Integrated Manufacturing*, vol. 15, no. 4, p. 296-318, **DOI:10.1080/09511920110077502**.

[31] Sivakumar, S., Dhanalakshmi, V. (2013). A feature-based system for CAD/CAM integrationthrough STEP file for cylindrical parts. *Indian Journal of Engineering & Material Science*s, vol. 20, p. 21-26, **DOI:10.1080/0951192X.2012.749527**.

[32] Xu, T., Chen, Z., Li, J., Yan, X. (2015). Automatic tool path generation from structuralized machining process integrated with CAD/CAPP/CAM system. *The International Journal of Advanced Manufacturing Technology*, vol. 80, p. 1097-1111, **DOI:10.1007/s00170-015-7067-5**.

[33] Wang, J., Zhang, H.L., Su, Z.Y. (2012). Manufacturing knowledge modeling based on artificial neural network for intelligent CAPP. *Applied Mechanics and Material*s, vol. 127, p. 310-315, **DOI:10.4028/www.scientific.net/AMM.127.310**.

[34] Li, J., Chen, Z.,Yan, X. (2014). Automatic generation of in-process models based on feature working step and feature cutter volume. *The International Journal of Advanced Manufacturing Technology*, vol. 71, no. 1-4, p. 395-409, **DOI:10.1007/s00170-013-5507-7**.

[35] Ma, H., Zhou, X., Liu, W., Li, J., Niu, Q., Kong, C. (2018). A feature-based approach towards integration and automation of CAD/CAPP/CAM for EDM electrodes. *The International Journal of Advanced Manufacturing Technology*, vol. 98,p. 2943-2965, **DOI:10.1007/s00170-018-2447-2**.

[36] Kumar, S.P.L. (2017). State of the art-intense review on artificial intelligence systems application in process planning and manufacturing. *Engineering Applications of Artificial Intelligence*, vol. 65, p. 294-329, **DOI:10.1016/j.engappai.2017.08.005**.

[37] Li, S., Li, J., Ma, Y., Liu, G. (2018). Application of Intelligent process decision in CAPP. *International Arab Journal of e-Technology*, vol. 5, no. 2, p. 71-77.

[38] Leo Kumar, S.P. (2018). Automation of tool path generation in multi-process micromachine tool for micromachining of prismatic and rotational parts. *International Journal of Computer Integrated Manufacturing*, vol. 31, no. 1, p. 49-70, **DOI:10.1080/0951192X.2017.1356471**.

[39] Li, X., Zhang, S., Huang, R., Huang, B., Xu, C., Zhang, Y. (2018). A survey of knowledge representation methods and applications in machining process planning. *The International Journal of Advanced Manufacturing Technology*, vol. 98, p. 3041-3059, **DOI:10.1007/s00170-018-2433-8**.

[40] Ma, H., Zhou, X., Liu, W., Li, J., Niu, Q., Kong, C. (2018). A feature-based approach towards integration and automation of CAD/CAPP/CAM for EDM electrodes. *The International Journal of Advanced Manufacturing Technology*, vol. 98, p. 2943-2965, **DOI:10.1007/s00170-018-2447-2**.

[41] Venu, B., Komma, V.R., Srivastava, D. (2018). STEP-based feature recognition system for B-spline surface features. *International Journal of Automation and Computing*, vol. 15, p. 500-512, **DOI:10.1007/s11633-018-1116-0**.

[42] Lavrentyeva, M.V., Chimitov, P.Y. (2017). Implementation of recognition algorithm with NXOpen API in siemens NX. *International Conference on Industrial Engineering, Applications and Manufacturing*, p. 1-4, **DOI:10.1109/ICIEAM.2017.8076193**.

[43] Klancnik, S., Brezocnik, M., Balic, J. (2016). Intelligent CAD/CAM system for programming of CNC machine tools. *International Journal of Simulation Modelling*, vol. 15, no. 1, p. 109-120, **DOI:10.2507/IJSIMM15(1)9.330**.

[44] Chung, C., Ma, T. (2017). Implementation of CAM programming with machinability database. *IEEE/SICE International Symposium on System Integration*, p. 236-240, **DOI:10.1109/SII.2017.8279218**.

Strojniški vestnik - Journal of Mechanical Engineering 67(2021)10, 489-500
DOI:10.5545/sv-jme.2021.7284
Original Scientific Paper
Received for review: 2021-06-07
Received revised form: 2021-08-17
Accepted for publication: 2021-09-09

Fault Diagnosis of Rotation Vector Reducer for Industrial Robot Based on a Convolutional Neural Network

Shuai Yang[1,*] – Xing Luo[2] – Chuan Li[2]

[1] Chongqing Technology and Business University, National Research Base of Intelligent Manufacturing Service, China
[2] Chongqing Technology and Business University, School of Management Science and Engineering, China

As a key component of a mechanical drive system, the failure of the reducer will usually cause huge economic losses and even lead to serious casualties in extreme cases. To solve this problem, a two-dimensional convolutional neural network (2D-CNN) is proposed for the fault diagnosis of the rotation vector (RV) reducer installed on the industrial robot (IR). The proposed method can automatically extract the features from the data and reduce the connections between neurons and the parameters that need to be trained with its local receptive field, weight sharing, and subsampling features. Due to the aforementioned characteristics, the efficiency of network training is significantly improved, and verified by the experimental simulations. Comparative experiments with other mainstream methods are carried out to further validate the fault classification accuracy of the proposed method. The results indicate that the proposed method out-performs all the selected methods.
Keywords: fault diagnosis, convolutional neural network, RV reducer

Highlights
- *An improved method based on deep-learning algorithms is proposed in this paper.*
- *2D-FFT and 2D-CNN are combined for the fault diagnosis.*
- *The efficiency of network training is significantly improved.*
- *Comparative experiments with other mainstream methods are carried out, and the fault classification accuracy of the proposed method is validated.*

0 INTRODUCTION

An industrial robot (IR) is defined as a device with multi-joint manipulator or multi-degree of freedom, which has been widely used in various industries, such as electronics, manufacturing, and aerospace [1]. Due to its automaticity and controllability, IR can provide a variety of functions in industrial processing or manufacturing. In the late 1950s, the first-generation IR was designed and manufactured by General Motors for completing simple and repetitive operations. After several decades of evolution, IR has become one of the most common devices in the manufacturing sector.

With the development of manufacturing and computer science, the IR has been increasing in intelligence, flexibility, and interactivity, which can satisfy the diverse needs of various costumers [2].

For most industrial robots, there are three major components and six subsystems. Among them, the driving system (motor) is the key part that provides power to the mechanical system of an IR [3]. Due to the high rotation speed and torque of the servo motor, a motor reducer is required for the driving system, which can match the rotation speed and transmit the torque between driving motor and actuator. The accuracy of the transmission ratio for a reducer directly affects the displacement precision and reduces the service life of the IR [4].

Because of the harsh working conditions, failure of the reducer is one of the most common phenomena in a mechanical system. Wear and leakage are two major types of failure, which can cause the shut-down of a mechanical system. Therefore, fault detection and diagnosis of the reducer are required.

In recent years, the deep-learning (DL) method has become the dominant method in fault diagnosis for extraction, detection, and classification. The mainstream DL methods include deep neural network (DNN), deep belief network (DBN), recursive neural network (RNN) and convolutional neural network (CNN).

Among them, CNN was initially applied to the recognition and classification of images. However, it also shows promising results in fault diagnosis, which can automatically extract features from the original data without manual selection. By training and adjusting the values of the convolution kernel, CNN can achieve the classification and recognition of fault based on the raw data [5] and [6].

Pan et al. [7] propose an improved bearing fault diagnosis method based on CNN and a long-short-term memory (LSTM) recurrent neural network whose input is the raw sampling signal without any pre-processing or traditional feature extraction. Janssens et al. [8] pre-processed the vibration data of bearing shell by fast Fourier transform (FFT) and input it

*Corr. Author's Address: Chongqing Technology and Business University, No .19 Xuefu Avenue, Chongqing, China, jerryyang@ctbu.edu.cn

into CNN for fault detection. Jing et al. [9] focused on the research and development of CNN, which can directly learn features from the frequency data of vibration signals, and test the different performance of feature learning from original data, spectrum, and time-frequency combined data. Azamfar et al. [10] proposed a fault diagnosis method based on the analysis of motor current characteristics. The data obtained from multiple current sensors are fused by a new two-dimensional convolutional neural network structure, which can be directly used for classification without manual feature extraction. DCNN was applied to solve the multi-state fault identification problem of gearboxes. By directly inputting the original signal, a higher diagnosis accuracy is obtained with a lower calculation time cost [11]. The two-dimensional mapping representation method based on cyclic spectrum coherence (CSCoh) and CNN is used to improve the fault identification performance of rolling bearings, which is a new fault diagnosis method based on DL proposed by Chen et al. [12]. A new full closed-loop method based on a deep convolution neural network is proposed to detect and classify the data of power quality disturbances [13]. Xuan and You [14] proposed a hierarchical convolutional neural network (HCNN) based on DL, which was used to detect pancreatic tumours. This method can improve the performance of the classifier and reduce the cost of the medical Internet of Things (IoMT). A framework based on DL was applied to classify the target data, which adopted deep CNN to learn the compact and effective representation of each signal from wavelet coefficients. This method is used to classify the ultrasonic signals of carbon fibre reinforced polymer (CFRP) specimens with voids and delamination [15]. Lu et al. [16] proposed a new method of rice disease recognition based on a deep convolution neural network and achieved good results. In [17], a time-varying reliability method of rotation vector (RV) reducer for industrial robots with multiple failure modes based on the Kriging model is proposed.

Based on the previous research, the application of the CNN model for fault detection and classification has achieved tremendous progress in many fields. However, for RV reducers of IR, the application of the CNN model remains rare. As is well-known, a convolutional neural network has unique advantages in processing massive data and can learn features from massive data. In this paper, a 2D-CNN based on the experimental vibration data after 2D-FFT is proposed for the fault diagnosis of an RV reducer for IR. Comparisons are conducted with other mainstream methods. The results indicate that the proposed method shows better performance in the fault diagnosis of an RV reducer.

1 METHODS

1.1 Back Propagation (BP) Algorithm

Since Rumelhart et al. [18] and [19] reinvented and described the application of the BP algorithm in neural networks in 1986, this algorithm has become a standard learning method for neural network models. Due to its high efficiency, the BP algorithm is also selected to determine the network parameters of the CNN model in this paper.

With the BP algorithm, the matrix of universal parameters can be optimized by error-oriented motion, which is used for the classified task of the CNN. The residual error between the actual and expected output is sent back to the hidden layer and eventually back to the input layer. Based on the results, the weighted coefficient will be adjusted to minimize the error till the optimal coefficient is obtained. The loss function for a single sample is written as follows:

$$J\left(W,b;x,y\right)=\frac{1}{2}h_{W,b}\left(x\right)-y^{2}, \tag{1}$$

where $h_{W,b}(x)$ is the actual output, y is the desired output, W is the weight-matrix, b is a bias vector. Assume there are m samples in each data set, the overall cost function can be defined as:

$$J\left(W,b\right)=\left[\frac{1}{m}\sum_{1}^{m}\left(\frac{1}{2}h_{W,b}\left(x^{(i)}\right)-y^{(i)2}\right)\right]+\Gamma, \tag{2}$$

where Γ is the regularization term or weight decay term, which can reduce the magnitude of the weight to prevent overfitting, m is the number of samples. Γ can be determined by:

$$\begin{cases}\Gamma=\dfrac{\lambda}{2}\displaystyle\sum_{l=1}^{n_l-1}\sum_{i=1}^{s_l}\sum_{j=1}^{s_{l+1}}\left(W_{ij}^{l}\right)^{2}\\ l=n_l-1,n_l-2,\ldots,2\end{cases}, \tag{3}$$

where λ stands for the weight decay parameter; W_{ij}^{l} is the weight matrix between the i^{th} neuron in layer l and the j^{th} neuron in layer $l+1$, n_l is the output layer. The gradient descent method updates the parameters w and b:

$$W_{ij\,new}^{l}=W_{ij\,old}^{l}-\alpha\frac{\partial}{\partial W_{ij\,old}^{l}}J\left(W,b\right), \tag{4}$$

$$b_{i\,new}^{l}=b_{i\,old}^{l}-\alpha\frac{\partial}{\partial b_{i\,old}^{l}}J\left(W,b\right), \tag{5}$$

where α represents the learning rate; b_i^l is the bias vector of the i^{th} neuron in layer l. Using the backpropagation algorithm to calculate the partial derivative, the residual calculation formula for each output unit of the output layer is listed as follows:

$$\delta_i^{n_l} = \frac{\partial}{\partial z_i^{n_l}} \frac{1}{2} y - h_{W,b}(x)^2 = -\left(y_i - a_i^{n_l}\right) \cdot f'\left(z_i^{n_l}\right), \quad (6)$$

where $a_i^{n_l}$ is the i^{th} input of output layer; $f'\left(z_i^{n_l}\right)$ is the derivative of the activation function that takes the partial derivative of $a_i^{n_l}$; $\delta_i^{n_l}$ is the residual. The residual calculation formula for each output unit of the other layer can be written as:

$$\delta_i^l = \left(\sum_{j=1}^{s_{n_l}} W_{ij}^l \delta_j^{n_l}\right) f'\left(z_i^l\right). \quad (7)$$

The calculation method of partial derivative can be presented by:

$$\frac{\partial}{\partial W_{ij}^l} J(W,b;x,y) = a_i^l \delta_i^{n_l}, \quad (8)$$

$$\frac{\partial}{\partial b_i^l} J(W,b;x,y) = \delta_i^{n_l}. \quad (9)$$

Thus, the residual calculation formula for the output layer and other layer are rewritten as:

$$\delta^{n_l} = -\left(y - a^{n_l}\right) \cdot f'\left(z^{n_l}\right), \quad (10)$$

$$\delta^l = \left(\left(W^l\right)^T \delta^{l+1}\right) \cdot f'\left(z^l\right). \quad (11)$$

Calculating the final required partial derivative value:

$$\nabla_{W^l} J(W,b) = \delta^{l+1}\left(a^l\right)^T, \quad (12)$$

$$\nabla_{b^l} J(W,b) = \delta^{l+1}. \quad (13)$$

The calculation formula for the change of parameters W and b are as follows:

$$\Delta W^l = \Delta W^l + \nabla_{W^l} J(W,b), \quad (14)$$

$$\Delta b^l = \Delta b^l + \nabla_{b^l} J(W,b). \quad (15)$$

The final parameters update formulas are as follows:

$$W^l = W^l - \alpha\left[\left(\frac{1}{m}\Delta W^l\right) + \lambda W^l\right], \quad (16)$$

$$b^l = b^l - \alpha\left[\left(\frac{1}{m}\Delta b^l\right)\right]. \quad (17)$$

1.2 Typical Structure of CNN Method

CNN is a feedforward neural network with a deep structure that includes convolution computation [20]. The initial concept of CNN was proposed by LeCun et al. [21]. However, the actual application of CNN began in 2012, due to the appearance of AlexNet [22]. This method has been widely used in various fields, such as image recognition, speech separation and video classification.

For most CNN models in fault classification, feature extraction, feature selection, and fault classification are three major parts. As shown in Fig. 1, there are five layers in the structure of CNN: input

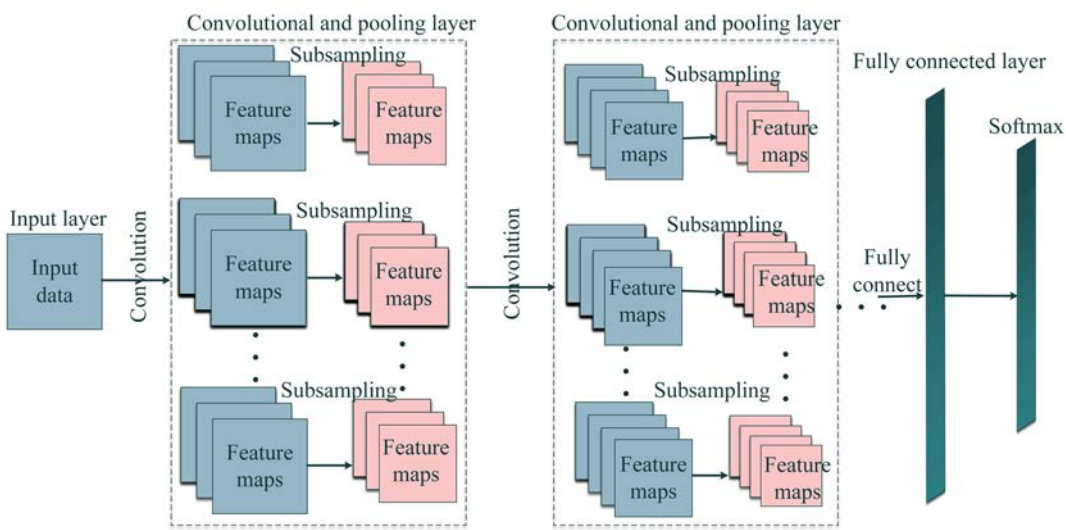

Fig. 1. *Typical structure of CNN*

layer, convolution layer, pooling layer, fully connected layer, and output layer.

(1) Convolution layer: as shown Fig. 1, there are many feature maps in the convolution layer; for each map, multiple neurons are distributed. The feature map of the former layer is connected to those neurons by the convolution kernel. As a feature matrix, the convolution kernel can extract the partial features of the input data. Due to the weight sharing of the convolution layer, the parameters in this layer can be minimized, which will improve the time of computation and avoid overfitting.

The output area of the convolution layer can be determined by:

$$Omap_{con} = \frac{Imap_{con} - kers + 2 \cdot padding}{stride} + 1. \quad (18)$$

In this equation, $Omap_{con}$ is the output area of the convolution layer, $Imap_{con}$ is the input area of convolution layer, *kers* is the convolution kernel, *stride* stands for the sliding length of convolution kernel, *padding* represents the padding size.

The specific convolution formula involved in the convolution process is as follows:

$$y^{l(i,j)} = f\left(w_i^l \cdot x^{l\left(r^j\right)} + b_i^l\right) = f\left(\sum_{j'=0}^{k-1} w_i^{l(j')} x^{l(j+j')} + b_i^l\right), \quad (19)$$

where $w_i^{l(j')}$ is the j^{th} weight matrix of the i^{th} convolution kernel in layer l; $x^{l(r^j)}$ is the j^{th} convoluted local region in layer l; k is the width of convolution kernel; is the bias terms in layer l and a vector; $f(\cdot)$ is the activation function.

There are five frequently-used activation functions: Sigmoid function, hyperbolic tangent (Tanh) function, rectified linear units (ReLU) function, exponential linear unit (ELU) function and MaxOut function. In this research, the ReLU function is selected as the activation function, because it can solve both explosion and disappearance of the gradient. Meanwhile, the convergence rate of ReLU function is much higher than the sigmoid and tanh functions [23]. The curve diagram of the ReLU function is shown in Fig. 2, which can be written as:

$$ReLU(x) = \max(0, x) = \frac{(x + |x|)}{2}, \quad (20)$$

$$ReLU'(x) = \begin{cases} 0 & x < 0 \\ 1 & x \geq 0 \end{cases}. \quad (21)$$

(2) Pooling layer: Similar to the convolutional layer, the pooling layer is composed of multiple feature maps. Although the number of feature maps is the same as the former layer, the size of each map is smaller. By pooling, the feature vector will be reduced, which leads to the second-extraction of feature data. In this paper, mean pooling is chosen instead of maximum pooling. The number of output feature maps of the pooling layer in CNN can be determined by:

$$Omap_{pool} = \frac{Imap_{pool} - kers}{stride} + 1, \quad (22)$$

where $Omap_{pool}$ is the size of the output feature map of the pooling layer; $Imap_{pool}$ is the size of the feature map of the input pool layer.

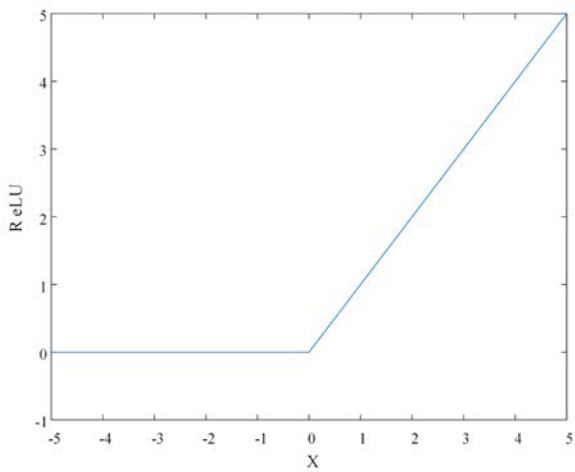

Fig. 2. *ReLU graph*

(3) Fully connected layer: in this layer, each neuron is fully connected with all neurons in the previous layer. The full connection layer can integrate the local information with class discrimination in the output of the pooling layer. The forward propagation in this layer can be represented as:

$$Z_j^{l+1} = \sum\nolimits_{i=1}^{n} W_{ij}^l a_i^l + b_j^l. \quad (23)$$

In the formula, W_{ij}^l is the weight matrix between the i^{th} neuron in layer l and the j^{th} neuron in layer $l+1$; Z_j^{l+1} is the output value of the j^{th} neuron in $l+1$ layer; b_i^l is the bias vector of all neurons in layer l to the j^{th} neuron in layer $l+1$; a_i^l is the output feature maps of l layer.

(4) Output layer: The output layer uses softmax logistic regression to classify the input data. Mathematically speaking, the softmax operation can be described as:

$$p(z)_i = \frac{e^{z_i}}{\sum_{i=1}^{N_c} e^{z_i}}, \quad (24)$$

where $p(z)_i$ represents the probability that z belongs to category i, $i \in N_c$.

1.3 Advantages of CNN for Fault Classification

As mentioned before, CNN can automatically learn the features from the raw data without manual selection. Through training, CNN will optimize the model's parameters and achieve the recognition and classification of data. Because of this characteristic, the original vibration signal can be directly used as input for CNN, which will bring two benefits. 1) By using the raw data, pre-processing of the data can be avoided, which will save time and maximumly ensure the authenticity of data. 2) For the signal processing of a complex system, the selection of feature functions usually requires rich mechanical mathematical knowledge, which means it is difficult for a common technician to extract effective features. However, data features can be extracted directly by using CNN.

The weight sharing of the convolution layer in CNN is the same as sparse connection, which reduces the parameters in the network and lowers the computation time and difficulty. Meanwhile, due to the regularization effect, the stability and generalization ability of network structure are improved, and over-fitting is also avoided [24]. As mentioned before, by pooling layers, the number of neurons in the model will be minimized, and the robustness of translation invariance in input space is improved [25]. Moreover, the structure of CNN is highly extensible, and a deeper layer can be designed in experiments. Therefore, CNN can be used for complex classification due to the ability of fault data extraction.

As a symbolic algorithm of deep learning, CNN can extract high-order features from input data. Specifically, the convolutional layer and pooling layer in the CNN can respond to the translation invariance of input features; in other words, they can identify similar features located in different spatial positions. Therefore, the CNN model has become one of the most popular models by researchers for fault identification and classification.

Since the data samples from the RV reducer are huge and complex, the CNN model is chosen for the fault identification and classification.

2 FAULT DIAGNOSIS METHOD BASED ON CNN

According to the different characteristics of the processing object and the dimension of the input data, CNN is divided into one dimension, two dimensions, and three dimensions, which play a role in different fields. The 2D-CNN weight filters take the dot product of the entire input as they move along the spatial dimension and sum them up. Unlike filters of 1D-CNN, which move in the time dimension, filters of 2D-CNN move in the space dimension, with two dimensions of height and width, which can more accurately and comprehensively extract the features of reconstructed data. In this paper, the 2D-CNN model is used to diagnose the fault data of the RV reducer used in an IR, and the vibration signal is directly used as the input to realize end-to-end fault diagnosis.

2.1 The Data Collection

In this paper, the RV reducer of an IR (model No. BRTIRUS1510A) is chosen as the research subject. There are six types faults: normal, broken teeth of planetary gear A, pitting of sun gear B, broken teeth of planetary gear B, crack of planetary gear B and broken teeth of planetary gear B respectively. For each fault, the rotation speed of the IR maintains 600 r/min without any load. Meanwhile, the motion track of IR will repeat 20 times, which is fixed (maximum motion range). For both motion and accelerate sensors, the sampling frequency is 100 kHz, the sampling time is 20 seconds, which will repeat 10 times. The experimental rig is shown in Fig. 3.

Fig. 3. *Experimental device for data collection*

The experimental design involves six different conditions corresponding to the faults, which includes one healthy mode (NR) and five fault modes (fault 1 to fault 5). Broken teeth are usually divided into fatigue fracture and overload fracture in the reducer, which are caused by fatigue stress and short-term overload or impact load. The pitting of teeth is generated by the teeth with small cracks mesh continuously, which lead to a small piece of metal slides off the tooth surface. The cracks of the teeth in the reducer are mainly triggered by machine overloaded, insufficient design strength, and defective material. Fig. 4 shows an example of a vibration signal acquired in each one of the fault types. The fault categories are listed in Table 1. Fig. 5 shows an example of each one of the five types of faults.

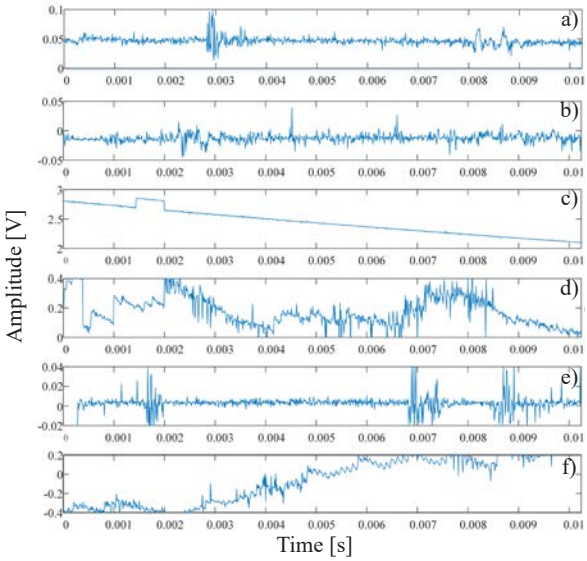

Fig. 4. *Vibration signals; a) normal, b) fault 1, c) fault 2, d) fault 3, e) fault 4, and f) fault 5*

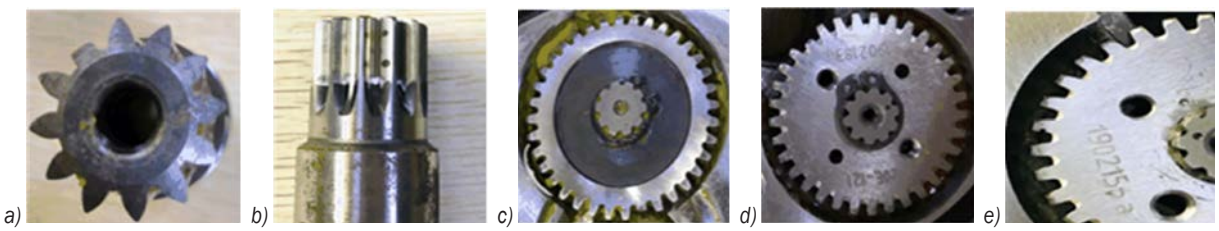

Fig. 5. *Five fault conditions; a) broken tooth in sun gear B, b) pitting in sun gear B, c) broken tooth in planetary gear A, d) cracking in planetary gear B, and e) cracking in planetary gear B*

Table 1. *Fault categories*

	Serial number	Fault type	Fault location	Degree of fault
Normal	NR	None	None	\
Planetary gear A	Fault 1	Broken teeth	Fault of tooth breakage of the second shaft RV40E-121 planetary gear	Completely broken teeth
Sun gear B	Fault 2	Pitting	Tooth pitting failure of the third shaft RV20E-121 sun gear	Moderate
	Fault 3	Broken teeth	Tooth breakage fault of the third shaft RV20E-121 sun gear	Completely broken teeth
Planetary gear B	Fault 4	Crack	Crack fault of the third shaft RV20E-121 planetary gear teeth	Width 0.5 mm Depth 0.5 mm
	Fault 5	Broken teeth	Fault of tooth breakage of the third shaft RV20E-121 planetary gear	Completely broken teeth

In this paper, for each fault, there will be 6×1000 samples. Among them, 4200 will be chosen for training, and the rest will be used for verification.

2.2 Experimental Environment

The hardware and software settings of this experimental environment are shown in Table 2.

Table 2. *Development environment*

Hardware	Configuration or installation information
Processor	Intel(R) Core(TM) i7-6700 CPU @3.40GHZ 3.41GHz
RAM	8.0 GB
Operating system	Windows 10 Professional 64-bit
Compilation environment	MATLAB R2018a

2.3 Data Processing

There are 6000 samples in this paper, and each sample has 1024 data points (i.e. 1024×1). The model used in this paper is 2D-CNN, so one-dimensional data is changed into two-dimensional data (i.e. 32×32×1) by pre-processing. Then, after 2D-FFT processing, the time domain diagram is changed into the frequency domain diagram, as shown in Fig. 6. The 2D-FFT is usually calculated by the row and column decomposition algorithm; in other words, by using its separability, the two-dimensional FFT is divided into row-oriented FFT and column-oriented FFT and then calculated in sequence. Generally speaking, the row-column sequence of 1D-FFT algorithm has no great influence on the operation results of 2D-FFT, as long as the row-oriented FFT and column-oriented FFT can be calculated separately. The Fourier transform can transform the signal from time domain to frequency domain, and then study the spectrum structure and variation rule of the signal. Some signals in the time domain have more obvious features in the frequency domain, which enables the CNN model to extract data features more accurately.

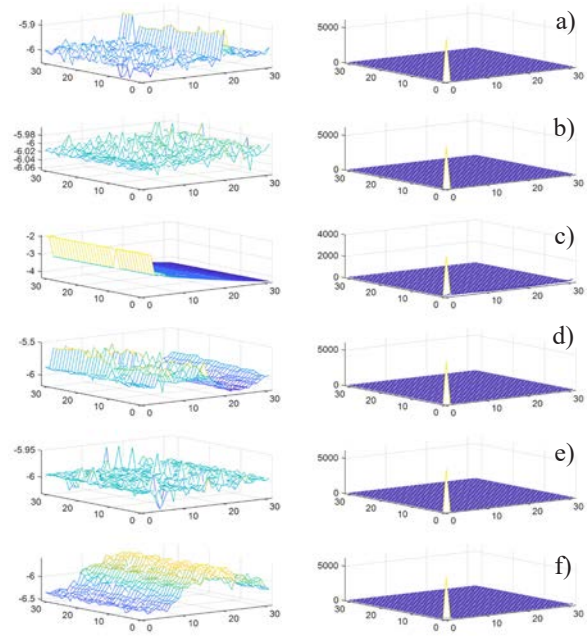

Fig. 6. *2D raw data and frequency domain diagram; a) normal, b) fault 1, c) fault 2, d) fault 3, e) fault 4, and f) fault 5*

2.4 Model Design

The CNN model used in this paper is shown in Fig. 7, which consists of an input layer, convolution layer C1, pooling layer P2, convolution layer C3, pooling layer P4, fully connected layer and output layer. The activation function of the convolution layer is the ReLU function, the pooling layer adopts mean pooling, and the fully connected layer contains 250 processing units.

In order to automatically adapt to the different characteristics of vibration signals, the key parameters of CNN need to be optimized. The parameters of the network layer structure, convolution kernel size, number of iterations, learning rate, number of

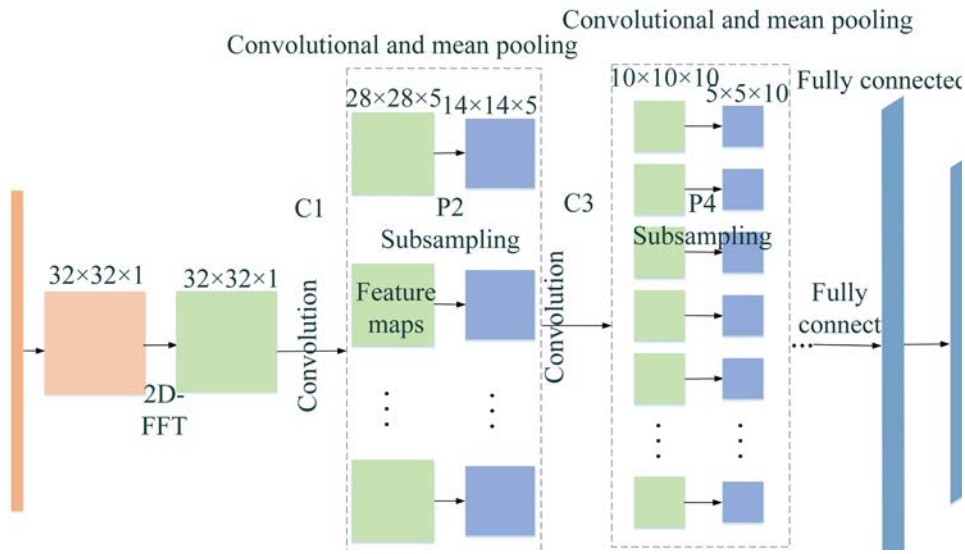

Fig. 7. *CNN framework diagram used in this paper*

Table 3. *Parameters of CNN model*

Layers	Types	Model parameters	Training parameters
2	Convolutional layer	Filter width = 5, Filter height = 5, Filter channel = 1, Filter number = 5, Bias = 5	Minibatch size = 200 Learning rate = 0.01 Momentum = 0.1 Max epochs = 300 Training sample rate = 70 % Activation='ReLU'
3	Pooling layer	Sub-sampling rate = 2	
4	Convolutional layer	Filter width = 5, Filter height = 5, Filter channel = 5, Filter number = 10, Bias = 10	
5	Pooling layer	Sub-sampling rate = 2	
6	Full-connected layer	250 nodes	
7	Softmax classifier	6 outputs	

convolution kernels, activation function, and pooling method all need to be adjusted. The optimal structure parameters are shown in Table 3.

The diagnosis process proposed in this paper is shown in Fig. 8, and the processing steps are listed as follows:

Step 1: Collecting vibration signals of different faults from the RV reducer through sensors installed on the machine;

Step 2: Pre-process each kind of fault data and divide it into training samples and test samples;

Step 3: Carrying out two-dimensional Fourier transform on the data;

Step 4: Initializing the 2D-CNN model;

Step 5: Fine-tuning the parameters;

Step 6: Learning the features of the training samples by 2D-CNN model, and then using the trained model for fault diagnosis of the test samples;

Step 7: Output the fault diagnosis results.

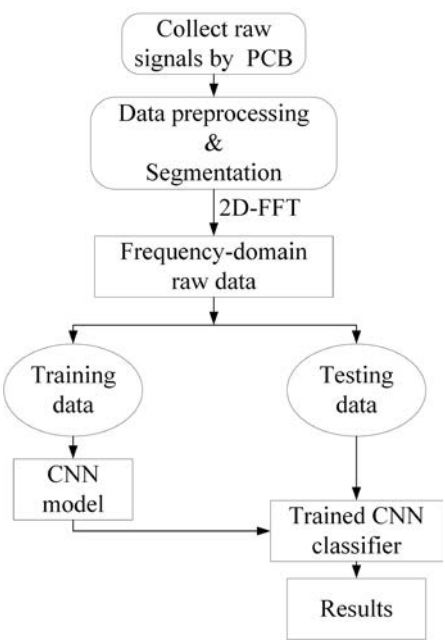

Fig. 8. *Fault diagnosis flow chart of CNN*

2.5 Experimental Results

The 2D-CNN model designed in this paper is used to classify six kinds of fault data of robots, and the classification results of test sets are shown in Table 4.

Table 4. *Fault classification results of test sets*

Fault category	Sample size	Accuracy [%]
NR	300	99
1	300	100
2	300	99.33
3	300	100
4	300	100
5	300	99.67
Overall accuracy		99.67

Based on the above table, the proposed CNN model in this paper can achieve 99.67 % overall accuracy in recognition rate. For Fault 1, Fault 3, and Fault 4, the recognition rate can reach 100 %. The accuracy of normal data is 99 %, the accuracy of Fault 2 is 99.3 %, and the accuracy of Fault 5 is 99.67 %. It can be seen from Table 4 that the classification accuracy rate of Fault 2 is the lowest, and Fault 2 is pitting. As shown in Figure 4, the vibration signal of Fault 2 is quite different from the other four fault signals.

All the results indicate that the CNN model is an effective method for fault classification of a reducer on an industrial robot (IR).

3 SIMULATION COMPARISON

To further verify the efficiency of the proposed method, simulations of comparison are carried out in this paper. Four mainstream methods are chosen as comparative subjects, which are 1D-CNN, DBN, Stacked AutoEncoder (SAE), RNN and Neural Network (NN), respectively.

Similar to 2D-CNN, 1D-CNN can automatically extract feature data through weight sharing to avoid overfitting. Table 5 shows the parameters of the 1D-CNN model used in this paper.

Table 5. *Parameters of 1D-CNN model*

Parameter	Value
Con1	Omaps = 5; kers = 15; actv = 'sigm'
Pool1,2	Scale = 5; pool = 'mean'
Con2	Omaps = 5; kers = 13; actv = 'sigm'
Numepochs	500
Batchsize	50
Learning rate	0.015
Output layer	Softmax

DBN is a probabilistic generative model, which is formed by stacking several restricted Boltzmann machines (RBM) [26]. Its training process is to use unsupervised greedy layer-wise pre-train to obtain weights. The bottom layer is mainly used to receive the input data and transform the input data into a hidden layer through RBM, that is, the input of higher layer RBM comes from the output of lower layer RBM. Stacked RBM networks form a DBN model to extract the features of fault data, and then the classifier is used for classification. Table 6 shows the parameters of the DBN model used in this paper.

Table 6. *Parameters of DBN model*

Parameter	Value
Dbnsizes	10×10
Learning rate	0.000003
Numepochs	500
Batchsize	100
Momentum	0.00001
Activation function	tanh
Output layer	Softmax

SAE is a deep neural network model composed of multi-layer AutoEncoder (AE), and AE is a three-layer unsupervised nonlinear neural network for feature extraction, including input layer, hidden layer, and output layer. The key idea of SAE is to let the network learn the features of input data in an unsupervised way [27]. Firstly, the greedy layer-wise training method is used to train the SAE network unsupervised, and the features of the fault data are obtained. Then, the trained SAE is connected with the softmax layer to classify the fault data of the test set. Table 7 shows the parameters of the SAE model used in this paper.

NN is composed of the input layer, hidden layer, and output layer, the latter of which have only one layer, and the number of hidden layers can be arbitrary. The input layer is introduced from the instance feature vectors in the training set, and is transferred to the next layer according to the weights between the connection points. Table 8 shows the parameters of the NN model used in this paper.

Table 7. *Parameters of SAE model*

Parameter	Value
Hidden layer	100
Numepochs	20
Batchsize	200
InputZeroMaskedFraction	0.5
Learning rate	0.0026
Activation function	tanh
Output layer	Softmax

Table 8. *Parameters of NN model*

Parameter	Value
Hidden layer	100
Numepochs	500
Batchsize	100
Momentum	0.5
Learning rate	0.21
Scaling_learningrate	1
Activation function	sigm
Output layer	Logistic

Six types of RV reducer data (one normal data and five fault) are collected in our experiments. The diagnosis results are shown in Table 9 and Fig. 9.

The fault diagnosis accuracy of five tests is shown in Fig. 9. It can be seen from the figure that the accuracy of fault diagnosis results of the 2D-CNN model is the highest, with the highest being 100 % and the lowest being 99.33 %, followed by 1D-CNN, NN and SAE. DBN performed the worst in these models.

Table 9 shows the average classification accuracy of the above five methods. In the classification performance, the fault classification method based on 2D-CNN has achieved better classification performance than other deep networks, and its average accuracy can reach 99.67 %. 1D-CNN's classification effect is ranked after 2D-CNN, and its average classification accuracy is 98.46 %. NN's classification effect is inferior to that of 1D-CNN, and its average classification accuracy is 83.47 %. The classification performance of SAE based on AEs is general, and the average accuracy of SAE is 83.05 %. The classification accuracy of DBN based on RBMs is low, and the average classification accuracy of DBN is only 58.08 %. To summarize, the 2D-CNN-based classification method has the highest average

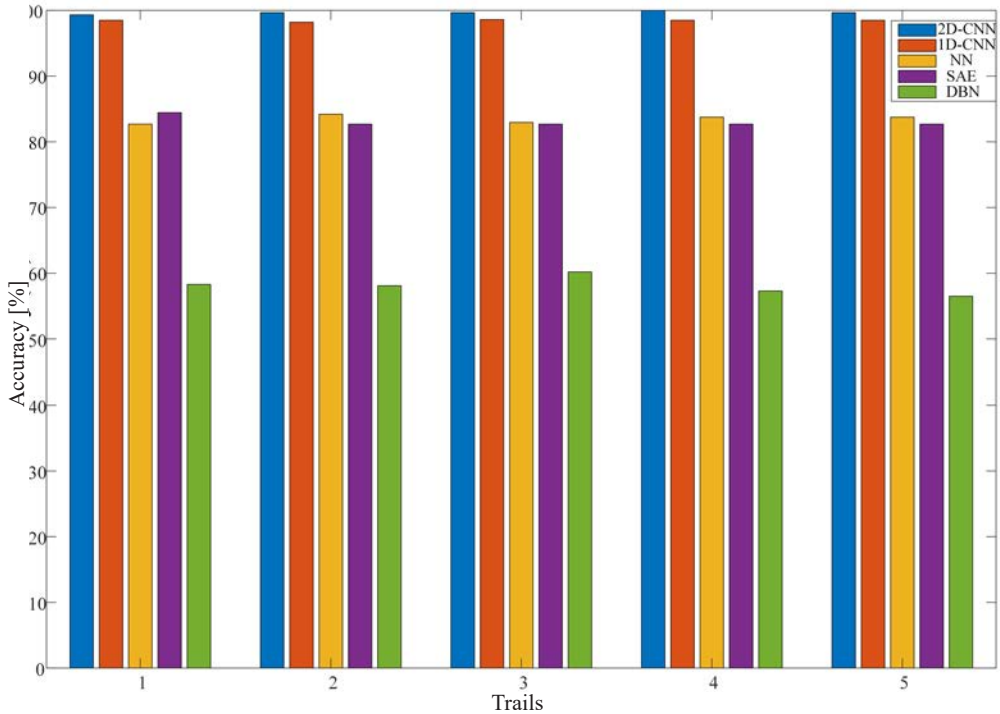

Fig. 9. *Comparison of model accuracy*

accuracy among the five methods, which is 1.21 % higher than 1D-CNN, 16.2 % higher than NN, 41.59 % higher than DBN and 16.62 % higher than SAE.

Table 9. *Mean accuracy of model*

Model	Mean accuracy [%]
2D-CNN	99.67
1D-CNN	98.46
DBN	58.08
NN	83.47
SAE	83.05

4 CONCLUSION

As a key component of industrial robots, the RV reducer often has various faults due to its bad operating environment. The failure of the reducer can bring huge economic losses to a company and even lead to serious casualties in some extreme cases. Therefore, the fault detection and diagnosis of the reducer is very important. In order to solve this problem, a 2D-CNN based on the experimental vibration data after 2D-FFT is proposed for the fault diagnosis of RV gear for IR. In the proposed algorithm, the time-frequency transformation of the original data is firstly performed by the 2D-FFT. Secondly, the convolutional layer and pooling layer of 2D-CNN are used to extract the fault features contained in the data. Finally, the Softmax layer classifies the extracted features.

2D-CNN can automatically learn the features in the data, and it has three features: 1) The spatial connection of data is local. Each neuron does not need to perform convolution computation on all the data. The global information can be obtained by integrating different local neurons obtained by convolution computation at a higher level, which can reduce the number of connections; 2) The weight sharing between different neurons can reduce the parameters that need to be solved, and multiple feature maps can be obtained by using multiple filters to convolute the input data; 3) Subsampling can reduce the amount of data to be processed while retaining useful information. These features are conducive to improving the efficiency of network training.

The proposed method is applied to the rotation vector reducer for industrial robots. The data used in this paper include one normal data and five fault data, and the diagnosis accuracy reaches 99.67 %. However, the comparison models include 1D-CNN, DBN, NN, SAE. And their accuracy rates are 98.46 %, 58.08 %, 83.47 %, 83.05 %, respectively. Experimental results show that, compared with other peer models, the proposed model has good fault diagnosis accuracy.

5 ACKNOWLEDGMENTS

This research is supported by National Natural Science Foundation of China (51905058), Natural Science Foundation of Chongqing (cstc2020jcyj-msxmX0182, cstc2019jcyj-zdxmX0013), Key Project of Technology Innovation and Application of Chongqing (cstc2019jscx-fxydX0077), Research Start-Up Funds of Chongqing Technology and Business University (1856018), Key Research Platform Project of Chongqing Technology and Business University (ZDPTTD201918). The authors also gratefully acknowledge the helpful comments and suggestions of the reviewers, which have improved the presentation.

6 REFERENCES

[1] Eguchi, K., Wu, Q., Liu, Y., Wu, C., Chen, T. (2018). An overview of current situations of robot industry development. *ITM Web of Conferences*, vol. 17, **DOI:10.1051/itmconf/20181703019**.

[2] Zhang, R., Zhang, C., Zheng, W. (2018). The status and development of industrial robots. *Materials Science and Engineering*, vol. 423, art. ID 012051, **DOI:10.1088/1757-899X/423/1/012051**.

[3] Chen, J. (2018). Industrial robot technology and its typical application analysis. *Journal of Electronic Research and Application*, vol. 2, no. 2, **DOI:10.26689/jera.v2i3.379**.

[4] Li, T., Xu, H., Tian, M. (2020). A loaded analysismethod for rv cycloidal-pin transmission based on the minimum energy principle. *Strojniški vestnik - Journal of Mechanical Engineering*, vol. 66, no. 11, p. 655-667, **DOI:10.5545/sv-jme.2020.6868**.

[5] Girshick, R., Donahue, J., Darrell, T., Malik, J. (2014). Rich feature hierarchies for accurate object detection and semantic segmentation. *IEEE Conference on Computer Vision and Pattern Recognition*, vol. 1, p. 580-587, **DOI:10.1109/CVPR.2014.81**.

[6] Tompson, J., Goroshin, R., Jain, A. (2015). Efficient object localization using convolutional networks. *IEEE Conference on Computer Vision and Pattern Recognition*, p. 648-656, DOI:10.1109/CVPR.2015.7298664.

[7] Pan, H., He, X., Tang S., Meng, F. (2018). An improved bearing fault diagnosis method using one-dimensional CNN and LSTM. *Strojniški vestnik - Journal of Mechanical Engineering*, vol. 64, no. 7-8, p. 443-452, **DOI:10.5545/sv-jme.2018.5249**.

[8] Janssens, O., Slavkovikj, V., Vervisch, B., Stockman, K., Loccufier, M., Verstockt, S., Van de Walle, R., Van Hoecke, S. (2016). Convolutional neural network based fault detection for rotating machinery. *Journal of Sound and Vibration*, vol. 377, p. 331-345, **DOI:10.1016/j.jsv.2016.05.027**.

[9] Jing, L., Zhao, M., Li, P., Xu, X. (2017). A convolutional neural network based feature learning and fault diagnosis method for the condition monitoring of gearbox. *Measurement*, vol. 111, p. 1-10, **DOI:10.1016/j.measurement.2017.07.017**.

[10] Azamfar, M., Singh, J., Bravo-Imaz, I., Lee, J. (2020). Multisensor data fusion for gearbox fault diagnosis using 2-D convolutional neural network and motor current signature analysis. *Mechanical Systems and Signal Processing*, vol. 144, art. ID 106861, **DOI:10.1016/j.ymssp.2020.106861**.

[11] Qiu, G., Gu, Y., Cai, Q. (2019). A deep convolutional neural networks model for intelligent fault diagnosis of a gearbox under different operational conditions. *Measurement*, vol. 145, p. 94-107, **DOI:10.1016/j.measurement.2019.05.057**.

[12] Chen, Z., Mauricio, A., Li, W., Gryllias, K. (2020). A deep learning method for bearing fault diagnosis based on cyclic spectral coherence and convolutional neural networks. *Mechanical Systems and Signal Processing*, vol. 140, p. **DOI:10.1016/j.ymssp.2020.106683**.

[13] Wang, S., Chen, H. (2019). A novel deep learning method for the classification of power quality disturbances using deep convolutional neural network. *Applied Energy*, vol. 235, p. 1126-1140, **DOI:10.1016/j.apenergy.2018.09.160**.

[14] Xuan, W., You, G. (2020). Detection and diagnosis of pancreatic tumor using deep learning-based hierarchical convolutional neural network on the internet of medical things platform. *Future Generation Computer Systems*, vol. 111, p. 132-142, **DOI:10.1016/j.future.2020.04.037**.

[15] Meng, M., Chua, Y. J., Wouterson, E. and Kong, C. P. K. (2017). Ultrasonic signal classification and imaging system for composite materials via deep convolutional neural networks. *Neurocomputing*, vol. 257, p. 128-135, **DOI:10.1016/j.neucom.2016.11.066.**

[16] Lu, Y., Yi, S., Zeng, N., Liu, Y., Zhang, Y. (2017). Identification of rice diseases using deep convolutional neural networks. *Neurocomputing*, vol. 267, p. 378-384, **DOI:10.1016/j.neucom.2017.06.023**.

[17] Qian, H. M., Li, Y.F., Huang, H.Z. (2020). Time-variant reliability analysis for industrial robot RV reducer under multiple failure modes using Kriging model. *Reliability Engineering & System Safety*, vol. 199, art. ID 106936, **DOI:10.1016/j.ress.2020.106936**.

[18] Rumelhart, D.E., Hinton, G.E., Williams, R.J. (1987). Learning Internal Representations by Error Propagation. In *Parallel Distributed Processing: Explorations in the Microstructure of Cognition: Foundations*, vol. 1, p. 318-362.

[19] Rumelhart, D.E., Hinton, G.E., Williams, R.J. (1986). Learning representations by back-propagating errors. *Nature*, vol. 323, p. 533-536, **DOI:10.1038/323533a0**.

[20] Gu, J., Wang, Z., Kuen, J., Ma, L., Shahroudy, A., Shuai, B., Liu, T., Wang, X., Wang, G., Cai, J., Chen, T. (2018). Recent advances in convolutional neural networks. *Pattern Recognition*, vol. 77, p. 354-377, **DOI:10.1016 /j.patcog.2017.10.013**.

[21] LeCun, Y., Bottou, L., Bengio, Y., Haffner, P. (1998). Gradient-based learning applied to document recognition. *Proceedings of the IEEE*, vol. 86, no. 11, p. 2278-2324, **DOI:10.1109/5.726791**.

[22] Krizhevsky, A., Sutskever, I., Hinton, G.E. (2017). ImageNet classification with deep convolutional neural networks. *Communications of the ACM*, vol. 60, p. 84-90, **DOI:10.1145/3065386**.

[23] Xu, B., Wang, N.Y., Chen, T.Q., Li, M. (2015). Empirical evaluation of rectified activations in convolution network. *Computer Science*.

[24] O'Shea, K., Nash, R. (2015). An introduction to convolutional neural networks. *Computer Science*.

[25] Huang, J.T., Li, J.Y., Gong, Y.F. (2015). An analysis of convolutional neural networks for speech recognition. *IEEE International Conference on Acoustics. Speech and Signal Processing*, p. 4989-4993, **DOI:10.1109/ICASSP.2015.7178920**.

[26] Xu, F., Fang, Z., Tang, R., Li, X., Tsui, K.L. (2020). An unsupervised and enhanced deep belief network for bearing performance degradation assessment. *Measurement*, vol. 162, art. ID 107902, **DOI:10.1016/j.measurement.2020.107902**.

[27] Vincent, P., Larochelle, H., Lajoie, I, Bengio, Y., Manzagol, P.-A. (2010). Stacked denoising autoencoders: learning useful representations in a deep network with a local denoising criterion. *Journal of Machine Learning Research,* vol. 11, p. 3371-3408.

Strojniški vestnik - Journal of Mechanical Engineering 67(2021)10, 501-515

DOI:10.5545/sv-jme.2021.7300 Original Scientific Paper
Received for review: 2021-06-24
Received revised form: 2021-09-05
Accepted for publication: 2021-09-21

Response Analysis of a Scraper Conveyor under Chain Faults Based on MBD-DEM-FEM

Zisheng Wang[1,2] – Bo Li[1,2] – Chao Liang[1,2] – Xuewen Wang[1,2,*] – Jiahao Li[1,2]

[1] Taiyuan University of Technology, College of Mechanical and Vehicle Engineering, China
[2] Shanxi Key Laboratory of Fully Mechanized Coal Mining Equipment, China

To tackle the difficulty in obtaining the response data of chain and bulk coal under chain faults, this paper uses a new method for the fault simulation of scraper chains based on the coupling of multi-body dynamics (MBD), discrete element method (DEM), and finite element method (FEM). With the force and stacking angle as response values, the contact parameters of bulk coal were revised using a rotary transport test. The simplified DEM-MBD model was verified from the resistance using the point-by-point method. The static structure model of the chain was verified by the chain tensile experiment. The DEM-MBD coupling results show that when the chain is stuck or broken, the dynamic properties of the chain and bulk coal fluctuate sharply, and the wear of the medium plate increases. Based on the DEM-MBD coupling results and the DEM-FEM unidirectional coupling, the stress, strain and life were acquired, and were verified experimentally. Regarding the fracture, the Plackett-Burman test was used to determine that the crack depth, initial angle, and tensile load significantly affect the stress intensity factor (SIF). The quadratic model between significant factors and SIF was constructed using the response surface method, which provides a reference for the simulation of the scraper conveyor, the fault mechanism, and the optimization of the design of the chain.

Keywords: multi-body dynamics, discrete element method, finite element method, scraper chain fault, stress intensity factor, response surface method

Highlights

- *A method for the fault simulation of a scraper conveyor based on the MBD-DEM-FEM was proposed.*
- *The contact parameters of bulk coal were revised from the force and stacking angle using the response surface method.*
- *The response data of the chain and bulk coal under chain faults were obtained.*
- *The interactions between factors on stress intensity factor were analysed using the response surface method.*

0 INTRODUCTION

As the core structure of the scraper conveyor, the scraper chain is subject to frequent faults, which seriously threatens the safety of workers and the mining efficiency of coal mines [1]. For satisfying the high requirements of intelligent coal mines for scraper chains, it is not feasible to perform fault tests on actual scraper conveyors or scaled models to obtain real-time data. This method is costly, and it is difficult to extract data. Consequently, safety cannot be guaranteed due to the uncertainty of fault. The simulation method based on computer aided design has low cost and high safety factor, and can reproduce the fault state realistically. The common simulation methods include finite element method (FEM), multi-body dynamics (MBD), and discrete element method (DEM).

FEM is based on the idea of discretization and numerical approximation to solve problems [2]. Based on the simplified chain transmission model, researchers have obtained the stress, strain, [3] and [4] and fatigue life [5] of chains under different conditions through transient dynamics or static structural analysis. However, the finite element analysis (FEA) based on the simplified model puts higher demands on the boundary conditions. The accuracy of boundary conditions set only by finite element software is not high but can be enhanced by coupling with DEM [6] and MBD.

MBD focuses on the kinematic and dynamic behaviour of multi-body systems and the mechanical interaction between parts. The velocity and vibration characteristics of the scraper chain under chain stuck and breaking faults were gained by Jiang et al. [7]. Xie et al. [8] discussed the torsional pendulum and vibration characteristics of the chain under chain stuck fault. With the maturity of flexible technology, scholars have made the chain flexible to obtain the stress and deformation [9] and [10]. Previous studies rarely considered the role of bulk coal or only replaced it with a constant load, ignoring the distribution and time-varying characteristics of bulk coal. However, the force and movement of bulk coal under fault conditions may worsen the fault and accelerate the failure of parts.

Considering the discrete characteristics of bulk coal [11], DEM has been applied to research the transport state of scraper conveyors [6] and [12] and the failure of key parts [13] and [14]. Researchers have improved the reliability of simulation by modifying

*Corr. Author's Address: College of Mechanical and Vehicle Engineering, Taiyuan University of Technology, Taiyuan, China, wxuew@163.com

parameters [15] and [16] and coupling simulation. The MBD-DEM bidirectional coupling model of scraper conveyor was established by Zhang et al. [17] to realize real-time sharing of information between bulk coal and rigid bodies.

The surface cracks caused by the synergy of complex factors such as wear, corrosion, and deformation are reasons for the fatigue fracture of the chain [18]. It is necessary to discuss the initiation and propagation of cracks. The stress intensity factor (SIF) is a fracture parameter that characterizes the stress field at the crack front, which is affected by the size and shape of the crack. Xue et al. [19] investigated the effects of crack depth and position on fracture parameters through the single factor test, which does not involve the interaction between the factors controlling the fracture of chains. The response surface method (RSM) is an optimization method combining mathematical statistics and modelling [20]. The effects of interaction on the response value can be investigated.

It can be seen that the advantages of each method can compensate for the deficiencies of other methods, so this study used a new method for the fault simulation of a scraper conveyor based on the coupling of MBD-DEM-FEM. First, the MBD-DEM coupling model was established and verified to gain the response characteristics of chain and bulk coal under chain stuck and breaking faults. Combining the above results and DEM-FEM coupling, this study obtained the stress, strain, and life of the chains. For the fracture failure, through single factor testing and response surface testing, the single and interactive effects of crack depth, initial angle, and tensile load on the SIF were investigated. This provides a reference for the simulation of scraper conveyors, and the fault mechanism and optimization design of the chain.

1 SIMULATION MODELS AND TEST

1.1 Dynamic Model

The coupling simulation with the complete length of the scraper conveyor (SGZ880/800) is not workable [17], so the dynamic model is simplified as necessary. When the chain is stuck or broken, the chain far from the fault point will not respond in a short time. Therefore, only three middle troughs, scraper chains, and drive sprockets are retained; the retarder, hydraulic coupler, and drive motor are removed, and the bottom chute for the return of the chains is added. The simplified model is 5 metres long, as shown in Fig. 1. In the pre simulation, the sprockets drove the scraper chains to run smoothly, which satisfied the desired motion characteristics. The kinematic pairs and contacts of components were set up in RecurDyn dynamic software. The stiffness and damping coefficients of contacts between parts were adjusted by pre-simulation to be 600000 $N \cdot mm^{-1}$ and 1000 $N \cdot (mm/s)^{-1}$.

1.2 Construction and Modification of Bulk Coal

1.2.1 Model of Coal Particle

The three typical shapes of coal particles were built by the spherical filling method [21], shown in Fig. 2. In order to obtain the contact characteristics of the bulk coal with the scraper chain and the medium plate more accurately, coal with large (50 mm to 100 mm), medium (25 mm to 50 mm), and small (13 mm to 25 mm) sizes was generated by the particle factory fixed above the machine tail, and the mass proportions of three sizes are 0.25, 0.4, and 0.35.

Hertz-Mindlin (no slip) [22] and Hertz-Mindlin with Archard wear [14] were chosen for the contact models between particles and between particles and rigid bodies, respectively. The intrinsic parameters

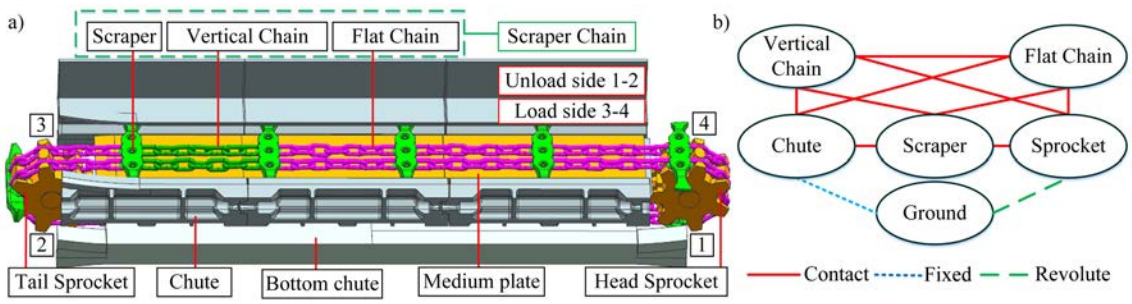

Fig. 1. *The mechanical relationship of simplified model; a) simplified model; and b) mechanical relationship*

measured by the group members through the designed experiments are listed in Table 1 [16].

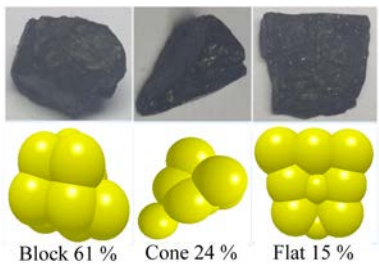

Fig. 2. *The shapes and mass proportions of particles*

Table 1. *The intrinsic parameters*

Parameters	Steel	Coal
Shear modulus [MPa]	800	470
Poisson's ratio	0.3	0.3
Density [kg·m^{-3}]	7850	1229

1.2.2 Modification of Contact Parameters

In current research, the calibration tests of coal particle parameters take the stacking angle at rest as the response variable. During the conveying process, the behaviour of bulk coal is not only macroscopic accumulation on the chutes, but also the mechanical interaction with the scraper conveyor. Therefore, it is necessary to modify the contact parameters of coal particles through the bulk coal transportation test with force and accumulation as the response variables.

Using the actual scraper conveyor to carry out the transportation test is not feasible. Based on the transport principle, the rotary transport testing machine shown in Fig. 3a was designed. The upper sample has a wedge structure with the same slope as the scraper, as shown in Fig. 3e, and the material of the upper sample is 42CrMo (C: 0.38 % to 0.45 %), which is the same as the scraper. The lower samples are six fan-shaped plates with positioning holes, as shown in Fig. 3f, and the material of the lower samples is 16Mn (C: 0.13 % to 0.19 %), which is commonly used in the medium plate. The three-dimensional force sensor and the upper sample are fixed with the rack through the clamp, and the lower samples are fixed with the trough through the positioning holes. After the bulk coals with the required mass and size are paved in the trough, the motor drives the trough to rotate at a uniform angular velocity of 10 rad·s^{-1}. The linear velocity of the position where the upper sample is located is the same as that of the scraper chain (1.1 m·s^{-1}), as shown in Fig. 3c. The bulk coals are pushed by the upper sample and accumulate around the sample, which is consistent with the principle of scraper transportation in actual work, as shown in Fig. 3c. The force on the upper sample when pushing the bulk coals was measured through the force sensor, as shown in Fig. 4. The stacking angle obtained using an image-processing program written in Matlab is 38.59°.

Through Plackett-Burman and response surface tests, the quadratic polynomials between force, stacking angle and significant terms were established. The contact parameters obtained by solving the polynomials with the experimental force and stacking angle as the target values are shown in Table 2. Finally, the accuracy and applicability of the parameters were verified through tests under different transport conditions.

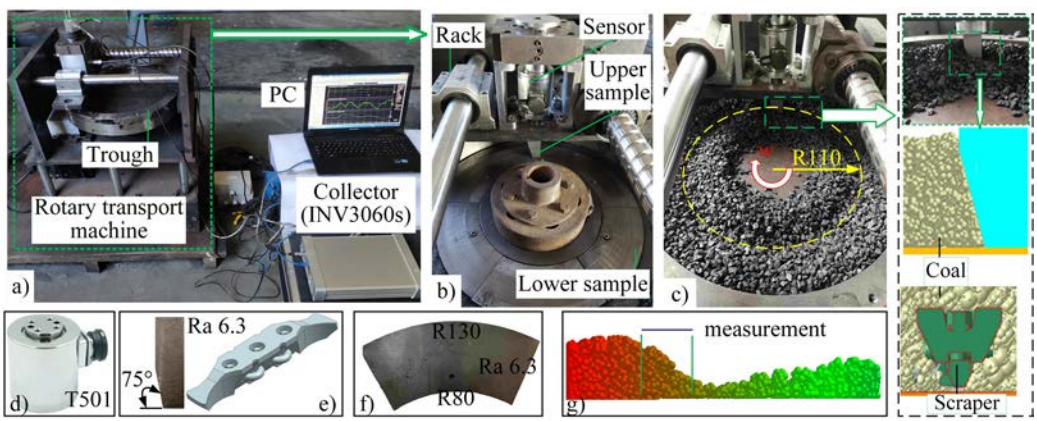

Fig. 3. *The test equipment and principle; a) test equipment; b) the rotary transport machine; c) test principle; d) three-dimensional force sensor; e) upper sample; f) lower sample; g) accumulation around the upper sample*

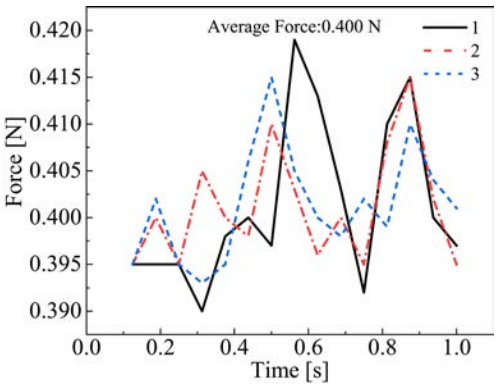

Fig. 4. *The force on the upper sample*

Table 2. *The corrected contact parameters*

Parameters	Coal-Steel	Coal-Coal
Coefficient of restitution	0.65	0.64
Coefficient of static friction	0.401	0.333
Coefficient of rolling friction	0.032	0.041

1.3 DEM-MBD Coupling Simulation

1.3.1 Verification of DEM-MBD Coupling Model

Due to the short laying length, there is a gap in the speed and tension with the actual situation. The point-by-point method is used to calculate the resistance of long-distance continuous conveying machinery; its main principle is shown in Eq. (1). This research focuses on the fault response of the scraper chain in the chutes, so it only verified the resistance of the loaded side (Points 3 and 4 in Fig. 1) and unloaded side (Points 1 and 2 in Fig. 1), which were calculated based on the parameters of the conveyor to be 348.9 kN and 35.3 kN respectively **[23]**.

$$F_i = F_j + W_{ij}, \tag{1}$$

where F_i [N] is the tension at the front point, F_j [N] is the tension at the back point, W_{ij} [N] is the running resistance.

The engagement and separation points of the sprockets and the chains are often selected as measuring points, as shown in Fig. 1. The DEM-MBD simulation was carried out under normal conditions to extract the chain tension at four points. According to Eq. (1), the simulation values of the running resistance on the load side and the unloaded side were calculated, and the comparison with the theoretical resistance is listed in Table 3, the relative error under no-load and full-load is less than 8 %, which testifies that the simplified model can reflect the mechanical characteristics of scraper conveyor.

Table 3. *The comparison between theoretical resistance and tension difference*

Items	No-load		Full-load	
	$i = 4$ $j = 3$	$i = 2$ $j = 1$	$i = 4$ $j = 3$	$i = 2$ $j = 1$
W_{ij} [kN]	35.2	35.2	348.8	35.2
ΔF_{ij} [kN]	33.7	34.6	321.7	35.3
Relative error [%]	4.26	1.70	7.77	0.28

The chain tension at the middle section of the scraper conveyor provided by the cooperative enterprise (Yaxing Anchor Chain) is about 210 kN to 223 kN; the simulation tension is about 200 kN, and the maximum relative error between them is 10.3 %.

The velocity curve of the chain under full-load condition is shown in Fig. 5, which reveals the fluctuation of "decrease–increase" after the velocity is accelerated. It conforms to the polygon effect **[24]** and validates the kinematics characteristics of simplified model.

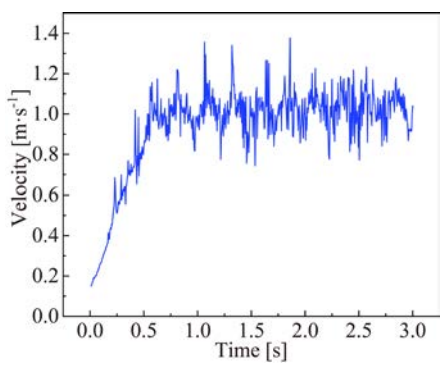

Fig. 5. *The velocity of scraper chain*

1.3.2 Design of Fault Conditions

Chain breaking and chain stuck are the most frequent faults **[25]**. The small preload, rib spalling of coal wall, and coal blocks stuck at the connection of chutes can cause the chains to jam: we added irregular obstacles in the chute to simulate the chain stuck fault in dynamics software. The increased chain pitch caused by wear, the extreme impact load, the long-term over-carrying and the fatigue crack generated by the synergy of corrosion and other factors can cause the chain to break; we did not deal with the stuck fault in time and set the simulation script for the contact between chain links to simulate chain breaking fault in dynamics software.

1.4 Experimental Verification of FEA Model

1.4.1 FEA Model of Chain

The FEA model shown in Fig. 6 was employed to solve the non-linear contact between chain links. The size of the chain link made of 23MnNiCrMo54 (C: 0.22 %) is Φ 34 mm × 126 mm; the properties of the material are listed in Table 4, and the S-N curve is $NS^{2.49} = 1.30066 \times 10^{10}$. The entire model was divided into tetrahedral mesh sized 6 mm, yielding 50,997 elements with 76,070 nodes. The frictional contacts were set between the flat chains and the vertical chain, and the coefficient of friction is 0.2. The right surfaces of flat chain 2 were subjected to boundary loads based on the coupling results, while the left surfaces of flat chain 1 were fixed. The pressure of coal was distributed on vertical chain 1 according to the pressure file derived from EDEM software.

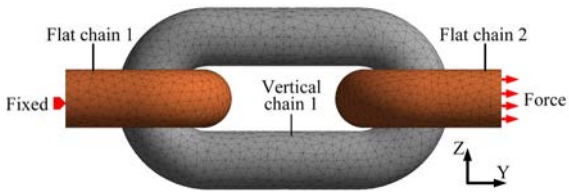

Fig. 6. *The FEA model of the chain*

Table 4. *The mechanical properties of 23MnNiCrMo54*

Properties	Value
Density [kg·m^{-3}]	7860
Young's modulus [GPa]	210
Poisson's ratio	0.3
Tangent modulus [MPa]	2444
Yield strength [MPa]	1166
Tensile yield strength [MPa]	1254

1.4.2 Experimental verification

The tensile testing machine (LAW-5000) was used to obtain the elongation rate of the chain under the test load (1160 kN to 1276 kN), as shown in Fig. 7, and the experiment was repeated three times. Based on the model in Fig. 6, the simulation value of the elongation rate is 1.33 %. The comparison between the experimental value and the simulated value is shown in Table 5. It can be seen from Table 5 that the relative error does not exceed 5 %.

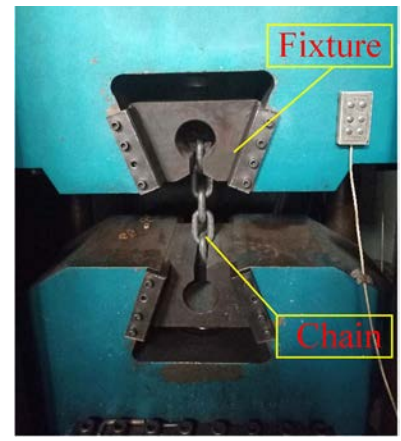

Fig. 7. *The microcomputer controlled electro-hydraulic servo tensile testing machine (LAW-5000)*

Table 5. *The comparison between experimental and simulation values of elongation*

Number	Experimental value [%]	Simulation value [%]	Relative error [%]	Average relative error [%]
1	1.40	1.33	5.00	4.07
2	1.36		2.20	
3	1.40		5.00	

2 SIMULATION RESULTS

When the scraper chains are stuck or broken, the scraper de flects due to the uneven force on both ends, as illustrated in Fig. 8. The surrounding of the deflected scraper is divided into four areas, in which PQ is the stuck side and RS is the deflected side.

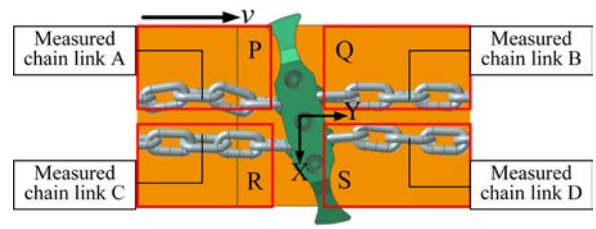

Fig. 8. *The areas around the deflected scraper*

2.1 Dynamic Response

2.1.1 Operating Tension

Fig. 9 is the tension diagrams of the measured chain links under faults. When the chain in areas PQ is stuck, the maximum tensions in areas Q and R reach 1139.9 kN and 669.9 kN, respectively, and the stuck side is

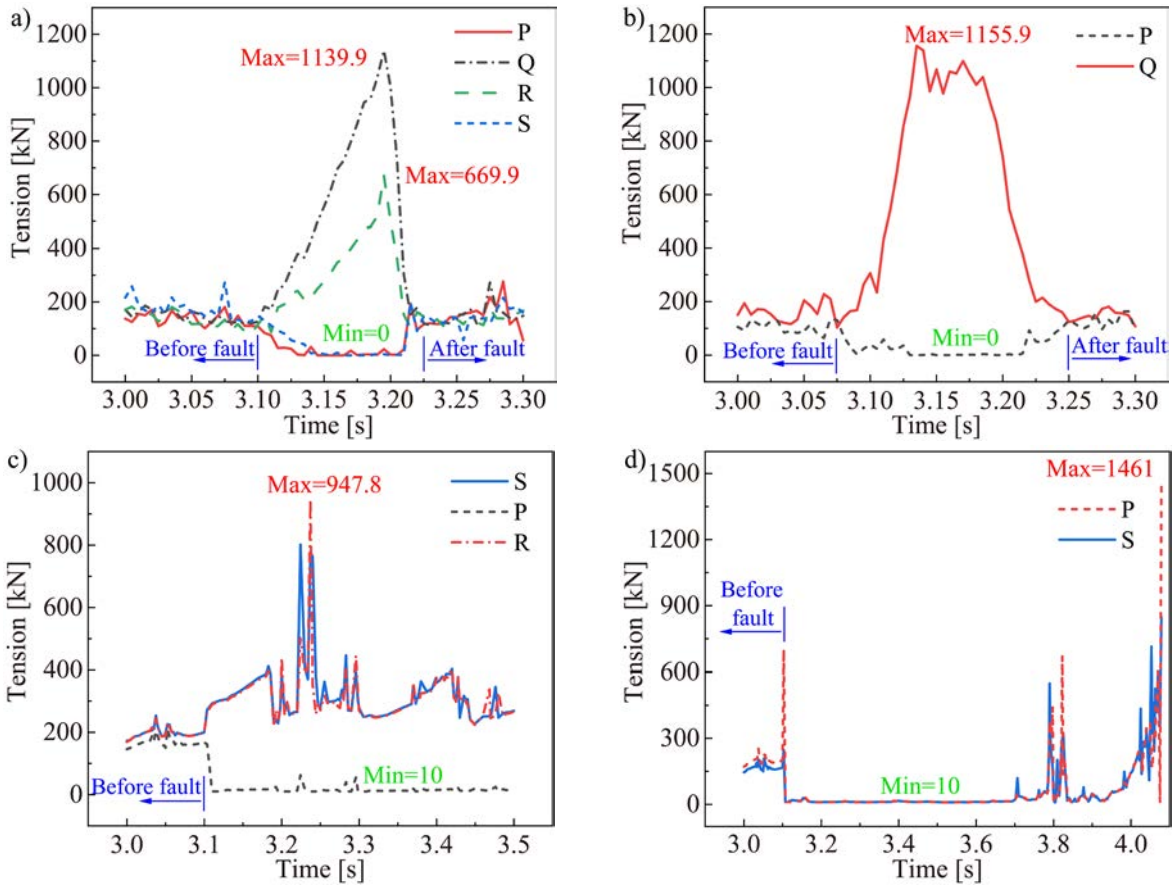

Fig. 9. *The tension curves; a) unilateral jamming; b) bilateral jamming; c) unilateral breaking; d) bilateral breaking*

larger than the deflected side; the tensions in areas P and S are reduced, and the minimums are both 0 kN. Furthermore, the tension on the stuck side changes earlier than the deflection side, but both sides return to stability concurrently. The dynamic responses of two chains are identical when both sides of the scraper are stuck, so only the curves on the side PQ are plotted. It can be seen from Fig. 9b that the maximum is 1155.9 kN, and the growth rate of tension is faster. The reason is that when both sides of the scraper are stuck, the scraper cannot deflect, and the growth rate of chain tension cannot be alleviated by deflection.

According to the tension response under chain stuck fault, the areas Q and R were set as the fracture points. When the area Q fails, the tension in area P decreases and stabilizes at 10 kN to 15 kN due to medium doubled chain; the tension in areas R and S increases due to the augment of load, and the maximum is 947.8 kN. When the chains in areas Q and R fracture, the middle scraper deflects instantly, the front and rear scrapers deflect in the opposite direction, and the chains in areas P and S are loose, as shown in Fig. 10. With the return of the front and rear scrapers and the deflection of the middle scraper, the chains finally break.

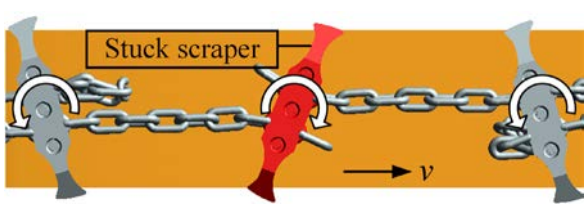

Fig. 10. *The deflection of the nearby scrapers*

2.1.2 Velocity of Chains

Fig. 11 reveals the velocity curves of the measured chain links under faults. In Fig. 11a, compared with the deflected side, the velocity fluctuation of the stuck side is larger, and the two fluctuations in area P are earlier and later than those in area Q severally. In addition, the chain links on the stuck side have the opposite velocity. The reason is that the chains in areas

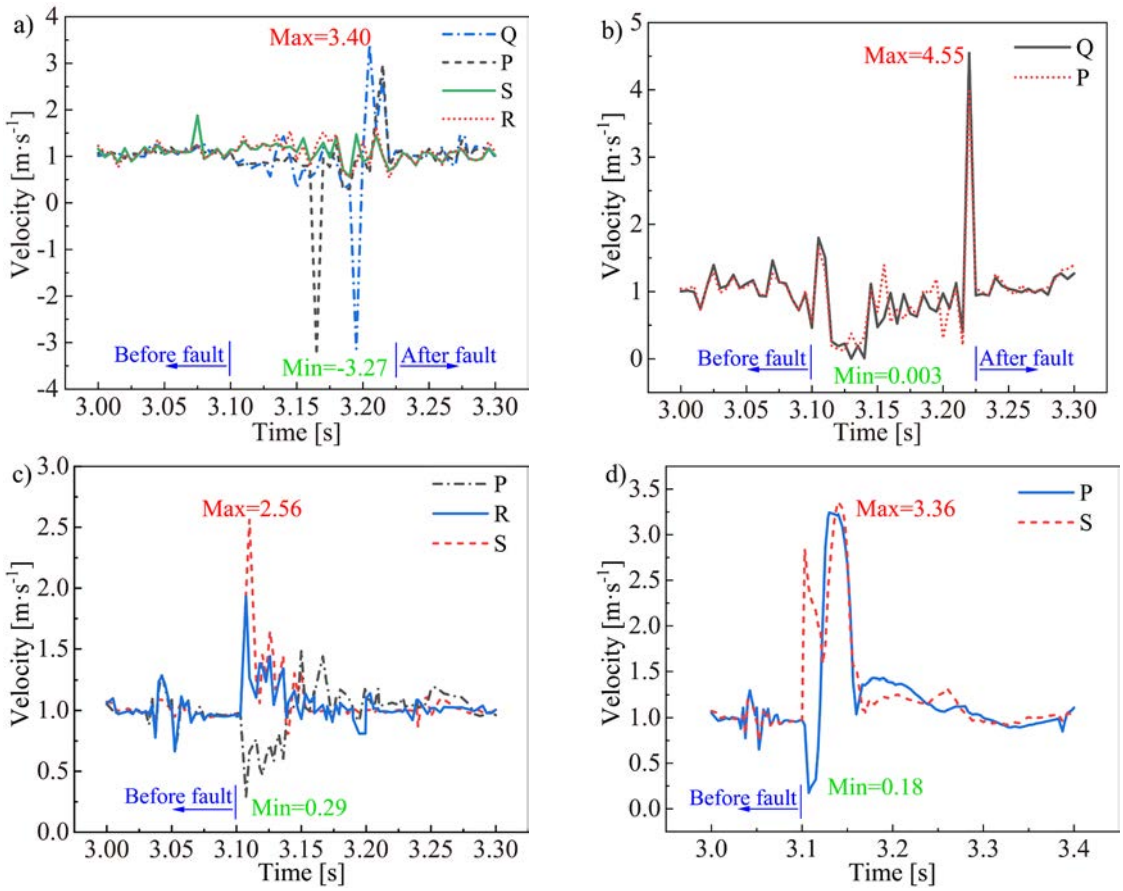

Fig. 11. *The velocity curves; a) unilateral jamming; b) bilateral jamming; c) unilateral breaking; d) bilateral breaking*

P and Q are piled up and tensioned, respectively, and this state is transmitted forward and backward with the stuck scraper as the centre. As a result, the tension at the rear of the tested link along the transportation direction is greater than that at the front in a short time. The velocity at the front and rear of the scraper are synchronous when two sides are stuck. The lowest velocity is almost 0 $m \cdot s^{-1}$, and there is a large positive mutation before recovery.

When the chain in area Q breaks, the velocity in area P is reduced by the deflection and impact of the scraper, and the velocities in areas R and S increase with different amplitudes. When the chains at areas Q and R both break, the velocity in area P fluctuates from decrease to increase, and the velocity in area S increases.

2.1.3 Acceleration in the Z-Direction

Fig. 12 shows the Z-direction acceleration curves of the measured chain links under faults. The scraper vibration can affect the chain vibration under normal conditions, and their vibrations are transmitted through the chain tension. From the chain tension curves under fault conditions (Fig. 9), it can be seen that when the PQ side of the scraper is stuck, the stuck scraper vibrates and deflects due to the external load. The scraper deflection loosens the chains in areas P and S, blocks the transmission of chain tension, causes the chain vibration in this area to weaken, and the minimum can reach 0. Additionally, the scraper deflection causes the chains in areas Q and R to be tightened, and the chain tension and its transmittance increases, resulting in the increase of chain vibration, up to 33 $m \cdot s^{-2}$. Since the chain vibrations in areas R and S are the same as those in areas Q and P, respectively, they are not repeated in the figure. The results of bilateral jamming and unilateral fracture of the chain are the same as above.

When the chains in areas Q and R break, the middle scraper deflects quickly, and then the front and rear scrapers deflect in opposite directions, as shown in Fig. 10. The remaining chains are piled up, the

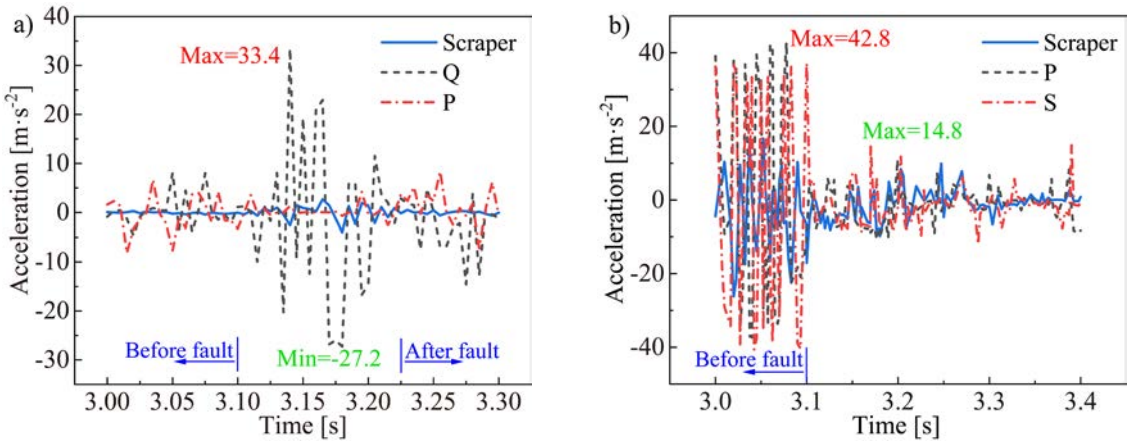

Fig. 12. *The curves of acceleration in the Z-direction; a) unilateral jamming; and b) bilateral breaking*

tension and its transmittance are reduced, resulting in reduced vibration of the chain and scraper.

2.2 Discrete Characteristics of Bulk Coal

2.2.1 Velocity of Bulk Coal

The velocity of bulk coal under unilateral jamming is shown in Fig. 13.

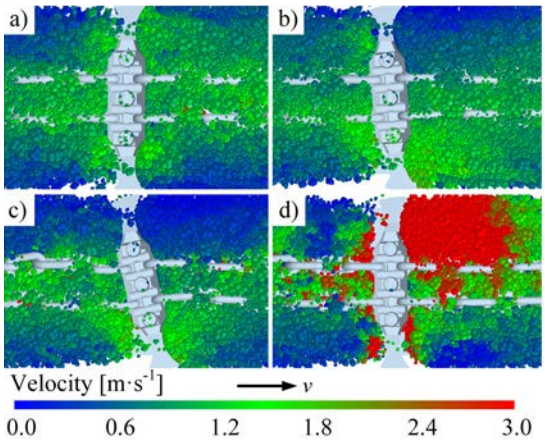

Fig. 13. *The velocity cloud diagram of bulk coal under unilateral jamming; a) before fault; b) initial stage of fault; c) middle stage of fault; d) after fault*

The farther the bulk coal is away from the scraper and chains, the lower the velocity. When the scraper starts to deflect, the velocity of the bulk coal in area Q decreases first; the velocity of the bulk coal in area S increases briefly. During the continuous deflection of the scraper to the maximum, the bulk coal in areas P and Q continue to accumulate, and the bulk coal in area S gradually return to the normal velocity. As the stuck side lags behind the deflected side by an angle, the velocity of the bulk coal in area Q instantly increases when the scraper returns to be steady, which can reach a maximum of 10.15 m·s^{-1}. The flying bulk coal may injure the staff. The result when both sides are stuck is the same as the result on the stuck side in Fig. 13.

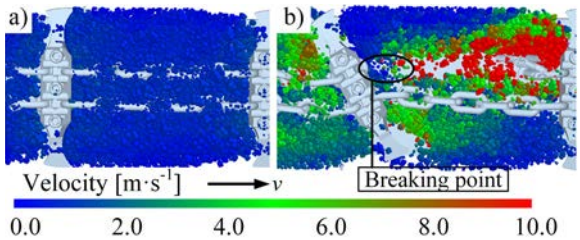

Fig. 14. *The velocity cloud diagram of bulk coal under unilateral breaking; a) before fault; and b) after fault*

2.2.2 Wear of Medium Plate

A layer of coal with a smaller size is often covered between the medium plate and scraper chain. When the scraper chain moves, three-body abrasive wear is formed [13], as shown in Fig. 15. Due to the short simulation time, only the qualitative analysis and prediction of the wear area of the medium plate was carried out; the material of the medium plate is NM450 (C: ≤ 0.35 %). The wear depth in the EDEM software was calculated by Eq. (2).

$$h = Q/A = WF_n d_t / A, \tag{2}$$

where Q [m^3] is the volume of material removed, W [Pa^{-1}] is the wear constant, the size is 1.2×10^{-12} Pa^{-1}, F_n [N] is the normal force, d_t [m] is the tangential distance moved, and A [m^2] is the area of material removed.

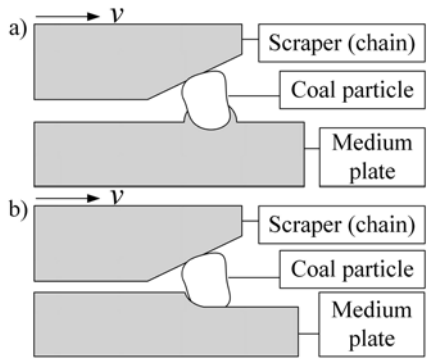

Fig. 15. *The three-body abrasive wear; a) furrow effect; b) micro-cutting effect*

It can be seen from Fig. 16 that the wear area of the medium plate is concentrated near the chain paths, which is consistent with the wear area of the scrapped medium plate. The unilateral jamming condition deepens the wear at the chain paths. In addition to deepening the wear at the chain paths, the bilateral jamming condition also form new wear areas at the centre and both ends of scraper. When the chain fractures, curved wear marks are generated on the medium plate due to the severe deflection of scraper.

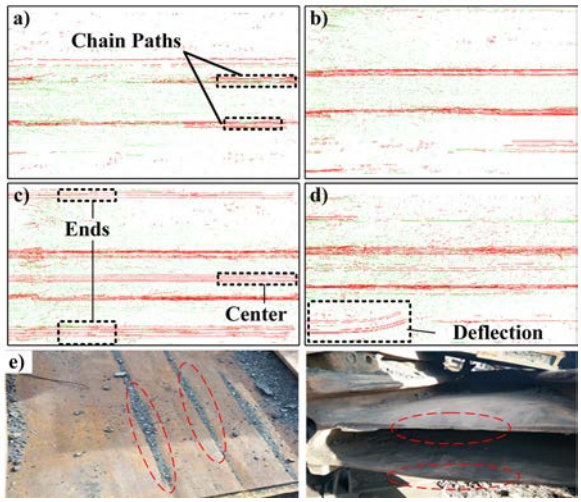

Fig. 16. *The wear areas of medium plate; a) normal; b) unilateral jamming; c) bilateral jamming; d) chain breaking; e) the actual wear area*

2.3 Results of FEA

2.3.1 Static Structural Analysis

The results of static analysis under normal load and stuck fault load were obtained by applying tension of 180 kN and 1155.9 kN to the FEA model, shown in Figs. 17 and 18. The maximum equivalent stress occurs at the inner side of the connection between the curved section and the straight section. The equivalent stress and elastic strain under normal load are less than the yield strength. The maximum equivalent stress under fault load is 1238.2 MPa, which is higher than the yield strength, and the maximum plastic strain is 0.10098. The above results explain that the chain has a high degree of damage when the chain is stuck. To prevent chain breaking accident, the damaged chain should be replaced in time.

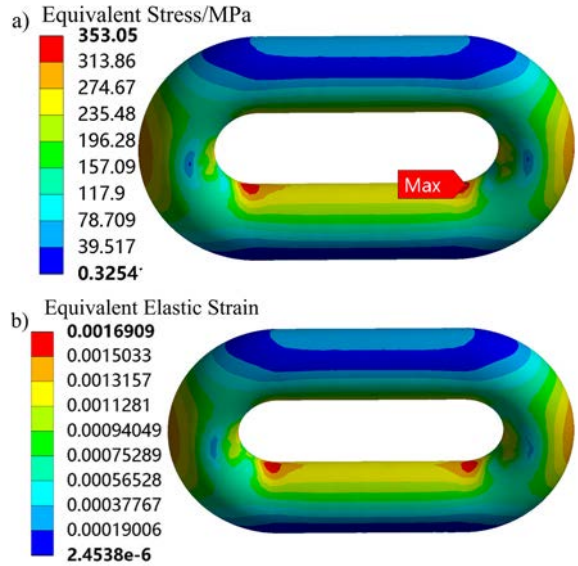

Fig. 17. *The results of statics analysis under normal load; a) equivalent stress, b) equivalent elastic strain*

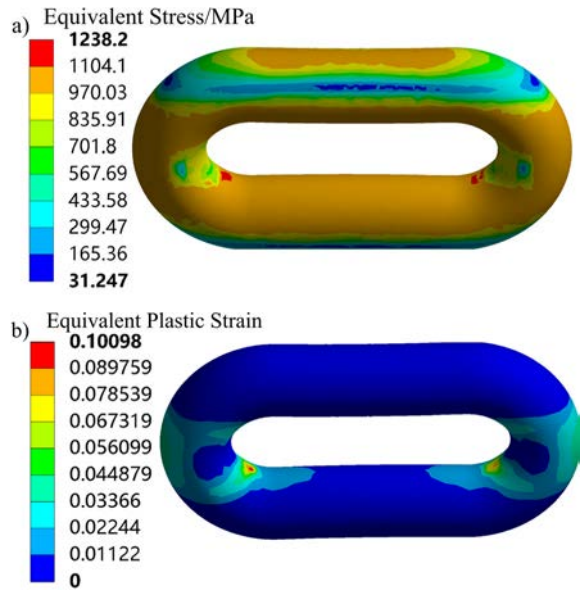

Fig. 18. *The results of static analysis under stuck fault load; a) equivalent stress, b) equivalent elastic strain*

Based on the equipment in Fig. 7, the deformation results of the chain were verified. The comparison of elongation is shown in Table 6. It can be seen that the relative error between simulation and experiment does not exceed 4 %.

Table 6. *The comparison between experimental and simulation values of elongation*

Number	Experimental value [%]			Simulation value [%]	Average relative error [%]
Normal load	0.220	0.225	0.223	0.215	3.43
Fault load	1.27	1.25	1.28	1.22	3.68

2.3.2 Fatigue Life

According to the coupling results, the load history for one cycle under normal conditions was constructed, shown in Fig. 19. The fatigue life was calculated based on the results of static analysis and linear cumulative damage theory. The theory can be expressed as:

$$D = \sum_{1}^{m} (n_i / N_i), \tag{3}$$

where D is the total damage, n_i is the number of cycles under stress level, N_i is the life under stress level, m is the number of stresses.

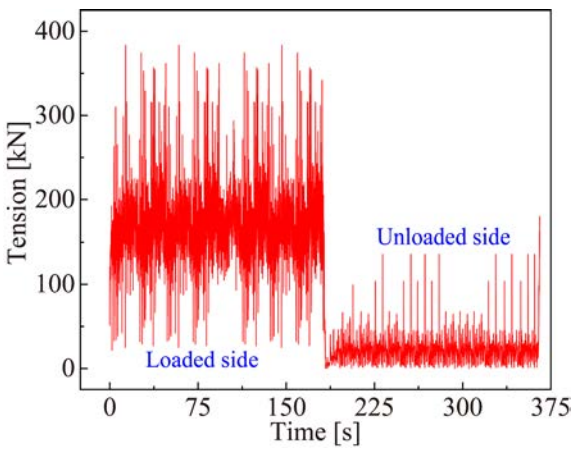

Fig. 19. *The load history under normal condition*

Based on Fig. 19, the stuck fault load was added to obtain the fatigue life. The fatigue life is displayed in Fig. 20. The lowest parts of the life under the two conditions are the contact position and the inner side of the connection, and the lowest values are 20,070 and 383.8 cycles respectively. The life under normal load is 52 times that under fault load. The chain near the stuck position should be overhauled and replaced in time to prevent the chain from breaking.

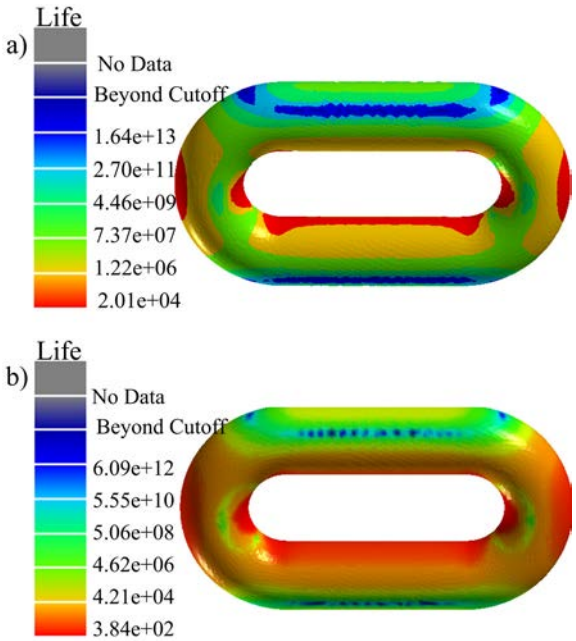

Fig. 20. *The fatigue life; a) normal load, b) fault load*

3 ANALYSIS OF FACTORS AFFECTING CRACK GROWTH

3.1 Plackett-Burman Test

3.1.1 Design of Test

Defects in structure or material are inevitable, of which cracking is the most common. According to load and propagation form of the cracks, they can be divided into three types: open type, slip type, and tear type, as shown in Fig. 21.

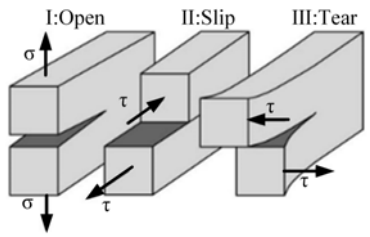

Fig. 21. *The types of the crack*

Stress intensity factor (SIF) K is defined as the strength of the stress field around the crack front of linear elastic material. The main stresses in the chain link are tensile and compressive stresses. The fracture type of chain link is Type-I, which SIF K_1 is expressed as:

$$K_1 = \sigma\sqrt{\pi a} f(a,W), \tag{4}$$

where σ [MPa] is the normal stress, a [mm] is crack size, W [mm] is the size of the component in the direction of crack depth, $f(a, W)$ is the shape correction function.

The Plackett-Burman test determines the significance of the factor by comparing the response variables at different levels of each factor [26]. Based on the results of FEA, a semi-elliptical crack was set on the inner side of the connection. Through pre-simulation, it is found that the positive or negative initial angle of the crack in Fig. 22 does not affect the result. Therefore, the crack depth, depth-length ratio, initial angle and tensile load were taken as factors, and the maximum K_{1max} of the type-I SIF at the crack front was used as the response variable to carry out the screening test. Each factor was set to high and low levels, as listed in Table 7, where the virtual parameters are used for error estimation.

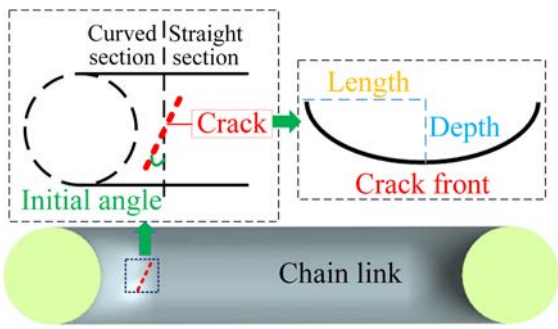

Fig. 22. *The factors of crack*

Table 7. *The factors and levels of Plackett-Burman test*

Parameters	Low (–1)	High (+1)
Crack depth L [mm]	0.2	1
Depth to length ratio B	0.2	0.8
Initial angle A [°]	0	60
Tensile load F [kN]	90	270
Virtual parameters	-1	+1

3.1.2 Results of Testing

Table 8 demonstrates the plan and results of test, and the significance ranking of factors on K_{1max} is listed in Fig. 23. From the pareto chart, the tensile load, initial angle, and crack depth are significant on K_{1max} (t > 2.36462), and the depth to length ratio is not significant. The tensile load and crack depth are positive effects, and the initial angle is negative. The order of significance is $F > A > L$. Therefore, the significant factors were selected for the following tests.

Table 8. *The plan and result of the Plackett-Burman test*

Number	L	B	A	F	K_{1max} [MPa·mm$^{-1/2}$]
1	1	1	–1	1	682.48
2	–1	1	1	–1	31.16
3	1	–1	1	1	299.59
4	–1	1	–1	1	309.75
5	–1	–1	1	–1	43.38
6	–1	–1	–1	1	424.65
7	1	–1	–1	–1	293.58
8	1	1	–1	–1	226.25
9	1	1	1	–1	71.88
10	–1	1	1	1	94.07
11	1	–1	1	1	299.59
12	–1	–1	–1	–1	140.78

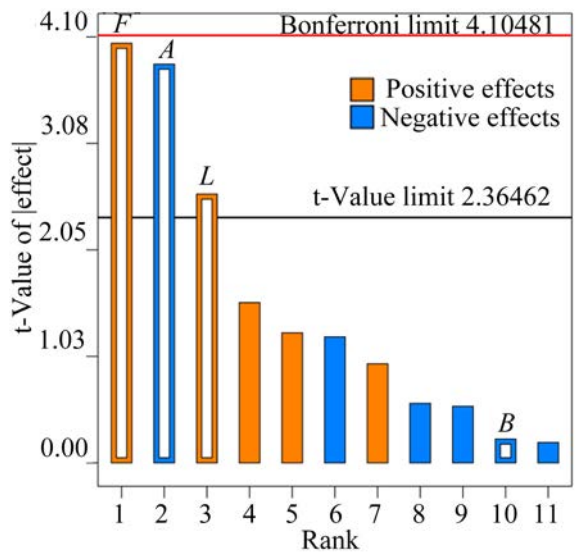

Fig. 23. *The pareto chart*

3.2 Single Factor Test

The design of the single factor test is shown in Table 9, and the depth to length ratio is fixed at 0.5. The K_1 on the crack front is plotted as Fig. 24, where the ratio of the arc length from a point to the end of crack front to the total arc length is the relative position of the point. In Fig. 24, K_1 aggrandizes with the increase of crack depth, and the growth rate gradually slows down. K_1 is negatively correlated with the initial angle; the larger the initial angle, the greater the decrease in K_1, and the smoother the curve of K_1. K_1 is positively correlated with the tensile load, and the increase of K_1 on the crack front is almost constant; the lower the load, the smoother the curve. In addition, as the initial angle increases, the maximum position of K_1 moves to the end of crack front near the load side.

Table 9. *The design of the single factor test*

Number	L [mm]	A [°]	F [kN]
1	0.2 to 1.0	0	180
2	0.6	0 to 60	180
3	0.6	0	90 to 270

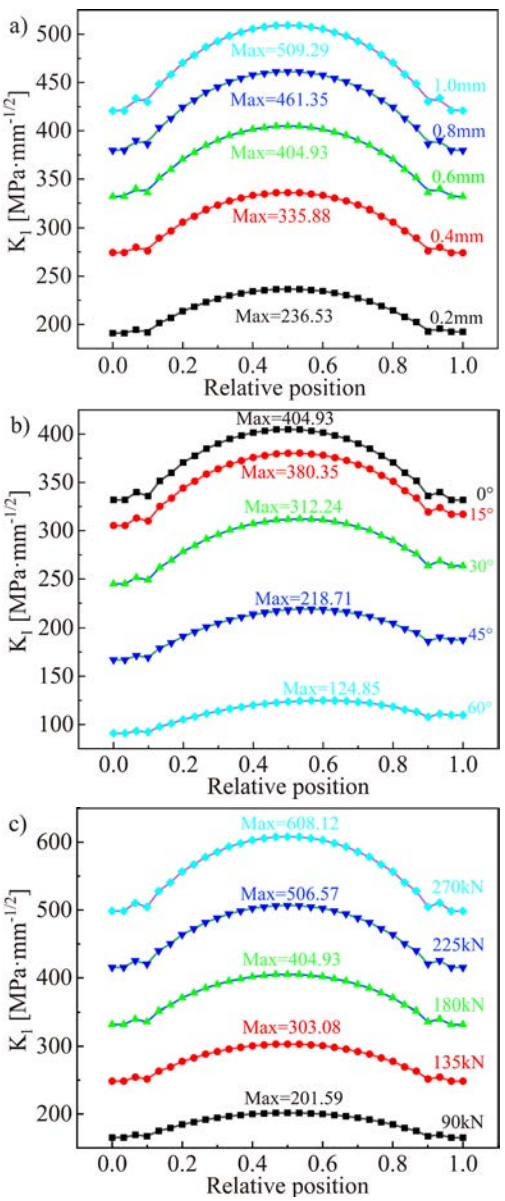

Fig. 24. *The effects on K_1; a) crack depth; b) initial angle; c) tensile load*

3.3 Box-Behnken Test

3.3.1 *Design of Test*

Based on the results of the Plackett-Burman test, the Box-Behnken test was designed with the K_{1max} as the response value. Each factor was set to high (+1), medium (0), and low (-1) three levels, as listed in Table 10. The entire design includes 12 sets of factorial tests and three sets of central tests for error estimation.

Table 10. *The factors and levels of Box-Behnken test*

Factors	–1	0	+1
L [mm]	0.2	0.6	1
A [°]	0	30	60
F [kN]	90	180	270

3.3.2 Results of Test

Based on the results of the test in Table 11, the quadratic regression polynomial between factors and K_{1max} was constructed by Design-Expert software as:

$$K_{1max} = -124.6 + 245.42L + 5.49A + 1.5F - 3.82LA + 1.46LF - 0.026AF - 126.34L^2 - 0.05A^2 - 0.00017F^2. \quad (5)$$

Table 11. *The results of the Box-Behnken test*

Number	L	A	F	K_{1max} [MPa·mm$^{-1/2}$]
1	-1	-1	0	239.98
2	1	-1	0	509.29
3	-1	1	0	72.71
4	1	1	0	158.86
5	-1	0	-1	92.02
6	1	0	-1	196.12
7	-1	0	1	277.36
8	1	0	1	591.39
9	0	-1	-1	201.01
10	0	1	-1	62.137
11	0	-1	1	605.63
12	0	1	1	187.59
13	0	0	0	310.23
14	0	0	0	305.57
15	0	0	0	316.51

The variance analysis of the regression polynomial is listed in Table 12. The model is extremely prominent ($P < 0.0001$), and the lack of fit is not prominent ($P = 0.0839 > 0.05$). The coefficient of variation (CV) is small (5.3 %), the R Square before (0.998) and after (0.993) correction is close to 1, and the accuracy is high (46 > 4). It can be concluded that the constructed quadratic model has high fitting accuracy and can characterize the relationship between K_{1max} and factors. The significance of term

was acquired by F-test. The larger the F value, the more prominent the impact. When the significance level is 0.05, the significances of terms are ranked as: $F > A > L > AF > LF > LA > A^2 > L^2$.

Table 12. *The variance analysis of polynomial*

Source	Sum of Squares	*F*-value	*P*-value
Model	4.21E+05	220.05	< 0.0001
L	74805.19	351.97	< 0.0001
A	1.44E+05	679.18	< 0.0001
F	1.54E+05	725.54	< 0.0001
LA	8386.9	39.46	0.0015
LF	11017.65	51.84	0.0008
AF	19483.55	91.67	0.0002
L^2	1508.79	7.1	0.0446
A^2	7592.13	35.72	0.0019
F^2	6.56	0.0309	0.8674
Lack of Fit	1002.4	11.09	0.0839
$R^2 = 0.998$; $R_a^2 = 0.993$; $CV = 5.3\ \%$; Precision = 46			

3.3.3 The Effect of Interaction

Through the three-dimensional response surface graph, the relationship between the interaction and the response value can be understood intuitively. When a factor is at 0 level, the variation of K_{1max} with the interaction is shown in Fig. 25. It can be seen that the crack depth and tensile load are positively related to the rate of change of K_{1max} with other factors, while the initial angle has a negative effect on the rate of change of K_{1max} with other factors.

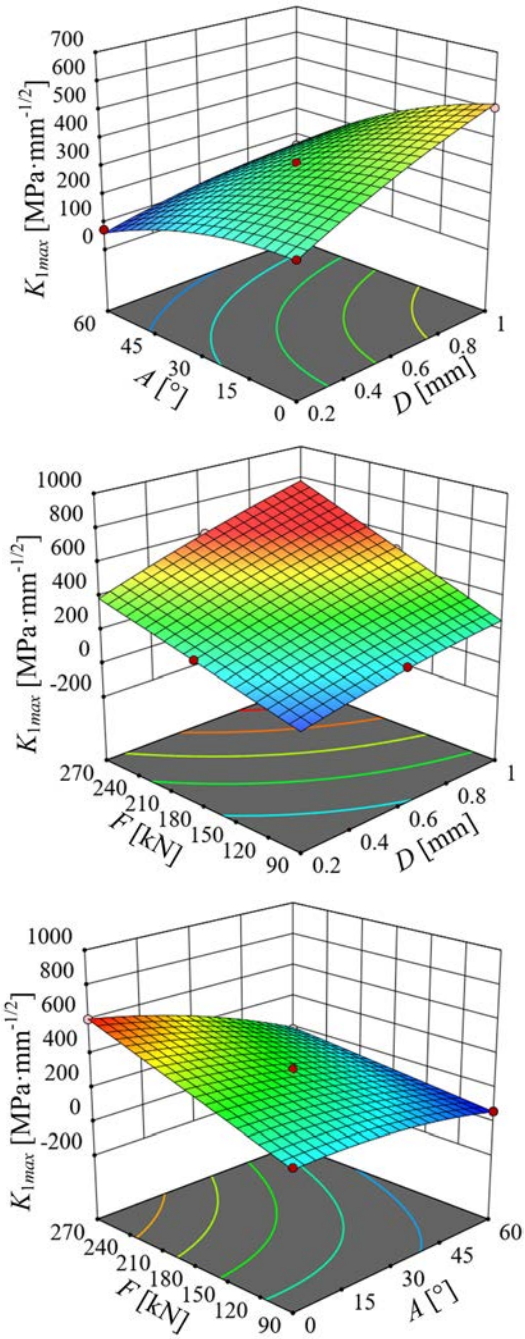

Fig. 25. *Response surface of interaction to* K_{1max}*; a) DA; b) DF; c) AF*

4 CONCLUSIONS

In this paper, a fault simulation method of scraper conveyor based on MBD-DEM-FEM coupling was used. The DEM-MBD-FEM models were established and verified by experiments and theory, the response data of the chain and bulk coal under chain stuck and chain-breaking faults were obtained, and some results were verified. For the fracture failure, the single factor test and response surface test were used to investigate the single and interactive effects of factors on the SIF.

1. With the force and stacking angle as response values, a rotary transport testing machine was designed to modify the contact parameters of coal. The DEM-MBD coupling model was verified, and the relative error between tension difference and resistance is less than 8 %. The static structure model of the chain was verified by the chain tensile experiment, and the relative error is less than 5 %.
2. In chain jamming and breaking faults, the deflection of scraper causes the uneven stress on chains. The tension of the tensioned chain increases rapidly, resulting in the torsion and vibration of chains. The tension, velocity, and

vibration of the loose chain decrease. The fault load leads to the plastic deformation of chain link and reduces its fatigue life. The wear of the medium plate is concentrated on the chain paths, which is consistent with the actual situation. In addition, the chain faults cause new wear on the centre and both sides of the medium plate surface.

3. The tensile load, initial angle and crack depth are significant on K_1. Through response surface analysis, both the crack depth and tensile load are positively correlated with K_1, and the initial angle is negatively correlated with K_1. The initial angle has a negative effect on the change rate of K_{1max} with other factors, while the crack depth and tensile load positively affect it.

5 ACKNOWLEDGEMENTS

This project was supported by National Natural Science Foundation of China (Grant Nos. 51875386 and 51804207) and the Fund for Shanxi "1331" Project.

6 REFERENCES

[1] Zhang, X., Li, W., Zhu, Z., Yang, S., Jiang, F. (2019). Fault detection for the scraper chain based on vibration analysis using the adaptive optimal kernel time-frequency representation. *Shock and Vibration*, vol. 2019, art. ID 6986240, **DOI:10.1155/2019/6986240**.

[2] Thirumurugan, R., Gnanasekar, N. (2020). Influence of finite element model, load-sharing and load distribution on crack propagation path in spur gear drive. *Engineering Failure Analysis*, vol. 110, art. ID 104383, **DOI:10.1016/j.engfailanal.2020.104383**.

[3] Li, J., Ma, Q. (2018). Mechanical characteristics of the scraper chain transmission system under the condition of chain blocked. *Journal of the China Coal Society*, vol. 43, p. 591-599, **DOI:10.13225/j.cnki.jccs.2018.0384**. (in Chinese)

[4] Jiang, S.B., Zeng, Q.L., Wang, G., Gao, K.D., Wang, Q.Y., Hidenori, K. (2018). Contact analysis of chain drive in scraper conveyor based on dynamic meshing properties. *International Journal of Simulation Modelling*, vol. 17, no. 1, p. 81-91, **DOI:10.2507/ijsimm17(1)418**.

[5] Wang, D.G., Zhang, J., Zhu, Z.C., Gang, S., Xiang, L. (2019). Crack initiation characteristics of ring chain of heavy-duty scraper conveyor under time-varying loads. *Advances in Mechanical Engineering*, vol. 11, no. 9, p. 11, **DOI:10.1177/1687814019880366**.

[6] Wang, X.W., Li, B., Wang, S.W., Yang, Z.J., Cai, L. (2018). The transporting efficiency and mechanical behavior analysis of scraper conveyor. *Proceedings of the Institution of Mechanical Engineers Part C-Journal of Mechanical Engineering Science*, vol. 232, no. 18, p. 3315-3324, **DOI:10.1177/0954406217734002**.

[7] Jiang, S.B., Ren, W.J., Mao, Q.H., Zeng, Q.L., Yu, P.F., Gao, K.D., Wang, L. (2021). Dynamic analysis of the scraper conveyor under abnormal operating conditions based on the vibration and speed characteristics. *Shock and Vibration*, vol. 2021, art. ID 8887744, **DOI:10.1155/2021/8887744**.

[8] Xie, C., Liu, Z., Mao, J., Xie, M., Lu, J. (2018). Analysis of torsional vibration characteristics of scraper conveyor on chain blocked condition. *Journal of the China Coal Society*, vol. 43, no. 8, p. 2348-2354, **DOI:10.13225/j.cnki.jccs.2017.1722**. (in Chinese)

[9] Wang, X.W., Wang, S.P., Long, R.S., Yang, Z.J., Liu, G.P. (2016). Rigid-flexible coupled dynamic contact analysis for a chains drive system of a heavy scraper conveyer during loading start-up. *Journal of Vibration and Shock*, vol. 35, no. 11, p. 34-40, **DOI:10.13465/j.cnki.jvs.2016.11.006**. (in Chinese)

[10] Jiang, S.B., Zhang, X., Gao, K.D., Gao, J., Wang, Q.Y., Hidenori, K. (2017). Multi-body dynamics and vibration analysis of chain assembly in armoured face conveyor. *International Journal of Simulation Modelling*, vol. 16, no. 3, p. 458-470, **DOI:10.2507/ijsimm16(3)8.391**.

[11] Dong, Y.S., Si, F.Q., Cao, Y., Jin, W., Ren, S.J. (2021). A new mechanistic model for abrasive erosion using discrete element method. *Powder Technology*, vol. 380, p. 486-496, **DOI:10.1016/j.powtec.2020.11.017**.

[12] Wang, X.W., Li, B., Yang, Z.J. (2018). Analysis of the bulk coal transport state of a scraper conveyor using the discrete element method. *Strojniški vestnik - Journal of Mechanical Engineering*, vol. 64, no. 1, p. 37-46, **DOI:10.5545/sv-jme.2017.4790**.

[13] Xia, R., Wang, X., Li, B., Wei, X., Yang, Z. (2019). Discrete element method-(DEM-) based study on the wear mechanism and wear regularity in scraper conveyor chutes. *Mathematical Problems in Engineering*, vol. 2019, art. ID 4191570, **DOI:10.1155/2019/4191570**.

[14] Xia, R., Wang, X., Li, B., Wei, X., Yang, Z. (2019). The prediction of wear on a scraper conveyor chute affected by different factors based on the discrete element method. *Proceedings of the Institution of Mechanical Engineers, Part C: Journal of Mechanical Engineering Science*, vol. 233, no. 17, p. 6229-6239, **DOI:10.1177/0954406219861130**.

[15] Xia, R., Li, B., Wang, X.W., Li, T.J., Yang, Z.J. (2019). Measurement and calibration of the discrete element parameters of wet bulk coal. *Measurement*, vol. 142, p. 84-95, **DOI:10.1016/j.measurement.2019.04.069**.

[16] Li, T.J., Wang, X.W., Li, B., Li, J.L., Yang, Z.J. (2018). Optimization method for coal particle model parameters based on discrete element method. *China Powder Science and Technology*, vol. 24, no. 05, p. 6-12, **DOI:10.13732/j.issn.1008-5548.2018.05.002**. (in Chinese)

[17] Zhang, P.L., Li, B., Wang, X.W., Liu, C.Y., Bi, W.J., Ma, H.Z. (2020). The loading characteristics of bulk coal in the middle trough and its influence on rigid body parts. *Strojniški vestnik - Journal of Mechanical Engineering*, vol. 66, no. 2, p. 114-126, **DOI:10.5545/sv-jme.2019.6267**.

[18] Li, S., Zhu, Z.C., Lu, H., Shen, G. (2019). A system reliability-based design optimization for the scraper chain of scraper conveyors with dependent failure modes. *Eksploatacja I*

Niezawodnosc-Maintenance and Reliability, vol. 21, no. 3, p. 392-402, **DOI: 10.17531/ein.2019.3.5**.

[19] Xue, H., Gu, S.P., Gong, X.Y., Ishihara, Z.Y., Tong, K.H. (2012). Analysis on structural integrity of defective mine round-link chains. *Mining & Processing Equipment*, vol. 40, no. 12, p. 98-101, **DOI: 10.16816/j.cnki.ksjx.2012.12.028**. (in Chinese)

[20] Zhao, L., Jin, X., Liu, X. (2020). Numerical research on wear characteristics of drum based on discrete element method (DEM). *Engineering Failure Analysis*, vol. 109, art. ID 104269, **DOI:10.1016/j.engfailanal.2019.104269**.

[21] Zhou, C., Yue, H., Li, Y., Zhang, M., Liu, J., Aijaz, S. (2019). A sphere filling algorithm for irregular aggregate particle generation based on non-linear optimization method. *KSCE Journal of Civil Engineering*, vol. 23, p. 120-129, **DOI:10.1007/s12205-018-0182-8**.

[22] Richesson, S., Sahimi, M. (2019). Hertz-Mindlin theory of contacting grains and the effective-medium approximation for the permeability of deforming porous media. *Geophysical Research Letters*, vol. 46, no. 14, p. 8039-8045, **DOI:10.1029/2019gl083727**.

[23] Hong, X.H. (2005). *Mine Transportation and Lifting*. China University of Mining and Technology Press, Xuzhou. (in Chinese)

[24] Liu, X., Wei, L. (2017). Vibration research on the polygonal effect of scraper conveyor. *International Conference on Computer Technology, Electronics and Communication*, p. 866-870, **DOI:10.1109/ICCTEC.2017.00192**.

[25] Bai, J., Xie, M.J. (2016). Scraper conveyor fault statistics and analysis of Shendong mining. *Coal Mine Machinery*, vol. 37, no. 11, p. 141-143, **DOI:10.13436/j.mkjx.201611050**. (in Chinese)

[26] Xia, R., Li, B., Wang, X.W., Yang, Z.J., Liu, L.P. (2019). Screening the main factors affecting the wear of the scraper conveyor chute using the Plackett-Burman method. *Mathematical Problems in Engineering*, vol. 2019, art. ID 1204091, **DOI:10.1155/2019/1204091**.

Strojniški vestnik - Journal of Mechanical Engineering 67(2021)10, 516-524

DOI:10.5545/sv-jme.2021.7251
Original Scientific Paper
Received for review: 2021-05-07
Received revised form: 2021-08-30
Accepted for publication: 2021-09-07

Investigation on the Depth of Slip Hanger Teeth Bite into Casing and the Mechanical Properties of Casing under Different Suspension Loads in Ultra-Deep Wells

Yong Chen – Jinjin Tan – Guoping Xiao
Southwest Petroleum University, School of Mechanical and Electrical Engineering, China

There is great difficulty in controlling the setting load of the large-size slip casing hanger in the Northwest Oilfield in China, and a reasonable setting load is of great significance. This paper studied the relationship between slip hanger bite depth and suspension load in the Φ 273 mm WE-type slip hanger in the Northwest Oilfield in China through experiment, theoretical computation, and finite element analysis. The accuracy of the finite element model was proved by comparing the finite element simulation results with the experimental bite marks on the casing surface. The study results show that the bite mark of the slip insert in the casing is deeper in the lower part of the sitting position. When the hanging load increases from 1000 kN to 6000 kN, the maximum bite depth of the slips in the casing gradually increases with the suspension load. The residual collapse strength of the casing decreases correspondingly. When the residual collapse strength decreases to a certain value, the maximum suspension force corresponding to the bite depth of the slip insert can be obtained. Based on the finite element research results and theoretical equations, the stress distribution on the casing wall where the slips bite the deepest is obtained by derivation. The suggestions on improving the material structure of the casing under this stress were proposed. The limit of the setting load of the large-size casing wellhead for avoiding casing collapse was obtained, which is of great significance for guiding field-casing setting.
Keywords: WE-type slip hanger, suspension load, slip hanger bite depth, finite element simulation, casing

Highlights
- *The relationship between slip hanger bite depth and suspension load has been studied.*
- *The bite depth of the slips is gradually reduced from no. 1 to no. 17 (from bottom to top) under a specific suspension load.*
- *The maximum circumferential squeezing stress on the inner wall of the casing is the risky section, which is subjected to the deepest bite by slip inserts.*
- *As the suspension load increases, the casing residual collapse strength decreases.*
- *Comparing the experimental result with the finite element result, shows that the two are consistent.*

0 INTRODUCTION

There is increasing difficulty in controlling the setting load due to increasing large-size casing tripped into deep reservoirs in the Northwest Oilfield in China. Excessive setting loads and the high-pressure and high-temperature (HPHT) conditions of reservoirs (such as 70 MPa and 170 °C) will cause problems such as wellhead subsidence, and severe damage to the casing caused by slips and the sitting load is too small possibly lead to poor sealing of the casing head [1] and [2]. Tripping the liner hanger into the upper casing is completed through interaction between the liner hanger slips and the casing. The setting of the liner hanger causes variation in the initial stress distribution inside the casing. The additional circumferential stress and additional axial stress caused by slips increase the load on the casing and affect the safety performance of the casing; those beyond the original design loads significantly lessen the margin against piping failure [3]. Statistics found that there were 10 well-times of large-size deep well casings in the past two years, and 3 well-times had abnormalities during wellhead installation. Therefore, a choice of setting load to solve the above contradictions and recommended practices for the setting of large casings are of great significance.

Many efforts have been put in analysis of the force and structure of the slip hanger and casing. Li et al. [4] and Tong et al. [5] carried out the mechanical analysis of slips on the packer with statics principles and obtained the formula for calculating the normal stress on the slip insert during anchoring of the slips and. Tang et al. [6] aim at the problem of damage caused by the casing pressure on the slip after setting, the pressure-bearing law of the slip teeth under the three-tooth parameters was analysed. Mohammed et al. [7] focused on factors attributing to casing failure, their failure mechanism and the resulting failure mode. The slip-casing bite model was analysed using the finite element numerical simulation method, which has been widely used in recent years. Wang et al. [8] carried out the finite element analysis of the force process of slips and improved the structural parameters of slips.

However, when the well's casing head pressure cannot be permanently bled off with a needle valve,

*Corr. Author's Address: School of Mechatronic Engineering, Southwest Petroleum University, China. chyswpu@163.com

the casing is said to exhibit sustained casing pressure (SCP) [9]. A cement sheath can act as a secondary barrier element in a dual barrier (elastomer seal and cement sheath) zonal isolation system. Cement is the main physical barrier able to seal fluid flow into unintended zones from the wellbore [10] and [11]; the rubber materials can be squeezed into the annulus between the hanger and the upper casing, effectively sealing the annulus, and providing an efficient two-way pressure-bearing capacity [12] to [14].

In this study, the relationship between slip insert bite depth and suspension load of the WE-type slip hanger of the Northwest Oilfield in China was studied using finite element analysis methods and theoretical computation. The limit of the setting load of the large casing wellhead for avoiding casing collapse was obtained. The formula for calculating the internal stress distribution of the risky section of the casing was derived to guide the design of the well structure and field operation.

1 THEORETICAL ANALYTIC METHODS

Current well-drilling and operation technologies cannot provide cost-effective solutions for emerging challenges. Based on statistics, casing deformation was observed in 38 wells out of 72 horizontal wells after hydraulic fracturing [15] and [16]. According to the field survey, there is always a section with the largest bite depth when the slip hanger holds the casing, i.e., the risky section. Lowering the pH value will cause an electrochemical reaction. It is common for the casing material to be exposed to the H_2S/CO_2 acid gas environment, and electrochemical reactions are prone to occur in risky sections [17] to [19].

In order to roughly clarify how the casing will be destroyed after exceeding the limit suspension load, the distribution of circumferential normal stress, radial normal stress, circumferential and radial shear stress of the dangerous section of the casing is determined by the theory of elastoplastic mechanics [20].

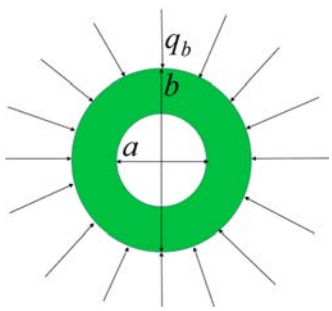

Fig. 1. *Diagram of stress on risky section of casing*

As shown in Fig. 1, the risky section of the casing is simplified as a circular ring. The outer wall of the ring is bitten by the slip inserts to produces a squeezing force. If the casing body force is neglected, the force is axisymmetric, and the stress component is written as [20]:

$$\sigma_\rho = \frac{A}{\rho^2} + B\left(1 + 2\ln\rho\right) + 2C, \tag{1}$$

$$\sigma_\varphi = -\frac{A}{\rho^2} + B\left(3 + 2ln\rho\right) + 2C, \tag{2}$$

$$\tau_{\rho\varphi} = \tau_{\varphi\rho} = 0. \tag{3}$$

Boundary conditions:

$$\left(\tau_{\rho\varphi}\right)_{\rho=a} = 0, \tag{4}$$

$$\left(\tau_{\rho\varphi}\right)_{\rho=b} = 0, \tag{5}$$

$$\left(\sigma_\rho\right)_{\rho=a} = 0, \tag{6}$$

$$\left(\sigma_\rho\right)_{\rho=b} = -q_b. \tag{7}$$

According to Eq. (3), Eqs. (4) and (5) are satisfied. Eqs. (6) and (7) are expressed as:

$$\frac{A}{a^2} + B\left(1 + 2lna\right) + 2C = 0, \tag{8}$$

$$\frac{A}{b^2} + B\left(1 + 2lnb\right) + 2C = -q_b. \tag{9}$$

A compatible equation is expressed as:

$$\left(\frac{\partial^2}{\partial\rho^2} + \frac{1}{\rho}\frac{\partial}{\partial\rho} + \frac{1}{\rho^2}\frac{\partial^2}{\partial\varphi^2}\right)^2 \Phi = 0, \tag{10}$$

which satisfies the compatibility equation.

The balanced differential equation (casing body-weight neglected) is expressed as:

$$\frac{1}{\rho}\frac{\partial\sigma_\varphi}{\partial\varphi} + \frac{\partial\tau_{\rho\varphi}}{\partial\rho} + \frac{2\tau_{\rho\varphi}}{\rho} = 0, \tag{11}$$

$$\frac{\partial\sigma_\rho}{\partial\rho} + \frac{1}{\rho}\frac{\partial\tau_{\rho\varphi}}{\partial\rho} + \frac{\sigma_\rho - \sigma_\varphi}{\rho} = 0, \tag{12}$$

which satisfies the balanced differential equation.

According to the displacement single value condition, $B=0$, then:

$$A = \frac{a^2b^2q_b}{b^2 - a^2}, \quad 2C = \frac{-q_b b^2}{b^2 - a^2}, \tag{13}$$

which are incorporated into Eqs. (1) and (2) and re-arranged to obtain the Lame solution of casing stress:

$$\sigma_\rho = -\frac{1-\frac{a^2}{\rho^2}}{1-\frac{a^2}{b^2}} q_b, \quad (14)$$

$$\sigma_\varphi = -\frac{1+\frac{a^2}{\rho^2}}{1-\frac{a^2}{b^2}} q_b, \quad (15)$$

where ρ is casing radial length interval, $\rho \in [a, b]$, σ_ρ casing radial normal stress, σ_φ circumferential normal stress on casing, $\tau_{\rho\varphi}$, $\tau_{\varphi\rho}$ circumferential and radial shear stress, *A, B, C* arbitrary constants, *a, b* casing inner and outer diameters, q_b external stress of slips on the casing, and Φ stress function.

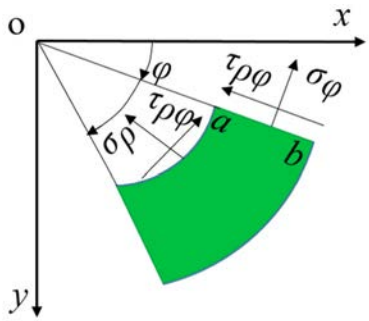

Fig. 2. *Distribution of stresses in the polar coordinates*

The above quantities are described in the form of polar coordinates (Fig. 2); the specific direction and size are determined according to the calculated results.

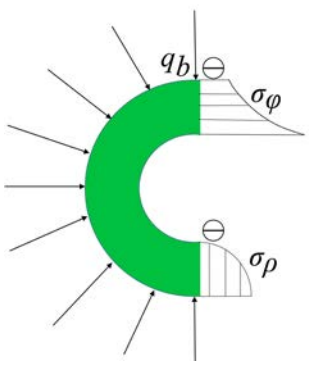

Fig. 3. *Distribution of stress inside the casing radial risky section*

According to derivation, *a, b* and q_b in expression σ_ρ are all constants, and σ_ρ is only positively correlated to a^2/ρ^2. Similarly, σ_φ is only positively correlated to $-a^2/\rho^2$. According to theoretical derivation, the distribution of the radial normal stress and circumferential normal stress on the casing is obtained (Fig. 3).

2 EXPERIMENTAL APPROACH AND PROCEDURE

2.1 Experimental Apparatus

The experiment was carried out on a horizontal hydraulic experiment box, model XDL-10000 kN, and its main technical indicators are shown in Table 1.

Table 1. *Technical indexes of XDL-10000 kN horizontal hydraulic experimental chamber*

Item	Parameter
Maximum test force	10000 kN
Hydraulic cylinder piston stroke	1000 mm
Stretching chuck distance up and down	6 m
Test machine space	500 mm × 6000 mm
Machine host size (L × W × H)	9000 mm × 1200 mm× 800 mm
Hydraulic system power	5 kW
The total weight of the machine	9000 kg

Fig. 4. *Hydraulic experimental chamber*

Fig. 4 shows the test machine used for casing tensile testing. The body adopts a double-frame force frame structure; a single-hydraulic cylinder is installed on the upper beam, the piston and sensor through the force frame and the upper tensile fixtures are directly connected on the specimen tensile test,

so that the loading head structure is simplified; The reaction frame and the left and right rigid frame are connected to the main body of the testing machine; The down-stretching chuck body is connected with the cross beam on the other side of the frame. The side of the host machine is equipped with a hydraulic loading system, which adopts a low-noise hydraulic pump unit, a hydraulic valve group, and a high-precision electro-hydraulic control valve to ensure high precision, high efficiency, low noise and fast response of the system, and to realize the automatic control of loading and reversing of the test (Fig. 5).

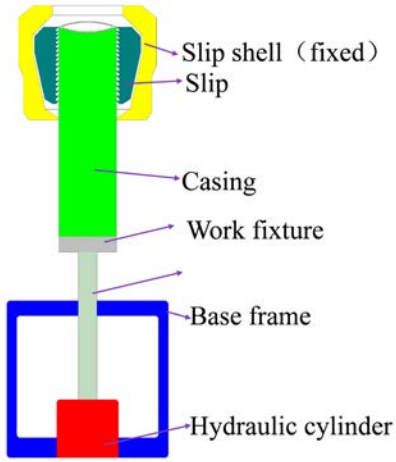

Fig. 5. *The experiment schematic diagram*

2.2 Experimental Procedure

In the experiment, the load increased by 500 kN uniformly over time, and the axial stress on the slips simultaneously measured was plotted as shown in Fig. 6.

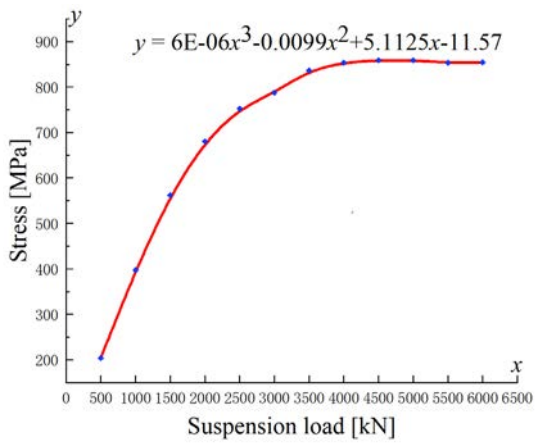

Fig. 6. *Relationship between different experimental loads and maximum normal stress*

As show in Fig. 6 that as the load increases, the maximum normal stress on the casing also increases, and the function fitted according to the curve is a third-order equation. It can be seen that the influence of the load on the results of the research is nonlinear.

3 FINITE ELEMENT ANALYSIS AND MATERIAL PREPARATION

3.1 Structure of ϕ 273 mm WE-Type Slip Hanger

In this paper, the ϕ 273 mm WE slip hanger commonly applied in the Northwest Oilfield in China was studied. The 3D solid structure established according to the real size is illustrated in Fig. 7.

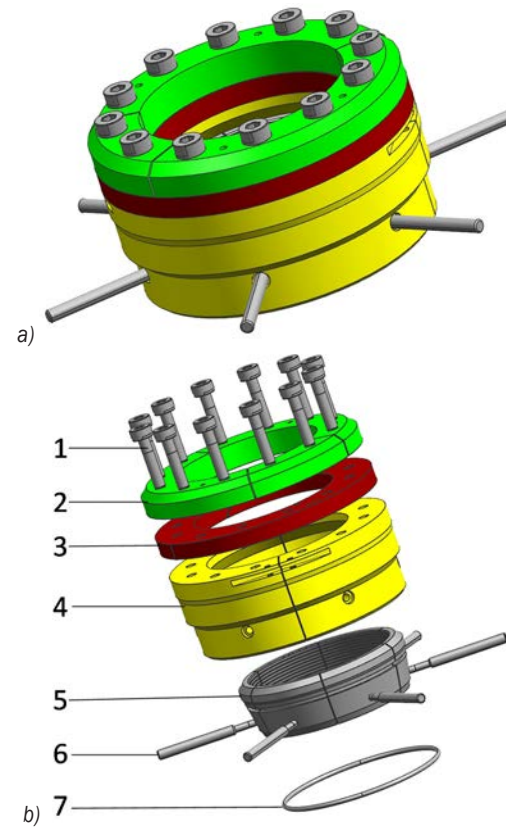

Fig. 7. *a) WE-type-slip hanger assembly diagram; b) WE-type slip hanger exploded view*

According to Fig. 7, the slip hanger consists of 1 hexagon socket screw; 2 pressure plate; 3 sealing ring; 4 slip shell; 5 slip teeth; 6 screw; 7 positioning block

3.2 Working Principle and Analysis of Stress on WE-Type Slip Hanger

The stress on the casing head slips is illustrated in Fig. 8.

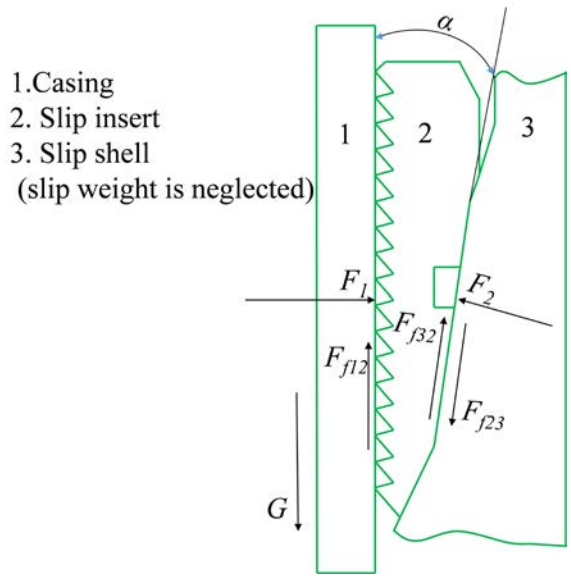

Fig. 8. *Stress on slips*

The process of slip bite in the casing is one of interaction between the slips and the pipe string. When Slip 2 starts to bite into Casing 1, the active force comes from the initial friction force received by the slips. The slips will hold the pipe string radially by causing reactions to the slips through amplifying them with the casing weight. In this process, the casing causes a large vertical gravitational acceleration under the action of the huge suspension load, and this causes the mutual friction between the casing and the slip insert tip, which propels the slip to move downward along Shell 3 until the slips cannot slide. Then, the slips are in direct contact with the slip shell through the inclined plane, and the casing moves downward to squeeze the slips, which remain in the same position by the support of the slip shell. The slip teeth are squeezed into the casing to generate a squeezing force; thus, sufficient friction is created to reach a mechanical equilibrium on the casing. If the suspension weight of the downhole casing increases, the slips continue to bite into the casing due to greater squeezing force until a new balance is reached, and the safe suspension of the casing is realized.

According to Fig. 8, the slips are subjected to the squeezing force and the frictional force of the casing and the slip shell; enough friction is generated by the bite of the slip teeth into the casing to balance the casing gravity. Therefore, for slips, we obtain according to the principle of static balance:

$$F_1 + F_{f32}\sin\alpha = F_2\cos\alpha, \tag{16}$$

$$F_2\sin\alpha + F_{f32}\cos\alpha = G, \tag{17}$$

where F_1 is the supporting force of the casing on the slips [N], F_2 the supporting force of the slip shell on the slips [N], F_{f32} the frictional force of slip shell on the slips [N], F_{f12} the friction force of the casing against the slips [N], F_{f23} the friction force of the slips against the slip shell [N], α the slip cone angle [°], and G the casing weight [N].

3.3 Establishment of Finite Element Model of WE-Type Slip Hanger

The parameters of material properties input in the process of finite element modelling are listed in Table 2.

The model's geometric dimensions, loads, and boundary conditions are symmetrical with regard to the axis. An axisymmetric finite element model is established to reduce the computational effort. Full constraints are imposed on the slip shell, and the suspension weight is simplified as an axial load acting on the casing. Finite element analysis (FEA) is an established standard procedure in many areas of numerical strength analysis **[21]** and **[22]**. According to the structure of the WE-type casing hanger and casing, assumptions are also made as follows to simplify the analysis model:

(1) The material is an elastoplastic body with isotropic and homogeneous properties;
(2) The effect of ovality and wall thickness unevenness of casing hanger and casing is neglected;
(3) The effect of the error in wellhead suspension installation is neglected.

A finite element model of the slips holding the casing was established according to the real hanger structure, and the model was meshed, as shown in Figs. 9 and 10. Mesh refinement of the slip inserts, the

Table 2. *Parameters of material properties of metal components*

Component	Material	Density [kg/m³]	Young's modulus [MPa]	Poisson's ratio	Yield strength [MPa]	Tensile strength [MPa]
Slips	718	7850	249350	0.3	980	1550
Slip bowl	30CrMo	7850	249350	0.3	785	930
Casing head	30CrMo	7850	249350	0.3	517	655

casing outer wall, the clip side surface, and the inner surface of the slip shell was carried out to obtain the accurate calculation results of contact between slips and the casing outer wall and between the slip side surface and the slip shell conical surface.

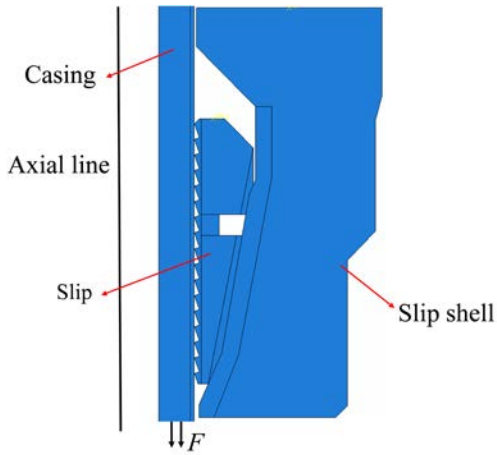

Fig. 9. *Finite element model of slips holding the case*

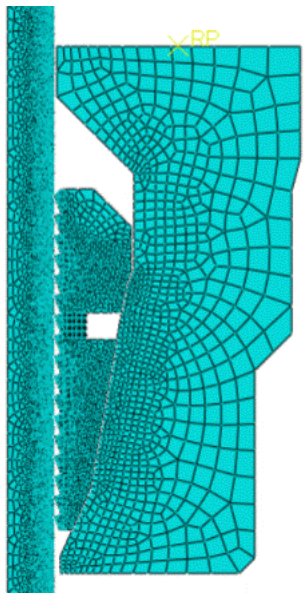

Fig. 10. *Meshing of model*

4 RESULTS AND DISCUSSION

4.1 Comparison of Results

The finite element simulation results are compared with the experimental bite marks on the casing surface to verify the correctness of the analysis results, as shown in Fig. 11.

According to Fig. 11, when the slip is holding the casing, the slip teeth squeeze the casing and bite into the casing wall. The slip teeth leave a bite mark with a clear texture on the casing surface. When the suspension load reaches a certain value, plastic deformation occurs on the bite mark. In addition, the simulated bite marks show that the bite marks are deeper in the lower part of the setting position. It can be proved that the establishment and analysis results of the finite element model are consistent with the experiment results.

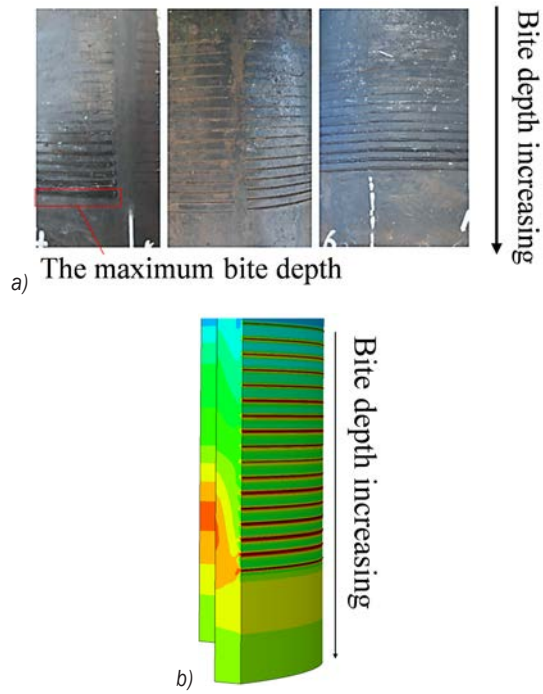

Fig. 11. *a) Experiment bite marks on the casing surface; b) simulated bite marks on the casing surface*

4.2 Relationship between Bite Depth and Suspension Load

The maximum depth of the slips bite into the casing when the suspended load is increased from 1000 kN to 6000 kN is simulated, as shown in Fig. 12. The maximum height of the slips bite into the casing gradually increases with the suspension load, which gradually enhances the plastic deformation of the casing surface.

When the slips bite into the casing surface, the bite depth of each tooth into the casing is different. Therefore, the teeth on the same slip are numbered sequentially from bottom to top, and the bite depth of all 17 teeth of the ϕ 273 mm WE-type hanger slips into the casing under different suspension loads was obtained, as illustrated in Fig. 13.

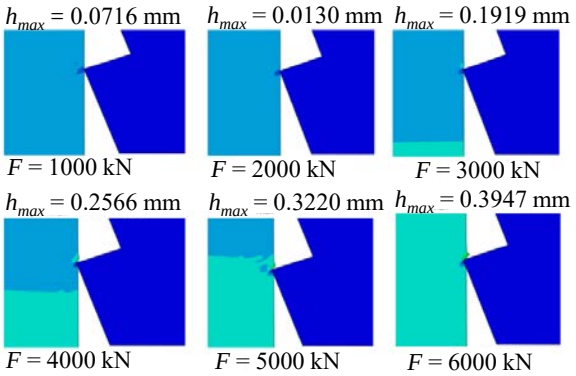

Fig. 12. *Maximum bite depth of casing surface under different suspension load*

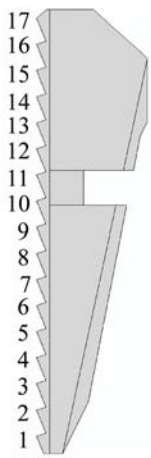

Fig. 13. *Number of slip hanger's teeth*

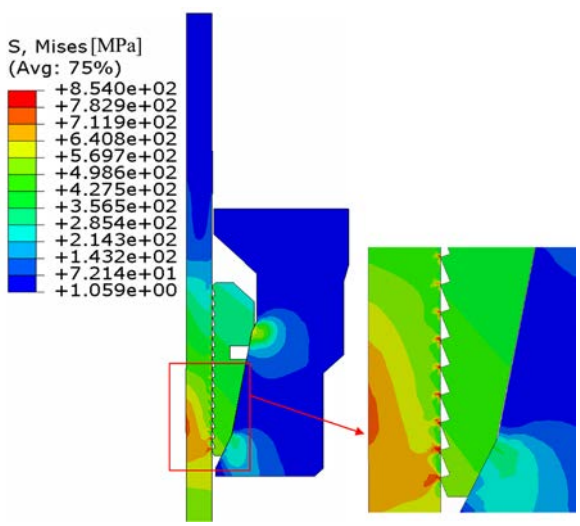

Fig. 14. *Equivalent stress cloud diagram of slip teeth biting into the casing*

According to Figs. 14 and 15, the bite depth of slip inserts into the casing is differentiated under the same suspension load, equivalent stress on the casing and the bite depth of slips gradually decreases from no. 1 to no. 17 (from bottom to top). With the increase of the suspension load, the bite depth of the slips gradually increases, and the increase in the bite depth of the slips is higher in the lower positions (smaller number).

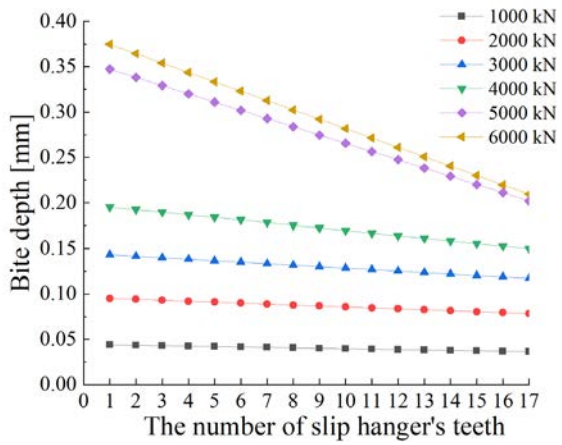

Fig. 15. *Relationship between the bite depth and the number of slip hanger's teeth, and the suspension load*

According to the finite element simulation results, the relationship between the suspension force and the maximum bite depth of the slip can be obtained, as shown in Fig. 16, which is used to fit the formula of the relationship between the suspension load and the maximum bite depth of the slip:

$$h_{\max} = 7E-11x^3 + 6E-8x^2 + 0.0006x + 0.0129, \quad (18)$$

where $h_{\max}$ is the maximum bite depth of slips [mm]; x is the suspension load [kN].

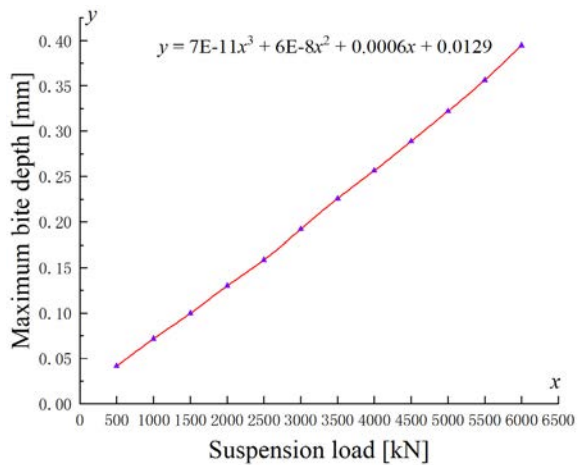

Fig. 16. *Relationship between the suspension load and the maximum bite depth of slips*

4.3 Relationship between the Suspension Load and the Residual Collapse Strength

When the slip inserts bite into the casing, the mechanical properties of the casing varies with the bite depth of the slips, which leads to variation in the collapse strength and suspension ability of the casing. Therefore, it is of great significance to study the effect of the bite depth of slips on the collapse strength and suspension ability of the casing. The cross-sectional schematic of the slip teeth bite into the casing is shown in Fig. 17. Assuming that the suspension load of the hanger at a certain moment is F, the corresponding maximum height of the slip insert bite into the casing is h_{max}. If the casing cross-sectional area is A_C [mm^2], the residual wall thickness of the casing at the maximum bite position is $t_s = t - h_{max}$ [mm], the residual diameter $D_S = D - 2h_{max}$ [mm], and the axial tensile stress is $Sa = F/A_C$ [MPa].

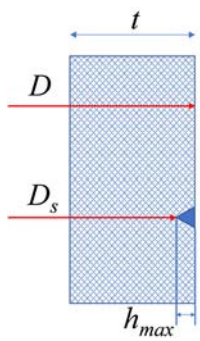

Fig. 17. *Profile of bite of slip insert into the casing*

The equivalent yield strength of the casing under the action of axial tensile stress is written as:

$$Y_{pa} = \left[\sqrt{1-0.75\left(\frac{S_a}{Y_p}\right)^2} - 0.5\frac{S_a}{Y_p}\right]Y_p, \quad (19)$$

where Y_{pa} is the equivalent yield strength of the casing under axial tensile stress [MPa], Y_p is the yield strength of the casing [MPa].

When $(D/t)_{YP} \leq D_S/t_S \leq (D/t)_{PT}$, is combined with the API formula for plastic collapse pressure and takes the safety factor as 1.5, the residual plastic collapse strength is written as:

$$P_{PS} = Y_{Pa}\left(\frac{A}{D_S/t_s} - B\right)/1.5 - 6.894757C, \quad (20)$$

where P_{PS} is residual plastic collapse strength [MPa], $(D/t)_{YP}$ is D/t limit value of yield strength collapse and plastic collapse, is the limit value of plastic collapse and elastic-plastic collapse, and casing steel grade coefficient.

The relationship between the suspension load and the residual collapse strength of the wellhead casing was obtained by integrating Eqs. (18) to (20), as shown in Fig. 18. As the suspension load increases, the casing residual collapse strength decreases. When decreases to a certain value, the maximum suspension force corresponding to the slips at a certain bite depth can be obtained. In practical application, considering the uneven wellhead or the error during installation of casing head, the residual collapse strength of the casing obtained in Fig. 18 should be divided by a "working condition factor".

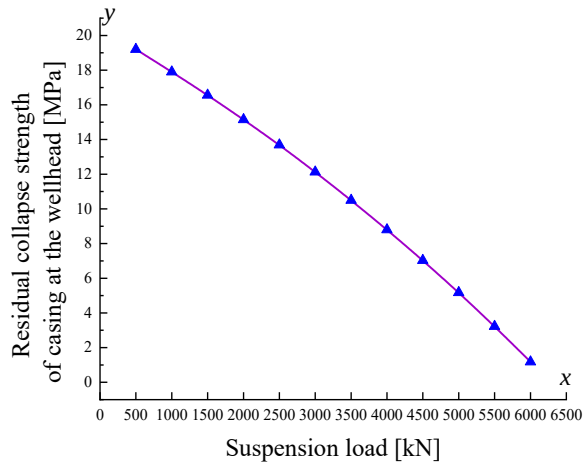

Fig. 18. *Relationship between the suspension load and the residual collapse strength of casing at the wellhead*

5 CONCLUSIONS

An axisymmetric finite element model of the hanger suspended the casing was established based on the real structure of the Φ273 mm WE slip hanger. The accuracy of the finite element model was proved by comparing the simulation results with the real bite marks on the casing surface.

The bite depths of slip inserts into the casing are different under a specific suspension load. The bite depth of the slips is gradually reduced from no. 1 to no. 17 (from bottom to top). With the increase of the suspension load from 1000 kN to 6000 kN, the maximum bite depth of slip inserts into the casing gradually increases from 0.07163 mm to 0.3947 mm, and the increase in the bite depth of the slips is higher in the lower positions (smaller number).

As the suspension load increases, the residual collapse strength of the casing decreases. When the

residual collapse strength decreases to a certain value, the maximum suspension force corresponding to the bite depth of slip inserts can be obtained.

6 REFERENCES

[1] Wen, J.L., Han, X.W., Xin, Z., Sheng, S.C. (2019). Sealing properties and structure optimization of packer rubber under high pressure and high temperature. *Petroleum Science*, vol. 16, no. 3, p. 632-644, **DOI:10.1007/s12182-018-0296-0**.

[2] Zhang, Z., Sang, P.F., Sang, Z., Hou, D., Lv, Y., Zheng, Y., Zhang, C. (2020). Analyzing failure of casing head slip hanger. *Engineering Failure Analysis*, vol. 108, art. ID. 104301, **DOI:10.1016/j.engfailanal.2019.104301**.

[3] Koc, P. (2019). An exacting wall-penetration pipe analysis. *Strojniški vestnik - Journal of Mechanical Engineering*, vol. 65, no. 3, p. 189-197, **DOI:10.5545/sv-jme.2018.5651**.

[4] Li, C., Guan, Z.C., Zhang, B., Wang, Q., Xie, H.Q., Yan, Y., Han, C. (2021). Failure and mitigation study of packer in the deep water HTHP gas well considering the temperature-pressure effect during well completion test. *Case Studies in Thermal Engineering*, vol. 26, art ID. 101021, **DOI:10.1016/j.csite.2021.101021**.

[5] Tong, S.K., Zhu, B.K., Cao, Y.P., Dou, Y.H. (2014). Analysis of the mechanical property of RTTS packer slip. *China Petroleum Machinery*, vol. 42, no. 2, p. 53-57, **DOI:10.3969/j.issn.1001-4578.2014.02.013**. (in Chinese)

[6] Tang, Y., Sun, p., Wang, G.R., Li, W. (2020). Analysis of pressure bearing performance and optimization of structural parameters of the slip in a compression packer. *Science Progress*, vol. 103, no. 1, p. 1-19, **DOI:10.1177/0036850419881106**.

[7] Mohammed, A.I., Oyeneyin, B., Atchison, B., Njuguna, J. (2019). Casing structural integrity and failure modes in a range of well types-A Review. *Journal of Natural Gas Science and Engineering*, vol. 68, art. ID 102898, **DOI:10.1016/j.jngse.2019.05.011**.

[8] Wang, Z.J., Deng, W.D., Lin, Z.C., Shang, X.F. (2013). Finite element analysis and structure improvements of packer slip in horizontal wells. *Oil Drilling & Production Technology*, vol. 35, no. 5, p. 78-81, **DOI:10.13639/j.odpt.2013.04.032**. (in Chinese)

[9] Xu, R., Wojtanowicz, A.K. (2017). Pressure buildup test analysis in wells with sustained casing pressure. *Journal of Natural Gas Science and Engineering*, vol. 38, p. 608-620, **DOI:10.1016/j.jngse.2016.12.033**.

[10] Ahmed, S., Salehi, S., Ezeakacha, C.P., Catalin Teodoriu, C. (2019). Evaluation of liner hanger seal assembly and cement sheath as a dual barrier system: Implications for industry standards. *Journal of Petroleum Science and Engineering*, vol. 178, p. 1092-1103, **DOI:10.1016/j.petrol.2019.04.017**.

[11] Kiran, R., Teodoriu, C., Dadmohammadi, Y., Nygaard, R., Wood, D., Mokhtari, M., Salehi, S. (2017). Identification and evaluation of well integrity and causes of failure of well integrity barriers (A review). *Journal of Natural Gas Science and Engineering*, vol. 45, p. 511-526, **DOI:10.1016/j.jngse.2017.05.009**.

[12] Chen, Y., Xiao, G.P., Zhong, W.J., Yi, H. (2020). Investigation of mechanical numerical simulation and expansion experiment of expandable liner hanger in oil and gas completion. *Shock and Vibration*, vol. 2020, art. ID 9375835, **DOI:10.1155/2020/9375835**.

[13] Patel, H., Salehi, S., Teodoriu, C., Ahmed, R. (2019). Performance evaluation and parametric study of elastomer seal in conventional hanger assembly. *Journal of Petroleum Science and Engineering*, vol. 175, p. 246-254, **DOI:10.1016/j.petrol.2018.12.051**.

[14] Ahmed, S., Salehi, S., Ezeakacha, C. (2020). Review of gas migration and wellbore leakage in liner hanger dual barrier system: Challenges and implications for industry. *Journal of Natural Gas Science and Engineering*, vol. 78, p. 103284, **DOI:10.1016/j.jngse.2020.103284**.

[15] Al-Abri, O.S., Pervez, T. (2013). Structural behavior of solid expandable tubular undergoes radial expansion process-Analytical, numerical, and experimental approaches. *International Journal of Solids and Structures*, vol. 50, no. 19, p. 2980-2994, **DOI:10.1016/j.ijsolstr.2013.05.013**.

[16] Meng, H., Ge, H.K., Fu, D.W., Wang, X., Shen, Y., Jinag, Z., Wang, J. (2020). Numerical investigation of casing shear deformation due to fracture/fault slip during hydraulic fracturing. *Energy Science & Engineering*, vol. 8, no. 10, p. 3588-3601, **DOI:10.1002/ese3.766**.

[17] Zhang, Z., Shao, L.Y., Zhang, Q.S., Zhang, C., Li, J., Zeng, D., Zhong, X., Hu, J., Hou, D., Shi, T. (2017). Environmentally assisted cracking performance research on casing for sour gas wells. *Journal of Petroleum Science and Engineering*, vol. 118, p. 729-738, **DOI:10.1016/j.petrol.2017.08.050**.

[18] White, S.P., Weir, G.J., Laycock, N.J. (2000). Calculating chemical concentrations during the initiation of crevice corrosion. *Corrosion Science*, vol. 42, no. 4, p. 605-629, **DOI:10.1016/S0010-938X(99)00097-9**.

[19] Sharland, S.M. (1992). A mathematical model of the initiation of crevice corrosion in metals. *Corrosion Science*, vol. 33, no. 2, p. 183-201, **DOI:10.1016/0010-938X(92)90144-R**.

[20] Xu, Z.L. (2016). Polar solutions to plane problems. In Zhao, X.D. (ed.) *Elasticity*. Higher Education Press, Beijing, p. 73-77.

[21] Glenk, C., Hüter, F., Billenstein, D., Rieg, F. (2018). Consideration of body forces within finite element analysis. *Strojniški vestnik - Journal of Mechanical Engineering*, vol. 64, no. 5, p. 303-309, **DOI:10.5545/sv-jme.2017.5081**.

[22] Wang, H.L., Long, B., Yang, Y., Xiao, Y., Wang, C. (2020). Modelling the Influence of Inlet Angle Change on the Performance of Submersible Well Pumps. *International Journal of Simulation Modelling*, vol. 19, no. 1, p. 100-111, **DOI:10.2507/IJSIMM19-1-506**.

Strojniški vestnik - Journal of Mechanical Engineering 67(2021)10, 525-533

DOI:10.5545/sv-jme.2021.7246 Original Scientific Paper
Received for review: 2021-05-06
Received revised form: 2021-07-27
Accepted for publication: 2021-09-24

Optimization of Laser Parameters and Dimple Geometry Using PCA-Coupled GRG

Saravanan Kandasamy Ganesan[1] – Thanigaivelan Rajasekaran[2,*]

[1] Sona College of Technology, India
[2] Muthayammal Engineering College, India

Stainless steel (SS316L) is applied in numerous fields due to its intrinsic properties. In this study, micro-dimples were fabricated on SS316L. The effects of laser process parameters, such as frequency, average power, and pulse duration, on the average dimple diameter, dimple distance, and dimple depth were studied using an L_9 orthogonal array. The analysis of variance (ANOVA) and multi-objective optimization technique, principal-component-analysis-coupled grey relational grade (GRG), was used to optimize laser process parameters on output responses. The optimal machining parameter settings obtained for the highest GRG peak value of 0.2642 are 15 kHz (frequency), 12 W (average power), and 1500 ns (pulse duration). The ANOVA results showed that average power is the most influential factor, contributing 86.40 % to performance measures (average dimple diameter (φ), dimple distance (d), and depth (l). Moreover, the effect of process parameters was studied using mean effect plots, and the micro-dimple quality was analysed using SEM micrographs.

Keywords: laser, micro-dimple, principal component analysis, grey relational grade, stainless steel

Highlights

- *Micro-dimples were fabricated on SS316L.*
- *The effects of laser process parameters, such as frequency(F), average power (P), and pulse duration (t) on the average dimple diameter (φ), dimple distance (d), and depth (l) were studied using an L9 orthogonal array (OA).*
- *The analysis of variance (ANOVA) and multi-objective optimization techniques, including grey relational grade (GRG) and principal component analysis (PCA), were used to optimize laser process parameters on output responses.*
- *In the sequence of the significance of controllable factors to the multi-performance characteristics in the laser process is as follows: frequency, pulse duration, and average power.*

0 INTRODUCTION

Stainless steel finds applications in food processing, pharmaceutical equipment, medical devices, potable water, and wastewater treatment industries due to its improved corrosive resistance property. Although stainless steel alloys have excellent properties, including corrosion resistance, higher strength and hardness, their tribological action is not satisfactory in biomedical applications, in particular for hip prostheses that require sliding contact [1]. Moreover, for biomedical applications, stainless steel alloy surfaces must be modified for tissue attachment and wear resistance [2]. Hence, their surface properties must be improved, and numerous methods, such as plasma and flame coatings, shot peening, thermal oxidation, nano-composite coatings, and ball burnishing, are available [3]. Each process has advantages and limitations. In this study, laser texturing was employed to improve the wear resistance of the stainless steel alloy surfaces. Laser texturing can be used to modify the SS-316L surface by generating micro-dimples to improve its properties under service conditions. Kovacı and Seçer [4] investigated the effects of different surface textures acquired through selective laser melting on the mechanical properties of AISI 316L stainless steel. Their results showed that the effects of surface textures and the area density on friction and wear properties were highly significant. Liew et al. [5] studied the effect of the dimple geometry with different textural shapes and orientations on friction and reported that geometric factors, such as the shape dimple area, area ratio, and dimple depth, considerably influence the load-carrying capacity of contacting surfaces. Yu et al. [6] investigated the effect of different dimple shapes on the tribological performance of surface textures. The dimple area ratio and depth considerably affect the friction reduction. According to the literature, surface modification plays a key role in improving the mechanical properties of materials. The fabrication of micro-dimples by using laser and control of process parameters on geometrical features were considered in [6]. Li et al. [7] fabricated the micro-dimples by using laser peen texturing on SUS304 stainless steel and found that the diameter, depth, and aspect ratio of the micro-dimples increased with laser power density. Dai et al. [8] used masked laser ablation to fabricate a micro-dimple array on a substrate surface with a pulsed Nd:YAG laser, investigated the influence of processing parameters on the micro-

*Corr. Author's Address: Muthayammal Engineering College, Rasipuram, India, tvelan10@gmail.com

dimple morphology, and developed clean periphery micro-dimples. Ahmed et al. [9] reviewed the effect of the geometrical parameters of micro-dimples on piston/cylinder assembly and concluded that the high dimple depth is unfavourable for development for starved lubrication. The most crucial parameter to enhance the tribological performance of piston ring/cylinder assembly is the aspect ratio [9]. Won and Kim [10] developed masked laser surface texturing to produce hundreds of micro-patterns. The number of laser pulses substantially affects uniform pattern formation [10]. Puoza et al. [11] micro-machined 45 steel, GCr15 steel, and grey cast iron materials by using laser processing technologies and analysed the features, including the diameter and depth, of the ablated micro-dimples. The diameter and depth of the micro-dimples generally increased with an increase in the laser fluence for all the materials [11]. Behera et al. [12] fabricated micro-channels and micro-dimples with different dimensions on anSS-304 alloy surface by using the pulsed Nd:YAG laser beam and studied the effects of process parameters, such as laser scanning speed, current, laser pulse frequency, and pulse duration, on the diameter and depth of micro-features. The dimensions of micro-features decreased an increase in the scanning speed and increased with an increase in the pulse frequency, pulse duration, and current [12]. Researchers have synthesized various micro-features with diverse dimensions for numerous applications. To improve the adherence of coatings with substrates, Lamraoui et al. [13] fabricated micro-dimples with a diameters and depths of 60 μm to 90 μm and 60 μm to 120 μm, respectively. Teleginski et al. [14] textured micro-dimples of 200 μm diameter on a material. Gajrani et al. [15] developed micro-dimples with the diameter and depth of 250 μm and 50 μm on a cutting tool for lubrication retention.

Researchers have used lasers to modify alloy surfaces for various applications, and the optimal use of laser process parameters for efficient production and high accuracy requires the proper control of input parameters. Although lasers have been used for alloy surface modification, no systematic study has reported the optimization of the laser process by using a multi-objective optimization technique. Hence, in this study, micro-dimples were fabricated on SS316L, and the effects of laser factors such as frequency (F), average power (P), and pulse duration (t) on the average dimple diameter (φ), dimple distance (d), and depth (l) were studied using an L_9 orthogonal array (OA). The analysis of variance (ANOVA) and multi-objective optimization techniques, including grey relational grade (GRG) and principal component analysis (PCA), were used to optimize laser process parameters on output responses. Moreover, the laser parameters must be optimized on geometrical parameters; otherwise, the laser parameters may negatively affect output performance.

1 METHODS

In this study, the SS316L alloy was selected as the workpiece material. Surgical 316L stainless ssteel was purchased from SAIL and its composition (wt %) are17.20 Cr, 12.60 Ni, 2.40 Mo, 1.95 Mn, 1Si, 0.03 C, 0.02 N, and balance Fe [16]. Nine samples with the length, width, and thickness of 25 mm, 25 mm, and 5mm, respectively, were used. The specimens were cleaned with acetone and immersed in an ultrasonic vibrator for 1min, and again, were cleaned with deionized water. The factors considered for the experiments are frequency (F) in kHz, average power (P) in Watts, and pulse duration (t) in nanoseconds. The factors are selected based on the preliminary experiments. Each factor has three levels, as seen in Table 1. OA was selected based on the degrees of freedom (DoF). DoF is used to determine how many runs are required to develop a parameter estimate. Each parameter estimate attracts one DoF from the total number of DoFs offered. The numbers of factors and levels were three and three, respectively. Thus, the multiplication of the number of factors with the difference between the number of levels and 1 provides DoF. The selected OA should be higher than DoF; therefore, based on the relevant calculation, $3(3-1)$ provides six DoFs, and selected OA is larger than 6, that is, L_9 OA [3]. The average dimple diameter (φ), dimple distance (d), and depth (l) were measured three times.

2 EXPERIMENTAL

Laser dimples were generated on the specimen according to the L_9 OA experimental design (Table 1). A fibre laser (CK-FB(A); Meera Laser Solutions) emitting a Gaussian beam at 1030 nm with the maximum output power and frequency of 20 W and 25 kHz, respectively, was used. The standoff distance was maintained at 0.7 mm. The quality of the laser beam highly depends on its polarization state. In practice, laser texturing is normally performed by the beam with circular and chaotic polarization for the fibre laser. The dimples are made with multiple pulses, and the laser jumps from dimple to dimple. The spot diameter of the laser beam on stainless steel was 150 μm. The dimple depth and diameter

Table 1. *L9 OA and output responses*

Sample number	F [kHz]	P [W]	T [ns]	φ [μm]	d [μm]	l [μm]	*STDEV*		
							φ	d	l
1	10	12	500	166.3	274.3	16.3	0.141	0.681	0.153
2	10	14	1000	161.2	265.4	15.4	0.833	0.200	0.200
3	10	16	1500	168.5	272.5	16.2	1.258	0.839	0.306
4	15	12	1500	173.9	250.2	17.3	0.709	0.404	0.100
5	15	14	500	171.7	252.1	16.8	1.159	0.153	0.231
6	15	16	1000	157.2	300.5	15.6	0.757	0.500	0.458
7	20	12	1000	134.9	335.3	13.9	0.586	0.252	0.361
8	20	14	1500	140.4	340.2	14.2	0.306	0.902	0.306
9	20	16	500	138.0	366.6	13.6	0.529	0.808	0.458

were characterized and analysed using a non-contact 3D surface profilometer (made by Taylor Hobson) and scanning electron microscopy. The time of laser hatching was recorded from the laser machine display. Fig. 1 illustrates the schematic of the micro-dimple geometry.

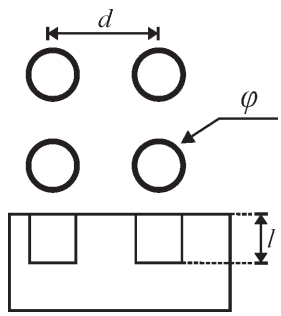

Fig. 1. *Schematic of the micro-dimples on a substrate*

2.1 Grey Relational Analysis

OA with the grey relational analysis (GRA) was used to determine the optimal machining parameters. In general, for GRG, each series is normalized by dividing the data into the original series by using their average [17]. Let the original reference and comparison sequences be $x_i^*(k)$ and $x_i(k)$, respectively, i = 1, 2,..., m; k = 1, 2,..., n, where m and n are the total number of experiments and observed data, respectively. Data pre-processing is used to convert the original sequence into an identical sequence. Several data pre-processing methods can be used in GRA, depending on the characteristics of the original sequence.

If the target value of the original sequence is "the-larger-the-better", then the original sequence can be normalized (Eq. (1)) as follows:

$$x_i^*(k) = \frac{x_i(k) - \min x_i(k)}{\max x_i(k) - \min x_i(k)}. \quad (1)$$

If the purpose is "the-smaller-the-better", then the original sequence can be normalized (Eq.(2)) as follows:

$$x_i^*(k) = \frac{\max x_i(k) - x_i(k)}{\max x_i(k) - \min x_i(k)}. \quad (2)$$

After data pre-processing, a grey relational coefficient (GRC) can be calculated using the pre-processed sequences. GRC (Eq. (3)) are defined as follows:

$$\xi_i(k) = \frac{\Delta_{\min} + \zeta\Delta_{\max}}{\Delta_{oi}(k) + \zeta\Delta_{\max}}, \quad (3)$$

where $\Delta_{oi}(k)$ is the deviation sequence of the reference sequence $x_0^*(k)$, $x_i^*(k)$ is the comparability sequence, and ζ is the distinguishing coefficient, ζ. GRG (Eq. (4)) is a weighted sum of the GRC defined as follows:

$$\gamma_i = \frac{1}{n}\sum_{k=1}^{n}\xi_i(k), \quad (4)$$

where GRG γ_i represents the level of correlation between the reference and comparability sequences.

2.2 Multivariate Statistical Technique

PCA is a multivariate statistical technique developed by Pearson [18] and adapted by Hotelling [19]. In this technique, several correlated variables are transformed into fewer uncorrelated variables. These transformed uncorrelated variables are called principal components (PCs) and are the linear combinations of response variables. Following steps are involved in PCA [20]:

Step 1. Formation of the decision matrix.

An array of original response variables is constructed as the decision matrix as in Eq. (5).

$$\begin{bmatrix} \mathbf{x}_{11} & \mathbf{x}_{12} & \mathbf{x}_{13} & \cdots & \mathbf{x}_{1n} \\ \mathbf{x}_{21} & \mathbf{x}_{22} & \mathbf{x}_{23} & \cdots & \mathbf{x}_{2n} \\ \mathbf{x}_{31} & \mathbf{x}_{32} & \mathbf{x}_{33} & \cdots & \mathbf{x}_{3n} \\ \vdots & \vdots & \vdots & \ddots & \vdots \\ \mathbf{x}_{m1} & \mathbf{x}_{m2} & \mathbf{x}_{m3} & \cdots & \mathbf{x}_{mn} \end{bmatrix}, \quad (5)$$

where, **X** is the decision matrix of the response variables, n and m are the numbers of output characteristics and experimental observations, respectively. Output characteristics n = 3, m = 9, and decision matrix **X** is obtained as the GRC array of individual responses.

Step 2. The correlation coefficient array can be acquired from the decision matrix and is expressed as Eq.(6).

$$C_{\alpha\beta} = \frac{\left(Cov\left(x_i(\alpha)\right), x_i(\beta)\right)}{\sigma x_i(\alpha) \times \sigma x_i(\beta)}, \quad (6)$$

where, ($Cov(x_i(\alpha), x_i(\beta))$ is the covariance of the sequences ($x_i(\alpha)$), ($x_i(\beta)$), $\sigma x_i(\alpha)$ is standard deviation (SD) $\sigma x_i(\alpha)$, and $\sigma x_i(\beta) = SD$ of $\sigma x_i(\beta)$. α = 1, 2, ..., n, β = 1, 2, ..., n. $C_{\alpha\beta}$ elements are mainly the correlation coefficients of the entire combinations of performance measures such as dimple diameter, dimple distance, and dimple depth.

Step 3. Determination of Eigenvalues and vectors.

Eigenvalues and vectors are estimated from $C_{\alpha\beta}$ by using Eq. (7).

$$E_{ik} = \left[C_{\alpha\beta} - \delta_k I_m \right], \quad (7)$$

where, δ_k is the Eigenvalue such that $\sum_{k=1}^{n} \delta_k = n$, and E_{ik} is the Eigenvector corresponding to Eigenvalue δ_k.

Step 4. Estimation of PCs.

PCs are estimated using Eq. (8) and are arranged in the decreasing order of variations captured by them. Hence, the highest variability in the data is generally explained using the first principal component.

$$P_{mk} = \sum_{i=1}^{n} x_m(i) \times E_{ik}, \quad (8)$$

where P_{mk} is the first PC.

PCA GRG is estimated using Eq. (9).

$$G_i = \in \sum_{i=1}^{n} W_j \left(\sum_{i=1}^{n} x_m(i) \right). \quad (9)$$

3 RESULTS

Performance measures, such as the average dimple diameter, dimple distance, and dimple depth, were considered. An increase in the average dimple diameter leads to the enhancement of lubrication storage for tribological applications and cell adherence in biomedical applications; thus, "the-larger-the-better" is considered the optimum condition. A decrease in the dimple depth and distance is effective to minimize the friction and wear; hence, "the-smaller-the-better" condition is used for the analysis. The original sequence is normalized using Eqs. (1) and (2) **[21]**. Subsequently, the deviation sequence is determined by subtracting the comparable sequence from the ideal sequence. GRC for output responses are calculated using Eq. (3) (Table 2). The PCA procedure is adapted to calculate the optimized weights. The GRC of the average dimple diameter, dimple distance, and depth are used as the elements of the decision matrix, which is used to calculate the correlation coefficient array and Eigenvalues using Eqs. (6) and (7), respectively. Table 3 presents the Eigenvalues and proportions for PCs. The first, second, and third PCs, that is, average dimple diameter, dimple distance, and dimple depth, respectively, account for 34.6 %, 34.5 %, and 31 % of variations, respectively, in GRG. Therefore, the accountability proportions of the first, second, and third PCs of 0.346, 0.345, and 0.310 are considered the optimum weights for the average dimple diameter, dimple distance, and dimple depth (Table 4).

Table 2. *Calculated GRC value*

Sample number	φ [μm]	d [μm]	l [μm]
1	0.7196	0.7072	0.4066
2	0.6056	0.7929	0.5068
3	0.7831	0.7230	0.4157
4	1.0000	1.0000	0.3333
5	0.8986	0.9684	0.3663
6	0.5387	0.5364	0.4805
7	0.3333	0.4061	0.8605
8	0.3679	0.3927	0.7551
9	0.3520	0.3333	1.0000

GRG was calculated by taking the average of GRCs matching to each process response by using

Eq. (9). The overall estimation of multiple response process parameters was based on GRG (Table 5), and the experiment with the highest GRG is optimal among all the runs. The GRG for each L_9 OA experiment was used to optimize laser process parameters (Table 5). Subsequently, the GRG of each combination was ranked as per value, and a set of optimal machining parameter settings was obtained based on the highest GRG peak value of 0.2642 with 15 kHz (frequency), 12 W (average power), and 1500 ns (pulse duration). The result indicated that experiment sample number 4 (Table 5) shows desirable responses among the nine experiments.

Table 3. *Eigen values and proportions for PC*

PC	Eigen values	Proportion [%]
First	0.1694	94.3
Second	0.0077	4.3
Third	0.0025	1.4

Table 4. *Accountability proportion of output responses*

Output parameters	Eigen vectors			Contribution (W_j)
	PC1	PC2	PC3	
φ (μm)	0.586	0.316	–0.746	0.346
d (μm)	0.588	0.468	0.660	0.345
l (μm)	–0.557	0.826	–0.088	0.310

Table 5. *Ranking of parameter combination*

Sample number	F [kHz]	P [W]	T [ns]	G_i	Rank
1	10	12	500	0.2059	5
2	10	14	1000	0.2131	4
3	10	16	1500	0.2160	3
4	15	12	1500	0.2642	1
5	15	14	500	0.2524	2
6	15	16	1000	0.1732	8
7	20	12	1000	0.1739	7
8	20	14	1500	0.1655	9
9	20	16	500	0.1821	6

Fig. 2 shows the micro-dimples machined for the optimum combination of parameters: 15 kHz (frequency), 12 W (average power), and 1500 ns (pulse duration). The pile-up phenomenon around the dimples (Fig. 2a) contributes to limiting the contact surface, leading to decreased wear. Fig. 2b shows the magnified view of micro-dimples and depicts the rough surface and re-solidified/re-cast areas. The re-solidified and re-cast layers on the micro-dimple resulted from the medium scanning speed, where material heat absorption decreased, leading to incomplete melting.

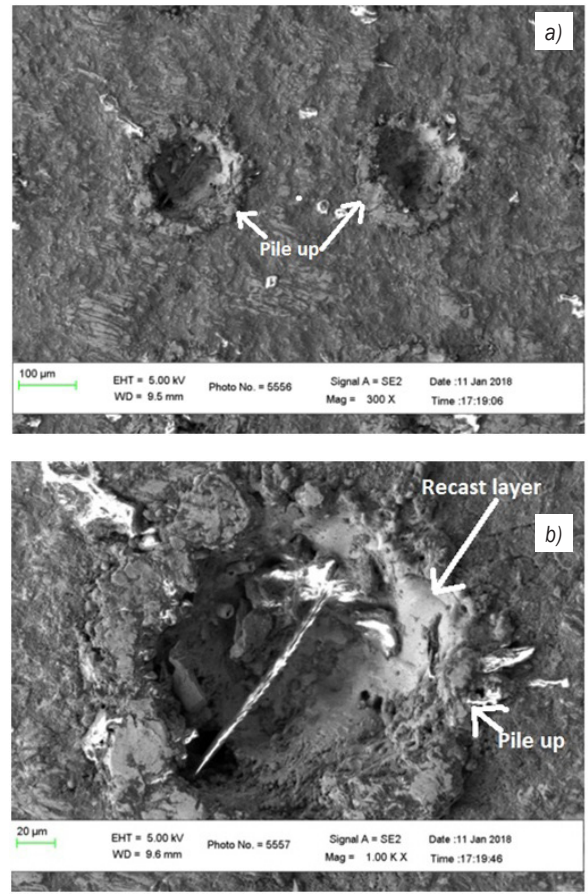

Fig. 2. *Micro-dimple machined at optimum laser parameters, a) micro-dimple, b) a magnified view of the micro-dimple*

The most significant factors of machining parameters are determined by estimating the difference between the maximum and minimum values of mean GRG.The values are 0.2299, 0.2147, and 0.2168 for the frequency, average power, and pulse duration, respectively. The result showed that the frequency (0.2299) has the most decisive influence on multi-performance characteristics. In the sequence, the order of significance of controllable factors to multi-performance characteristics in the laser process is as follows: frequency, pulse duration, and average power. An increase in the pulse frequency improves laser spot extension leading to large and deep micro-dimples. At the frequency of 15 kHz, the pulsed laser beam exposed to the particular area of the workpiece causes heating and melting. With an increase in the pulse duration, the material exposure time increases,

and hence, heat transfer to the workpiece increases. The pulse duration of 1500 ns contributes to the generation of wide and deep dimples.

4 DISCUSSION

Fig. 3 presents the mean effect plot for output performance. With the frequency increase, output performance increases. The pulse frequency is the number of pulses per unit of time. With the increase in the pulse frequency, the number of pulses per second also increases. When a pulsed laser beam focuses on the SS316L workpiece surface, the required area on the substrate heats, melts and/or evaporates. Moreover, overlapping between the laser spots results in material removal. Thus, an increase in the pulse frequency causes overlapping between the laser spots, resulting in highly prominent diameter micro-dimples. The further increase in the frequency and improper ejection of molten materials hinder micro-dimple formation. The increase in laser power leads to a decrease in output performance. The increasing of power attributes to material removal, and the inadequate removal of molten materials reduces output performance. The

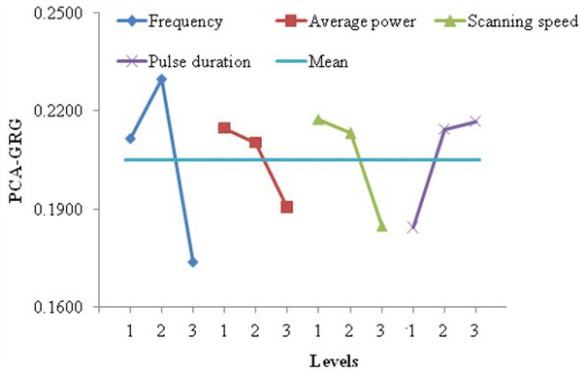

Fig. 3. *Mean effect plot for output performance*

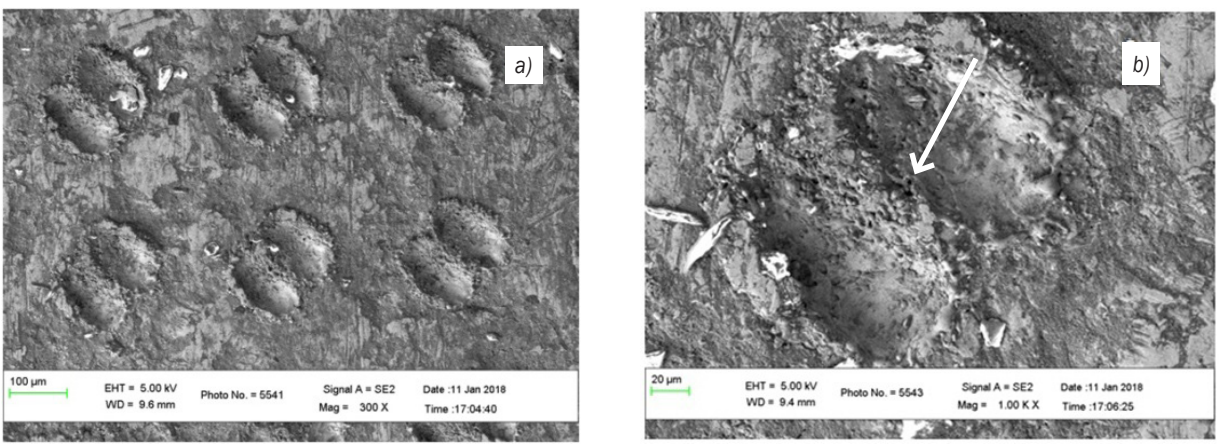

Fig. 4. *a) Micro-dimples, and b) a magnified view of the dimple*

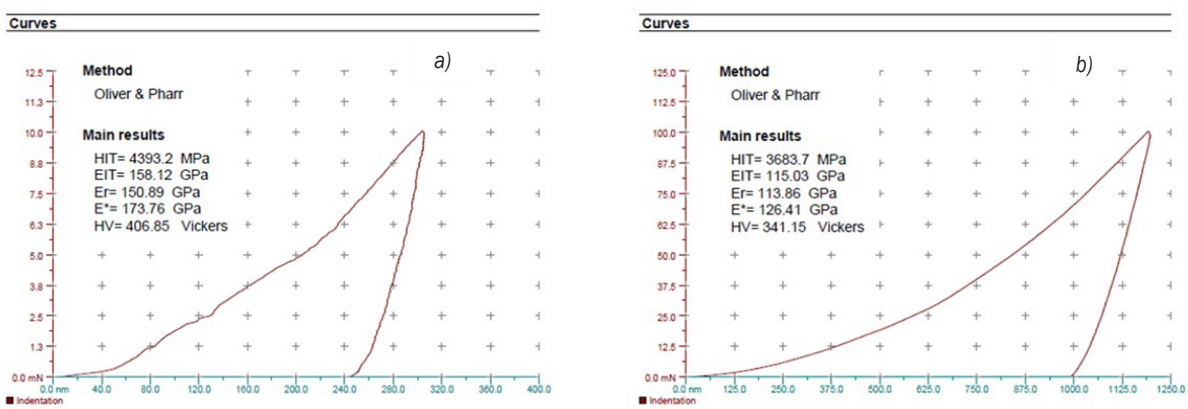

Fig. 5. *Loading and unloading graphs of Vickers hardness for a) 10 mN, and b) 100 mN*

important factor that significantly affects the micro-dimple quality is the interaction time between the laser beam and material. During interaction time, heat absorption of the material decreases, resulting in unfinished melting and the evaporation of the material surface, which leads to a decrease in the dimple diameter, distance, and depth. Fig. 4 illustrates the machined micro-dimples. The factor pulse duration exhibits an increasing trend in output responses. With an increase in the pulse duration, the laser exposure time on materials increases, contributing to an increase in output responses. Fig. 5 presents the loading and unloading graphs of Vickers hardness. The force was steadily lowered from 10 mN to 0 mN and 100 mN to 0 mN. The load and penetration depth of the indenter were continuously measured under the load-unload conditions. The nano-indentation test showed the hardness of 406.85 HV and 341.15 HV for 10 mN and 100 mN loadings, respectively. The Vickers hardness of SS316L was 140 HV in the non-laser irradiation area, and hardness increased almost three times. The arrow mark presented in Fig. 5b shows the measurement positions on the dimple for the Vickers hardness test.

4.1 ANOVA for PCA–GRG

ANOVA is used to determine the most influencing parameter and to estimate the contribution percentage of laser process parameters [22] and [23]. ANOVA is a statistical tool employed to obtain the experimental results and to establish the performance of a group of analysed parameters. The total variance of an observed value can be calculated using the sum of squares (SS). Moreover, the sample variance is considered the mean square, which is obtained by dividing SS with the respective DoF. The *F*-value is the ratio of two variances and shows how far the values are scattered from the mean value. Larger *F*-values represent higher dispersion within the group. As per the ANOVA (Table 6), the average power is the most influential factor, contributing 86.40 % to the performance measures, followed by the pulse duration [ns], and frequency [kHz], which contributes11.66 %, and 1.77 % to these measures. It is evident from the literature that the ablation mechanism is determined by applied power, and pulses have the least significance [24]. According to the comparison of the analytical mean results of PCA-GRG and ANOVA, the frequency and average power are the most significant parameters for dimple creation. This result variation was obtained because within the mean effect calculation, the difference between the two groups was considered, and in ANOVA, the variation between the sample means and the variation within each sample was considered.

5 CONCLUSIONS

In this study, micro-dimples were fabricated on SS316L, and the effects of laser process parameters such as the frequency, average power, and pulse duration on the average dimple diameter, dimple distance, and dimple depth were studied by using L_9 OA. The performance measures were optimized using PCA-coupled GRG. The following conclusions are drawn from the study.

1. The micro-dimples were successfully fabricated on the SS316L samples of 25 mm × 25 mm × 5 mm.
2. The optimal laser parameter setting for suitable micro-dimple generation for tribological applications is 15 kHz (frequency), 12 W (average power), and 1500 ns (pulse duration).
3. The most significant factors influencing micro-dimple generation are frequency and average power.
4. In the sequence, the order of significance of controllable factors to the multi-performance characteristics in the laser process is as follows: frequency, pulse duration, and average power.
5. With the increase in laser power, output performance decreases.
6. The development of a research model for predicting the number of micro-dimples for

Table 6. *ANOVA results*

Factors	DoF	SS	MS	F-value	Percentage contribution [%]
F	2	0.0000901	0.00004505	12.18	1.7786
P	2	0.0043769	0.00218845	591.47	86.4060
t	2	0.0005911	0.00029555	79.88	11.6691
Error	2	0.0000074	0.0000037	1	0.1460
Total	8	0.0067852	0.00084815	684.53	~ 100

given area will be considered for further studies using the RSM model.

6 ACKNOWLEDGEMENTS

This manuscript was edited by editingindia.

7 REFERENCES

[1] Fellah, M., Labaïz, M., Assala, O., Iost, A., Dekhil, L. (2013). Tribological behaviour of AISI 316L stainless steel for biomedical applications. *Tribology - Materials, Surfaces & Interfaces*, vol. 7, no. 3, p. 135-149, **DOI:10.1179/1751584X13Y.0000000032**.

[2] Bekmurzayeva, A., Duncanson, W.Jr., Azevedo, H.S., Kanayeva, D. (2018). Surface modification of stainless steel for biomedical applications: Revisiting a century-old material. *Materials Science and Engineering: C*, vol. 93, p. 1073-1089, **DOI:10.1016/j.msec.2018.08.049**.

[3] Thanigaivelan, R., Arunachalam, R.M., Nithish, A., Venkatesh, S., Naveenkumar, P., Selvaganapathy, S., Siranjeevi, A.A.S. (2020). Optimization of laser and electrochemical process parameters for surface modification of hardness and hydrophobicity on 316L steel. *Lasers in Engineering*, vol. 45, no. 1-3, p. 69-84.

[4] Kovacı, H., Seçer, Y. (2020). Improved tribological performance of AISI 316L stainless steel by a combined surface treatment: Surface texturing by selective laser melting and plasma nitriding. *Surface and Coatings Technology*, vol. 400, art. ID 126178, **DOI:10.1016/j.surfcoat.2020.126178**.

[5] Liew, K.W., Kok, C.K., Ervina Efzan, M.N. (2016). Effect of EDM dimple geometry on friction reduction under boundary and mixed lubrication. *Tribology International*, vol. 101, p. 1-9, **DOI:10.1016/j.triboint.2016.03.029**.

[6] Yu, H., Deng, H., Huang, W., Wang, X. (2011) The effect of dimple shapes on friction of parallel surfaces. *Proceedings of The Institution of Mechanical Engineers Part J: Journal of Engineering Tribology*, vol. 225, no. 8, p. 693-703, **DOI:10.1177/1350650111406045**.

[7] Li, K., Hu, Y., Yao, Z. (2013). Experimental study of micro dimple fabrication based on laser shock processing. *Optics & Laser Technology*, vol. 48, p. 216-225, **DOI:10.1016/j.optlastec.2012.09.015**.

[8] Dai, F.Z., Wen, D.P, Zhang, Y.K., Lu, J.Z, Ren, X.D., Zhou, J.Z. (2015). Micro-dimple array fabricated on surface of Ti6Al4V with a masked laser ablation method in air and water. *Materials and Design*, vol. 84, p. 178-184, **DOI:10.1016/j.matdes.2015.06.137**.

[9] Ahmed, A., Masjuki, H.H., Varman., M., Kalam, M.A., Habibullah, M., Al Mahmud, K.A.H. (2016). An overview of geometrical parameters of surface texturing for piston/cylinder assembly and mechanical seals. *Meccanica*, vol. 51, p. 9-23, **DOI:10.1007/s11012-015-0180-6**.

[10] Won, S.J., Kim, H.S. (2019). Effects of laser parameters on morphological change and surface properties of aluminum alloy in masked laser surface texturing. *Journal of Manufacturing Processes*, vol. 48, p. 260-269, **DOI:10.1016/j.jmapro.2019.10.034**.

[11] Puoza,J.C., Hua, X., Liu, Q., Kang, Z., Zhang, P. (2018). Manufacturing of micro-textures on metals by nanosecond laser micromachining. *Advances in Materials and Processing Technologies*, vol. 4, no. 1, p. 86-99, **DOI:10.1080/2374068X.2017.1406268**.

[12] Behera, R.R., Babu, P.M., Gajrani, K.K., Sankar, M.R. (2017). Fabrication of micro-features on 304 stainless steel (SS-304) using Nd: YAG laser beam micro-machining. *International Journal of Additive and Subtractive Materials Manufacturing*, vol. 1, no. 3-4, p. 338-359, **DOI:10.1504/IJASMM.2017.089929**.

[13] Lamraoui, A., Costil, S., Langlade, C., Coddet, C. (2010). Laser surface texturing (LST) treatment before thermal spraying: A new process to improve the substrate-coating adherence. *Surface and Coatings Technology*, vol. 205, p. S164-D167, **DOI:10.1016/j.surfcoat.2010.07.044**.

[14] Teleginski, V., Chagas, D.C., Costa de Oliveira, A.C., Santos, J.C.G., Azevedo, J.F., Riva, R., de Vasconcelos, G. (2014).Yb: fiber laser surface texturing of stainless steel substrate, with MCrAlY deposition and CO_2 laser treatment. *Surface and Coatings Technology*, vol. 260, p. 251-259, **DOI:10.1016/j.surfcoat.2014.06.076**.

[15] Gajrani, K.K., Reddy, R.P.K., Sankar, M.R. (2016). Experimental comparative study of conventional, micro-textured and coated micro-textured tools during machining of hardened AISI 1040 alloy steel. *International Journal of Machining and Machinability of Materials*, vol. 18, no. 5-6, p. 522-539, **DOI:10.1504/IJMMM.2016.078982**.

[16] Sivaraj, D., Vijayalakshmi, K. (2019). Enhanced antibacterial and corrosion resistance properties of Ag substituted hydroxyapatite/functionalized multiwall carbon nanotube nanocomposite coating on 316L stainless steel for biomedical application. *Ultrasonics sonochemistry*, vol. 59, art. ID 104730, **DOI:10.1016/j.ultsonch.2019.104730**.

[17] Thanigaivelan, R., Arunachalam, R.M. (2013). Optimization of process parameters on machining rate and overcut in electrochemical micromachining using grey relational analysis. *Journal of Scientific and Industrial Research*, vol. 72, no. 1, p.36-42.

[18] Pearson, K. (1901). On lines and planes of closest fit to systems of points in space. *The London, Edinburgh, and Dublin Philosophical Magazine and Journal of Science,* vol. 2, p. 559-572, **DOI:10.1080/14786440109462720**.

[19] Hotelling, H. (1993). Analysis of a complex of statistical variables into principal components. *Journal of Educational Psychology*, vol. 24, p. 417-441, **DOI:10.1037/h0071325**.

[20] Sonawane, S.A., Kulkarni, M.L. (2018). Optimization of machining parameters of WEDM for Nimonic-75 alloy using principal component analysis integrated with Taguchi method. *Journal of King Saud University-Engineering Sciences*, vol. 30, no. 3, p. 250-258, **DOI:10.1016/j.jksues.2018.04.001**.

[21] Wu, Z., Xing, Y., Huang, P., Liu, L. (2017). Tribological properties of dimple-textured titanium alloys under dry sliding contact. *Surface and Coatings Technology*, vol. 309, p. 21-28, **DOI:10.1016/j.surfcoat.2016.11.045**.

[22] Thanigaivelan, R., Arunachalam, R.M., Jerald, J., Niranjan, T. (2011). Applications of Taguchi technique with fuzzy logic to optimise an electrochemical micromachining process. *International Journal of Experimental Design and Process Optimisation*, vol. 2, no. 4, p. 283-298, **DOI:10.1504/IJEDPO.2011.043565**.

[23] Pradeep Kumar, G., Thanigaivelan, R., Arunachalam, R.M., Paramasivam, P. (2014). Experimental investigation of edm processing parameters on machining Al6063-12% sic-5% gr using response surface methodology. *High Temperature Material Processes: An International Quarterly of High-Technology Plasma Processes*, vol. 18, no. 1-2, p. 27-43, **DOI:10.1615/HighTempMatProc.2015014659**.

[24] Zhao, W., Wang, W., Jiang, G., Li, B.Q., Mei, X. (2015). Ablation and morphological evolution of micro-holes in stainless steel with picosecond laser pulses. *The International Journal of Advanced Manufacturing Technology*, vol. 80, no. 9, p. 1713-1720, **DOI:10.1007/s00170-015-7145-8**.

Strojniški vestnik - Journal of Mechanical Engineering 67(2021)10, 534-544
DOI:10.5545/sv-jme.2021.7272
Original Scientific Paper
Received for review: 2021-05-29
Received revised form: 2021-09-29
Accepted for publication: 2021-10-01

Mechanical Characterization and Structural Attributes of Biohybrid Composites Derived Using Hemp, Bamboo, and Jute Fibres: an Alternative Approach in the Application of Natural Fibres in Automobile Parts

Rajmohan Bose – Arunachalam Kandavel
MIT Campus Anna University, India

In the present work, three natural fibres, namely jute, hemp and bamboo have been hybridized with seashell powder and polypropylene resin as biohybrid composites. Nine samples are considered for this study with various weight propositions of bamboo, hemp, and jute. The mechanical characteristics, such as the flexural, impact, and tensile strength of nine samples, are compared, and the Sample 9 shows very good results; the obtained flexural, tensile strength and impact energy of Sample 9 are 239.36 MPa, 47.84 MPa, and 18.33 J, respectively. The main reason for this is the presence of jute material and layering pattern; Sample 9 contains 60 % Jute, 20 % hemp, and 20 % bamboo; the percentage of jute is high compared to the other eight samples. Furthermore, morphological analysis and thermogravimetric analysis (TGA) have been carried out with Sample 9. While comparing the properties of with the existing dashboard material properties, they show more desirable values and thus, the compositions of Sample 9 material can be used for various vehicle parts. When the experimental results are compared with the finite element analysis (FEA) results, the experimental results match with the FEA results, and few variations are noticed.
Keywords: thermogravimetric analysis, morphological analysis, jute, hemp, bamboo, finite element analysis

Highlights

- *This Investigation has considered three natural fibres (hemp, bamboo, and jute) with seashell powder and polypropylene resin, and they are hybridized in biohybrid composites.*
- *Experimentally, its potential is investigated through various mechanical characteristics, such as tensile, flexural strength, and impact energy.*
- *The authors have also validated the reported results with FEA modelling.*

0 INTRODUCTION

Naturally, derived cellulose fibres have gained significant attention due to their diverse applications in the engineering disciplines, and especially in end uses, such building materials and structural parts of motor vehicles for which there is a need for a lightweight material. Low cost followed by lesser tool wear at the time of processing are some of the major advantages seen during the implementation of plant fibres, as well as the ease of recycling an environmentally viable and friendly material. Over 1000 different plant species bearing cellulose-based usable fibres exist [1]. There is a growing consciousness of environmental sustainability and a profound interest among researchers in using natural fibres (NF) like bamboo, pineapple leaf, hemp, kenaf, banana, jute, coir, sisal, oil palm, and flax as green reinforcements of polymer composites for minimizing the overall implementation and of synthetic fibres, such as Kevlar, glass, and carbon [2].

The recent decade has seen the rise of the utilization of NF as a reinforcement concerning composite materials for replacing glass fibres. The automotive industry remains one of the promising and prominent users of naturally derived composites in their fabrication and interior applications, especially in the making of trunk liners and door panels for vehicles [3]. It is estimated that the increase in the utilization of NF as an alternative for several automotive components might reach about 54 %, since European and US car manufacturers have implemented Environmental Directives. Several US-based automotive have embraced using natural materials: about 1.5 million vehicles are already using vegetable fibres such as jute, hemp and kenaf as reinforcement of thermoplastic and thermosetting polymers [4]. Under this particular aspect, automobile parts like bumpers, panels, and other related automotive components are produced using fibres or with other forms of bio-thermoplastic as well as hybrid composites, which are already in use [5]. Composite materials involve a combination of two or even more differently derived materials for their effective reinforcement in industrial application. They are broadly used in many major industries, including automotive, aerospace, marine and electric, which require light weight-to-strength ratios [6].

*Corr. Author's Address: MIT Campus Anna University, India, rajmohanbose1990@gmail.com

Bamboo (Bambusoideae) is a group of gigantic grass plants. It is estimated that there are about 2000 species of bamboo around the world [7]. There is a steady rise in the marketing of bamboo-based products as well as their manufacturing has increased rapidly. This is especially attributed due to its effective application from being an unwanted bamboo particulate which is concentrated to develop micro-bamboo filler derived polymer composite; this happens to serve as a better opportunity in replacing it effectively as an NF for enhancing materials' property [8].

Furthermore, the plant is well-known for its excellent mechanical properties (MP) based on comparative mass and the distinct attributes of its unique physical structure [9]. The developed brake pads using seashell powder gave a better friction coefficient as the optimal value (0.48) falls within the class G (0.45 to 0.55) type of brake pads recommended for use by the Society of Automobile Engineers (SAE) [10]. It was found that poor binding with epoxy/natural filler, agglomeration issue under a higher filler weight %, and also susceptible to increased moisture content [11]. Several types of research studies have analysed its effect on the recycling of polypropylene (PP), which is known as the most widely used matrix in terms of composite materials reinforced alongside natural fibres [12]. For instance, a study that concentrated on both the mechanical and rheological properties has shown that pure PP remains to be practically observed as unaffected while performing the first four recycling cycles. Also chemical treatments involving alkali, silane, and acid-based treatments have appeared to be the most utilized approaches in developing a fibre and natural filler [13].

Jute, which remains in the top the tables in terms of its usage as vegetable fibre, is grown in tropical countries like India, China, Bangladesh, Thailand, and Nepal. These countries collectively contribute 95% of global jute fibre production [14]. As the majority of studies focus on jute fibre/non-degradable polymer composites, research about jute/biodegradable polymer-based composites has been found to be quite limited [15]. For the hemp plant, the fibres contained within the tissues facilitate holding the plant in an erect position. Hence, the fibres exhibit strength as well as stiffness. Both of these factors make hemp quite suitable for the reinforcement of composite-based materials [16].

In this study, physical, chemical and MP of NF's properties observed [17] and [18]. The chemical, physical and MP of polymers properties observed [19]. Fibre type is commonly categorized based on its origin: plant, animal, or mineral. From these types, plant-based fibres are the most suitable to be used in composites with structural requirements. Furthermore, plant fibres can suitably be grown in many countries and can be harvested within short periods. The focus, for example, in Europe, has been on flax, whereas hemp, jute, ramie, kenaf, and sisal have been of greater interest in Asia. Generally, higher performance is achieved with the varieties of higher cellulose content and with cellulose microfibrils aligned more in the fibre direction. It tends to occur in blast fibres (e.g., flax, hemp, kenaf, jute, and ramie) that have higher structural requirements in providing support for the plant's stalk [20]. Researchers [21] have found that with the addition of chemically treated wood flour in PP (polypropylene), sustained improvement is obtained in composite's tensile strength.

The research study evaluates the overall environmental impact of alkaline-treated bamboo, jute, and hemp fibre on a PP matrix. Flexural, impact, and tensile characteristics, scanning electron microscope (SEM), Energy Dispersive X-ray (EDX), TGA and FEA analyses have been investigated to develop verified weight proportions and layering patterns of bio hybrid composites for applications suitable for automobile parts.

1 EXPERIMENTAL PART

1.1 Fabrication of Specimen

Compression moulding is a form of moulding that requires preheated moulding material that is initially mounted on an open, heated, mould -etched cavity. At the Indian Institute of Technology Madras, compression moulding is used to create these composites. The composites are made up of NF and PP in the ratio of 1:4. The weight composition of the composite produced are 100 grams of fibre, 400 grams of PP resin, and 5 grams of seashell powder. The conditions involved in fabricating the specimen are: time: 4 hours, stirring time: 45 minutes, pressure: 25 bar, and temperature: 75 ºC. The dimensions of the composite shape are 300 mm × 300 mm × 4 mm (length × width × thickness). The bio hybrid composites are fabricated into nine different weight proportions and layering patterns. The weight composition is illustrated in Table 1. Four layers of bio-hybrid composite are fabricated at a defined orientation (0˚ & 90˚).

These three fibres (hemp, jute, and bamboo) was purchased from Go Green Products, Chennai. PP resin was purchased from Vasavibala resins (P) Ltd,

Chennai. Seashells are collected from the seashore and powdered using a ball-milling machine.

Table 1. *Sample weight distribution*

Sample	Hemp [%]	Bamboo [%]	Jute [%]
Sample 1	40	30	30
Sample 2	30	40	30
Sample 3	30	30	40
Sample 4	50	25	25
Sample 5	25	50	25
Sample 6	25	25	50
Sample 7	60	20	20
Sample 8	20	60	20
Sample 9	20	20	60

1.2 Chemical Treatment

The purpose of chemically treating the NF is primarily the removal of lignin, waxy substances, pectin, and natural oils that coat the external portion of the fibrous cell wall. This initial treatment exposes fibrils, thereby giving a rough topographical surface for the fibre. Bleaching is carried out using sodium hydroxide (NaOH) as it is commonly used chemical in cleaning/ bleaching plant fibres' efficiently. Also, the chemical modifies the finer structural characteristics in native cellulose I/II via alkalization [22]. Fibre treatments involving silane and alkali require treatment for increasing adhesion between hydrophilic groups endowed in NF with that of the hydrophobic epoxy matrix [23]. Interfacial bonding in the case of the fibre and matrix is found to have improved effectively via chemical treatment using a coupling agent [24]. In this study, alkaline treatment has been done with 5 % NaOH; the material is dipped in it for 72 hrs and dried [25] and [26].

1.3 Mechanical Characterization

A universal testing machine (Instron 5567, Shakopee) has been employed to perform mechanical attributes, and elongation is performed under the breakage of composites under different loadings. Composite samples are cut into a rectangular shape of 246 mm × 29 mm × 4 mm with a band saw machine for tensile testing, which has been carried out as per ASTM D3039 standard involving cross-head speed 5 mm/ min with gauge length spanning 50 mm. Data on loading, displacement, and strains are acquired. The impact in terms of strengths from derived composites under varied loading are estimated using the FIT-300-D machine. The samples are then cut into a rectangular shape of 64 mm × 12.7 mm × 4 mm using a band saw. V-notched specimens were further tested as per ASTM D256. Appropriate pendulum hammers of over 10 kJ are mounted. The analysis tool involves the calibration of energy followed by accurate determination showing the exact amount in terms of impact energy [J/m] involved for the tests. The energy needed for breaking composite specimens in terms of toughness and average impact energy is determined. Flexural properties of composites are evaluated by involving bending (three-point) using a universal testing machine, as per ASTM D790 standards.

Furthermore, they are cut as per the standard dimension of 250 mm × 25 mm × 4 mm. The machine is operated at a cross-head speed of 1 mm/min with a support span-to-depth ratio involving 16:1. The existing material mechanical properties (tensile, flexural and impact) were obtained as per the same testing procedure followed by the experimentally tested mechanical properties of the nine samples.

1.4 Scanning Electron Microscopy (SEM)

SEM is facilitated for observing the morphological attributes of the experimental composites comprising of montmorillonite (MMT) based inorganic load. This form of analysis is essentially used for studying the surface characteristics of the composites via constructing three-dimensional images under high resolution with excellent depth in the field and no loss in image sharpness. The morphological features of the fractured sample from the composites are determined using QUANTA 200F – SAIF - IIT Madras.

1.5 Energy Dispersive X-ray (EDX)

EDX is an X-ray approach used to determine the elemental composition of materials. A QUANTA 200F – SAIF-IIT Madras SEM instrument has been used to perform this elemental analysis.

1.6 Thermogravimetric Analysis (TGA)

The TGA of polymers serves as a very effective technique for assessing thermal stability. Similar approaches employed are DGC, DTA, and derivatographic analysis [27] for a comparative study, especially for assessing the thermal behaviour of related categories of polymer samples, with each of its samples analysed via one or more of such methods involving identical experimental attributes. For instance, TGA is performed in air with an oxygen-free nitrogen composition. The process is

carried out under varied thermal conditions/different heating rates. It is imperative to assess the polymeric samples under different thermal analyses under a given method based on numerous aspects [28]. The amount, as well as material particle size, is examined these factors influence the nature of the thermogram. Thermogravimetric readings monitor the speed of the recorder by noting modifications in terms of weight and shape of sample containers which impact thermogravimetric outcomes. The heating rates of the sample and the ambient atmosphere during the time of analysis are assessed. The information achieved from TGA is found to be complementary to the other methods mentioned above. The study employed TGA analysis via the Universal V4.5A TA instrument in CLRI, Chennai.

1.7 Finite Element Analysis (FEA)

This work [29] has focused on numerical modelling, and verification of the experiment results is performed with the compression of axially compressed honeycomb cores. The explicit standard simulation has offered good results for the first phase of the test, and the force calculated by the simulation is very close to the experimental tests.

The formula used for density calculation is:

$$Density = \rho_{(A\times\%A)} + \rho_{(F)(B\times\%B)} + \rho_{(F)(C\times\%C)} + \rho_{(F)(D\times\%D)}. \quad (1)$$

The density calculation is carried out using the fibre weight percentage and resin weight percentage.

In this formula, ρ stands for density, A refers to matrix material density. B, C and D denote the densities of each of the fibres.

Semi-empirical models have been successfully used to describe the characterization of composite materials. Rule-of-mixture models are commonly used to predict Young's modulus [30].

$$E_C = E_F E_M / (E_F V_M + E_M V_F). \quad (2)$$

In this equation, E_C, E_F, and E_M are Young's modulus for the composites, matrix, and fibres respectively; V_F and V_M are the volume fractions of the fibres and matrix, respectively.

2 RESULTS AND DISCUSSION

The 5 % sodium hydroxide alkaline treatment of NF has improved the biohybrid specimen's mechanical characterization, although the aforementioned treatment wipes out the dust and other impurities of the fibre. It is more convenient to obtain interfacial adhesion bonding among reinforcement and matrix. The reinforcement and matrix parameters have greatly influenced the mechanical attributes and performed an influential role in fabricating the biohybrid specimens. Furthermore, the seashell powder is acknowledged because it contributes to the improvement of the biohybrid specimen's mechanical properties and also helps to minimize the voids and cracks in the specimen.

The experimentally tested mechanical properties of the nine samples and the existing material are given in Table 2. The properties of the existing material are compared with the samples obtained with high values [31].

Table 2. *Mechanical strength of composite samples*

Sample	Tensile strength [MPa]	Flexural strength [MPa]	Impact energy [J]
Sample 1	31	167.99	13.16
Sample 2	28.79	107.14	14.16
Sample 3	28.53	150.94	11.33
Sample 4	24.53	94.05	21
Sample 5	33.20	132.42	15.16
Sample 6	40.59	184.23	16.83
Sample 7	34.30	132.73	14.83
Sample 8	35.82	178.02	18.33
Sample 9	47.84	239.36	18.33
Existing material	18.1	68.2	3.6

2.1 Tensile Strength

The results assessments of various mechanical characteristics of fabricated composite (jute, hemp, bamboo) with regard to tensile strength are summarized in Table 2 for better comparison. Significantly, it is revealed that the joint exists with dissimilarities in aspect ratio, and the varied material fibres affect the inborn property; thus, mechanical characteristics increase/decrease, when applied individually. It is observed that the tensile strength of Sample 9 appears high compared to other sample data. Stress rises linearly by concerning the rises in strain of composites. The least tensile strength of 24.54 MPa is obtained in Sample 4 which has 50 % hemp, 25 % bamboo, and 25 % jute, whereas Sample 9 has 20 % hemp, 20 % bamboo, and 60 % jute. This shows the highest value of 47.85 MPa. Thus, by concerning the tensile strength, the maximum value is obtained in the combination in which the presence of jute is the

highest as well as the layering pattern of the biohybrid composite.

2.2 Flexural Strength

The flexural resistance observed from the composites is shown in Table 2. The flexural strengths for samples establishes from the linear portion of the curve via defining load and equivalent displacement, which is also indicated in Sample 9 to exhibit the highest value compared to other composite samples; this sample has the fibre content of 20 % hemp, 20 % bamboo, and 60 % jute. Sample 4 has a fibre content of 50 % hemp, 25 % bamboo and, 25 % jute. Sample 4 has the lowest value, at 94.05 MPa, which is not even half of the maximum value obtained.

2.3 Impact Energy

The test is achieved by assessing the impact of capability under different composites. Impact energy aid in determining the material's toughness. It is regarded as one of the critical factors measuring the ability to absorb energy while the sample undergoes plastic deformation (PD). Brittle materials, for instance, exhibit low toughness as an effect of a smaller degree of undergoing PD. In the case of NF, it shows greater fibre/matrix strength as it does not facilitate energy being absorbed in interfaces. This loss of energy is established via the Charpy impact test machine. The absorbed energy under each specimen when impacted by heavy blow, and the resultant data are summarized in Table 2. Resin toughness compared to that of fibre strength as well as stiffness observed is regarded as a major parameter that influences composite's impact-resistant properties. It is seen that Sample 4 has exhibited high impact energy upon comparison with other composites; the energy absorbed is 21 J. Sample 4, which shows a high impact value, has the fibre content of 50 % hemp, 25 % bamboo, and 25 % jute. Sample 9 has the second-highest value at 18.83 J.

2.4 Comparison of Composite Material with Existing Material

The highest tensile, flexural, and impact values obtained from the experiment are compared with the existing material for car dashboards are shown in Table 2. The major proposal of this study is to suggest a composite material made of NF for the manufacturing of various automobile interior parts. Thus, the car dashboard is selected as a proposal, and the properties are compared. The tensile strength of the existing material is 18.1 MPa, but the highest value obtained in Sample 9 is 47.85 MPa, which is 29.75 MPa high. Thus, the proposed composite possesses a value 2.6 times more than the existing value. The flexural strength of the existing materials is 68.2 MPa, but the highest value obtained in Sample 9 is 239.36 MPa, which is 171.16 MPa high. Thus, the proposed composite possesses a value which is 3.5 times more than the existing value. The impact energy of the existing material is 3.6 J, but the highest value obtained in Sample 4 is 21 J, which is 17.4 J higher than the existing material. Thus, the Sample 4 possesses a value which is of 5.83 times higher than the existing value.

2.5 Morphological Analysis via SEM

Morphological analysis has been performed via SEM. Sample 9 has exhibited better MP, which is evident from the observed samples selected for the morphological analysis. The prediction of macroscopic behaviour of composite materials is of fundamental and practical importance, as new composites are being developed continually for the automotive as well as aerospace industries, electronic packaging, thermal insulation, and many other applications [32]. There is an improvement in the interfacial adhesion between the matrix and coating; hence, the mechanical properties are attributes of the high strength cellulosic composite. SEM observations have allowed highlighting the different morphology of the surfaces [33]. A detailed analysis of the microstructure was carried out; it highlighted the predominant role of fibre orientation in the MP of composites [34]. It was found that chemical treatment results in composites with better MP's compared to the composites without any treatments [35].

Fig. 1 displays a micrograph of a fractured specimen of tensile, flexural, and impact test of Sample 9, which shows improved MP related to other samples. Alkaline treatment of the composites aids in better interfacial bonding, which in turn improves the mechanical strength. Pull-out phenomena of the fibres are presented in the image. The SEM images reveal some voids due to the fibre pull-out, and more breakages of fibres. SEM images Fig. 1b to d indicates better fibre-matrix interaction between the fibres and the polymer matrix. Fig. 1a depicts the SEM image of the parent material; it clearly shows the fibre direction. It also demonstrates a very good bonding between the resins and fibre, thus indicating a better mechanical bonding with the fibre-polymer matrix. Fig. 1b

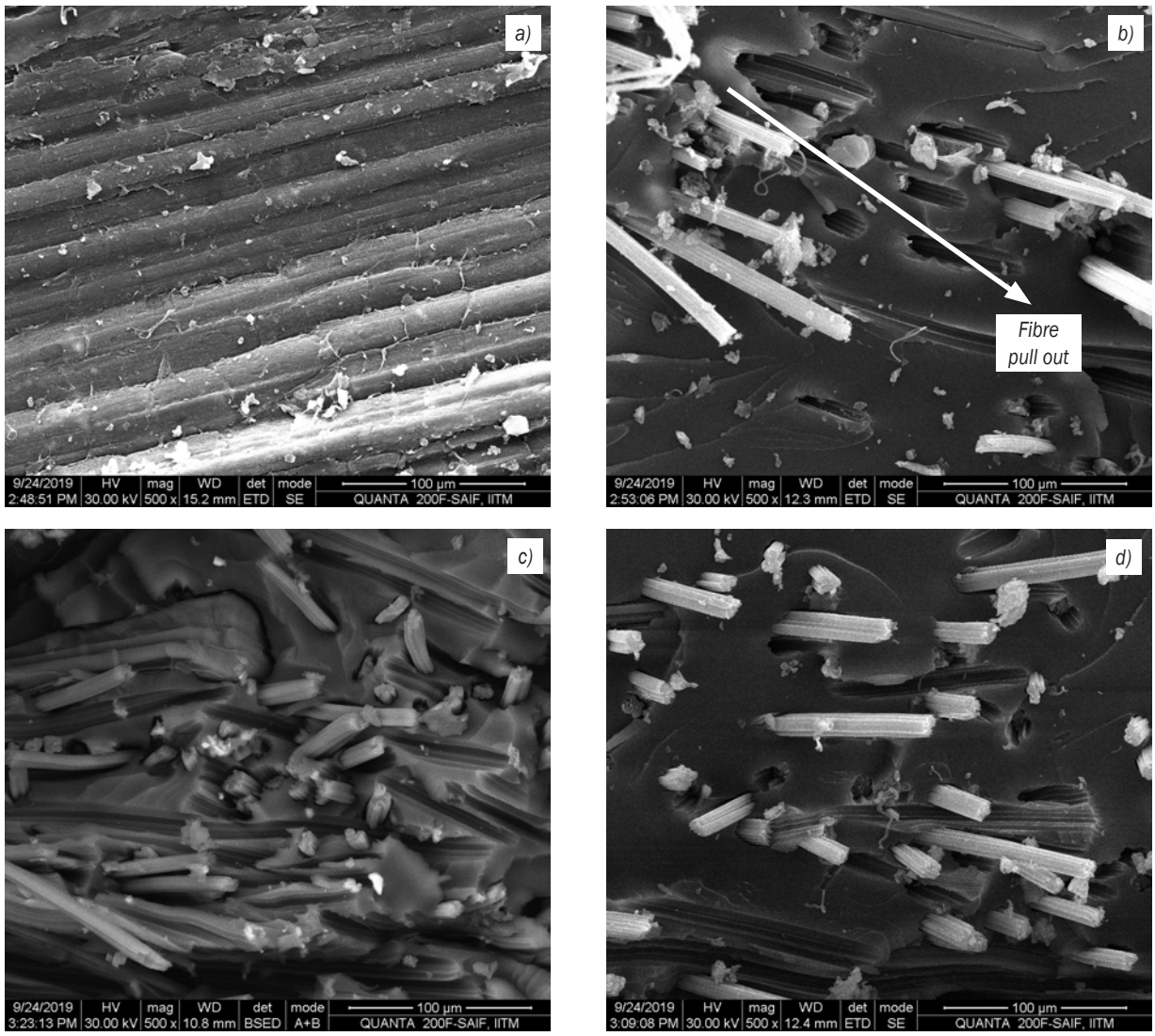

Fig. 1. *SEM image of a) Specimen 9 top surface, and b) fractured Specimen 9 of tensile test, c) fractured Specimen 9 of impact test, and d) fractured Specimen 9 of flexural test*

delineates the SEM image of a fractured specimen during a tensile test where the fibre pull out position is visible in the image. Fig. 1c illustrates the SEM image of a fractured specimen of impact test, and Fig. 1d shows the SEM image of the fractured specimen of the flexural test. SEM images show that there are no voids, blowholes, or cracks on the top surface and in the inner layers. These figures reveal that the mixture of the resin and fibre is uniform in all the biohybrid composites.

2.6 Energy Dispersive X-ray (EDX)

Fig. 2a represents the distribution of fibres and particulate reinforcement from observed composite samples; Fig. 2b depicts the energy dispersive X-ray (EDX) spectroscopy of composites material. From the observed EDX analysis, it can be seen that the particles are primarily composed of component mixtures, such as Ca, Cl, and C. There are numerous trace elements, including K, Ca, and Si, present in the samples.

The EDX comprises a unique class of fillers that are effectively applicable for polymer matrix as a result of their fine dispersion, inertness, homogeneity, chemical stability, and low water absorption. The presence of Ca was reported as high, as a result of seashell powdered composite elements deposited in composite samples. Fig. 1a shows that the seashell powder is finely distributed throughout the sample

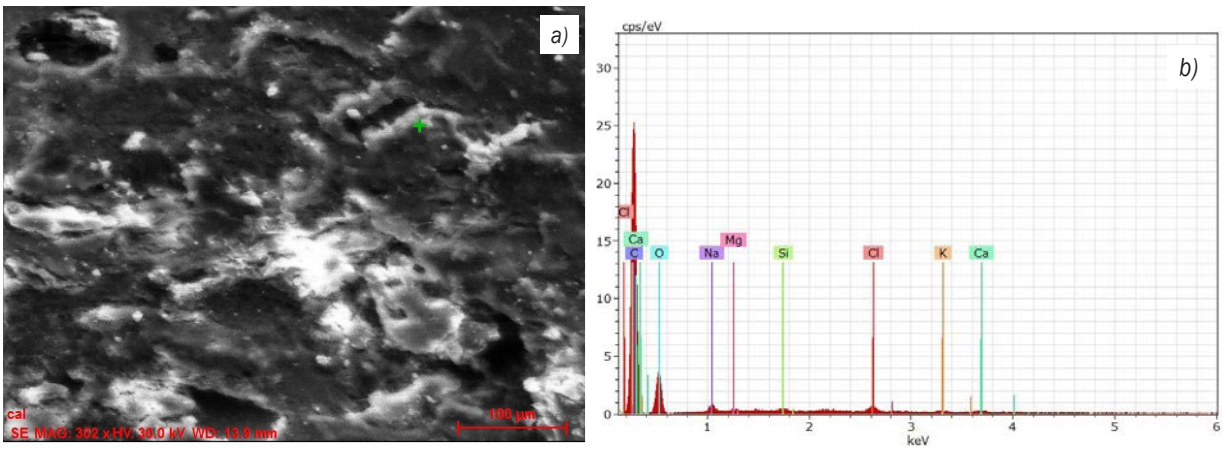

Fig. 2. *Composite material Sample 9, a) EDX image, and b) EDX graph*

SEM, and it helps to increase the mechanical strength of the composite material.

2.7 Thermogravimetric Analysis (TGA)

A special TGA technique has been developed for quantifying the composite mass percentage. TGA curves derived from additives, fibres, and polypropylene are assigned for a composite fraction.

The heating rate is fixed for thermal degradation of single components via using dynamic as well as isothermal segments.

Sample 9 is thermogravimetrically analysed with the existing material to find the percentage of weight loss concerning increasing temperature. The three major weight loss regions are represented in Fig. 3. Fig. 3a displays the TGA results of Sample 9, and Fig. 3b shows the TGA of the existing material. Table 3 gives the peak temperature at various mass loss percentages and the average temperature is calculated by the obtained values. Sample 9 can withstand even at 451 °C, with 50 % of weight loss and the working temperature in real-time is much less than the calculated temperature. The existing material shows an average temperature of 536.3 °C, and Sample 9 shows an average temperature of 430.6 °C, which is 19.4 % less than that of the existing material. The major reason for this reduction is that the composite is made of NFs.

2.8 Comparison between the Experimental results and FEA

As per the ASTM standard tensile, flexural and impact test specimen size, the surface geometry is created using Creo. The created geometry is imported into the ANSYS workbench, and solid jet 4 node 285 element has been chosen for composite laminates. The properties of isotropic fibre-reinforced composites are

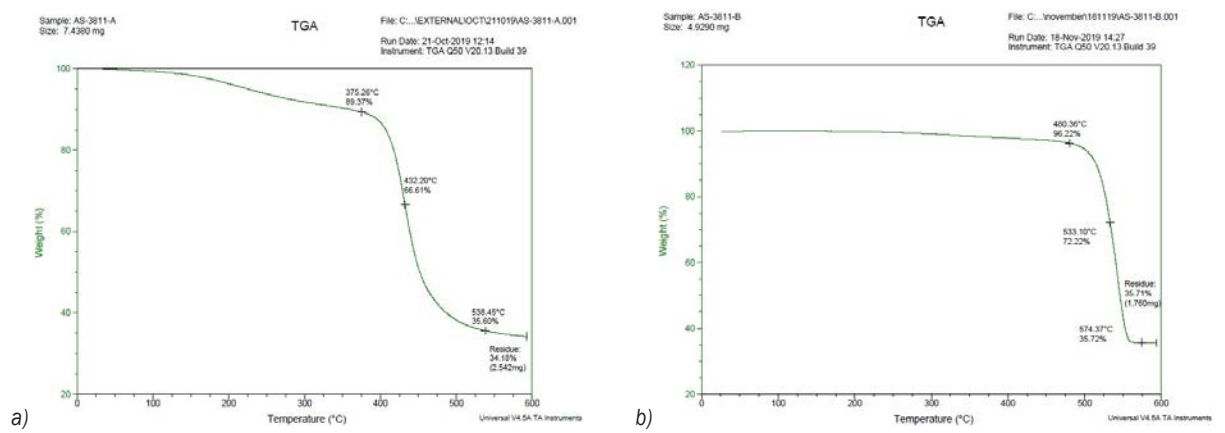

Fig. 3. *TGA; a) Sample 9, and b) existing material*

Table 3. *The peak temperature at various mass loss percentages*

	Peak temperature [˚C] and (weight [g])						Mean temperature [˚C]
Wt. loss [%]	10	20	30	40	50	60	
Sample 9	360.6 (6.69)	417.3 (5.95)	429.0 (5.2)	437.6 (4.46)	452.0 (3.71)	487.0 (2.975)	430.6
Existing	517.0 (4.361)	527.0 (3.94)	534.6 (3.45)	540.7 (2.95)	546.0 (2.46)	552.7 (1)	536.3

Table 4. *Boundary conditions*

Properties	Composite density [g/cm^3]	Young's modulus [N/mm^2]	Poisson's ratio	Tensile strength [MPa]	Flexural strength [MPa]	Impact energy [J]
Sample 9	0.99	7.57×10^3	0.3	47.84	239.36	21
Existing car dash board	1.03	7.27×10^3	0.3	18.1	68.2	3.6

theoretically calculated for Sample 9 and the existing material. They are given in Table 4.

2.8.1 Tensile Strength Analysis

Fig. 4 and Table 5 show tensile strength analysis of the existing material and Sample 9.

Table 5. *Tensile strength comparison*

Test conducted	Tensile strength [MPa]	
	Existing material	Sample 9
Experimental work result values	18.1	47.84
FEA work result values	18.57	44.73
Variation	0.47	3.11
Variation %	D 2.56	I 6.72

The experimental value and the FEA values are within 5 % of variation. As mentioned earlier, Sample 9 exhibits tensile strength, which is 64.1 % higher than the existing material. Experimental values match with the FEA results. FEA results of Sample 9 have the tensile strength of 44.73 MPa, and the experimental result is 47.84 MPa, which is a 6.72 % increase from the FEA result. The FEA results of the existing material show the tensile strength of 18.57 MPa and the experimental result is 18.1 MPa, which is a 2.56 % decrease from the FEA result. In Tables 5, 6, and 7. D stands for decrease and I for increase.

2.8.2 Flexural Strength Analysis

Fig. 5 and Table 6 show the flexural strength analysis of the existing material and Sample 9.

Table 6. *Flexural strength comparison*

Test conducted	Flexural strength [MPa]	
	Existing material	Sample 9
Experimental work result values	68.2	239.36
FEA work result values	71.62	263.38
Variation	3.42	24.02
Variation %	D 4.89	D 9.55

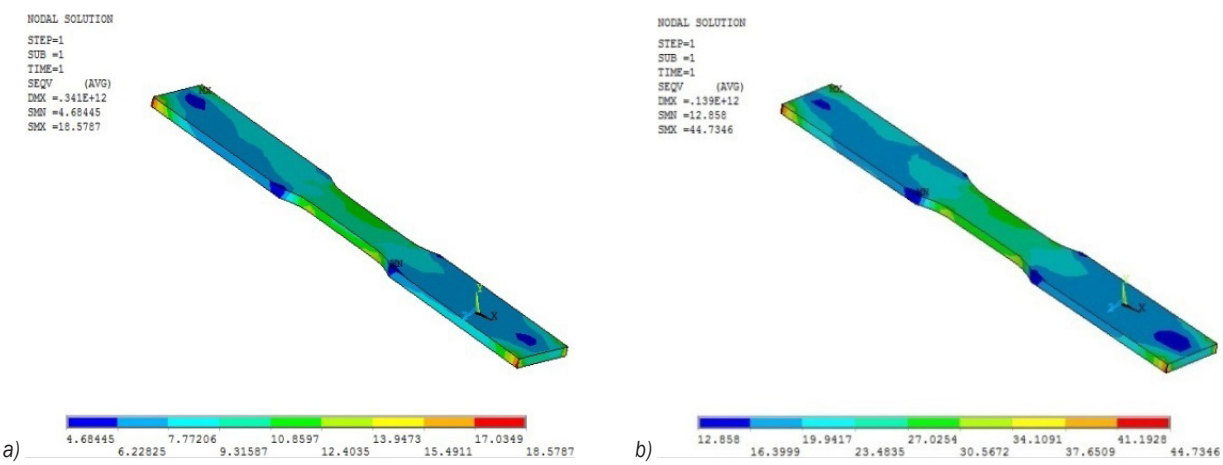

Fig. 4. *Tensile strength analysis, a) existing material, b) Sample 9*

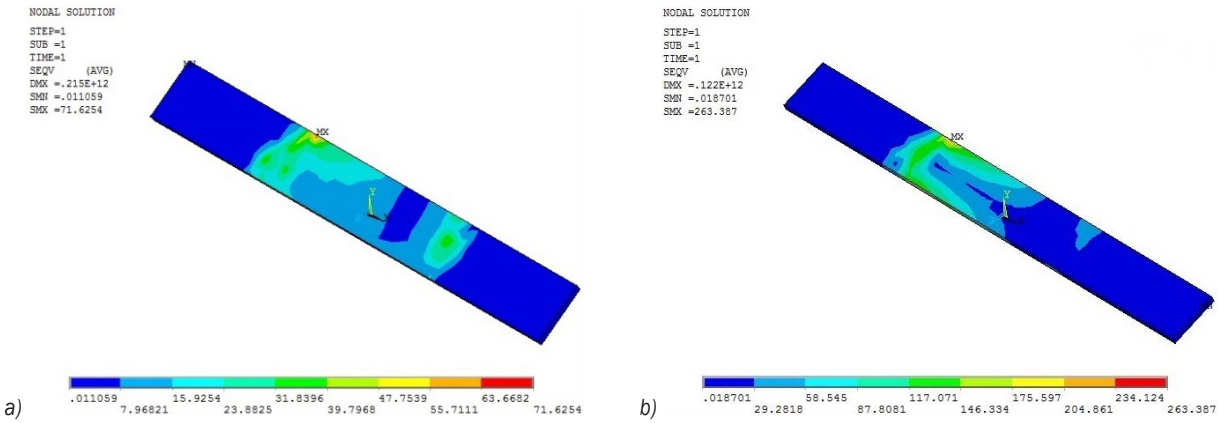

Fig. 5. *Flexural strength analysis, a) existing material, b) Sample 9*

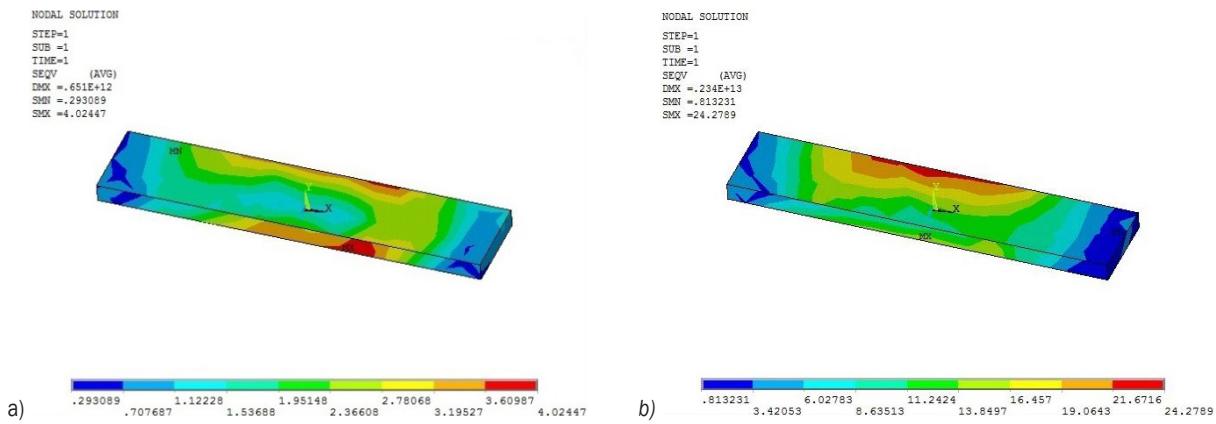

Fig. 6. *Impact energy; a) existing material, b) Sample 4*

When the experimental values and FEA values are compared, for the existing material, the experimental value of the existing material is 4.89 % less than the FEA results, where as in Sample 9, there is a decrease of 9.55 % compared to the FEA results. As mentioned earlier, Sample 9 exhibits flexural strength that is 150.96 % higher than the existing sample material.

2.8.3 Impact Energy Analysis

Fig. 6 and Table 7 shows the impact energy analysis of the existing material and Sample 4.

Table 7. *Impact energy comparison*

Test conducted	Impact energy [J]	
	Existing material	Sample 4
Experimental work result values	3.6	21
FEA work result values	4.02	24.27
Variation	0.42	3.27
Variation %	D 11.02	D 14.44

The experimental value and the FEA values are compared. It is clear that there is a decrease of 11.02 % in the existing material and 14.44 % in Sample 4. As mentioned, Sample 4 exhibits impact energy that is 5.83 times higher than that of the existing material. Experimental values match the FEA results. The FEA results of sample 4 show the impact energy of 24.27 J, and its experimental result is 21 MPa, whereas the FEA result of the existing material is 4.02 J, and the experimental result is 3.6 J.

3 CONCLUSIONS

The composite samples consist of jute, bamboo, and hemp, and they are fabricated. Hybrid composites are subjected to tensile, impact, and flexural testing. Results obtained are compared with the existing material. All the composites exhibit a high value compared to the existing material. Among the nine samples, Sample 9 (20 % hemp, 20 % bamboo, and 60 % jute) provides the highest values. Thus, for further

morphological analysis, TGA and FEA analyses are performed with Sample 9, and the results are compared with the existing material results. Consequently, the Sample 9 composite will be the best replacement for the existing material and the same can be utilized for the manufacturing of various vehicle parts.

Based on the results, the major conclusions identified are:

- The tensile strength of Sample 9 composite at 20 % hemp, 20 % bamboo, and 60 % jute wt.% fibre, compared to the existing material, is increased by 64.1 % (47.84 MPa) more compared to the existing material (18.1 MPa). These values are high at 29.74 MPa for Sample 9. The unique property of this sample is the presence of high wt.% of jute.
- The flexural strength of Sample 9 is 239.36 MPa, which is 150.96 % higher than that of the existing material (68.2 MPa).
- The impact energy of Sample 9 is five times higher than that of the existing material, and the value for sample 9 is 18.33 J, whereas it is 3.6 J for the existing material. Thus, it can be concluded that the material can withstand sudden impact without any deformation. This property is essential for the materials of automobile parts.
- Morphological analysis has been carried out to better understand the structure formation and interfacial bonding between the materials.
- TGA results show that the existing material has an average temperature of 536.3 °C, and Sample 9 has an average temperature of 430.6 °C, which is 19.4 % less than the existing material. The major reason for this reduction is that the composite is made of NFs. The working temperature of the interior and exterior parts of the automobiles is below 460.6 °C and as a result, the material can be used to manufacture automobile parts.
- The FEA results are consistent with the experimental results which show that FEA is the correct tool for testing and evaluating the mechanical behaviour of hybrid structures.
- The results indicate the possibilities of using composites made from NF, such as jute, hemp, and bamboo, as raw materials to produce various automobile parts, which can also be cost-effective and better than the existing material.

4 REFERENCES

[1] Robson, J., Hague, J., Newman, G., Jeronimidis, G., Ansell. MP. (1993). *Survey of natural materials for use in structural composites as reinforcement and matrices. Report to DTI LINK Structural Composites Committee*. Report No. EC/431/92, University of Wales, Cardiff.

[2] Monteiro, S.N., Calado, V., Rodriguez, R.J.S., Margem, F.M. (2012). Thermogravimetric stability of polymer composites reinforced with less common lignocellulosic fibers - an overview. *Journal of Materials Research and Technology*, vol. 1, no. 2, p. 117-126, **DOI:10.1016/S2238-7854(12)70021-2**.

[3] Suddell, BC., Evans, WJ., Isaac, DH., Crosky, A. (2002) A Survey into the Application of Natural Fiber Composites in the Automobile Industry. *Fourth International Symposium on Natural Polymers and Composites*, Sao Pedro, p. 455-461.

[4] Faruk, O. (2019). Cars from Jute and Other Bio-Fibers, from, *http://biggani.com/files_of_biggani/mashiur/interview/omar_faruk.pdf*, accessed on 2019-09-14.

[5] Netravali, A.N., Chabba, S. (2003). Composites get greener. *Materials Today*, vol. 6, no. 4, p. 22-29, **DOI:10.1016/S1369-7021(03)00427-9**.

[6] Bingol, M., Cavdar, K. (2018). New investigations on higher mechanical properties of woven glass fiber reinforced SMC composites. *Indian Journal of Engineering and Material Science*, vol. 25, no. 4, p. 315-320, **nopr.niscair.res.in/handle/123456789/45263**.

[7] Zhang, Y.C., Dai, K., Tang, J.H., Ji, X., Li, Z.M. (2010). Anisotropically conductive polymer composites with a selective distribution of carbon black in an in situ microfibrillar reinforced blend. *Materials Letters*, vol. 64, no. 13, p. 1430-1432, **DOI:10.1016/j.matlet.2010.03.041**.

[8] Li, Z.H., Kobayashi, M. (2004). Plantation future of bamboo in China. *Journal of Forestry Research*, vol. 15, p. 233-242, **DOI:10.1007/BF02911032**.

[9] Tan, T., Rahbar, N., Allameh, S.M., Kwofie, S., Dissmore, D., Ghavami, K., Soboyejo, W.O. (2011). Mechanical properties of functionally graded hierarchical bamboo structures. *Acta Biomaterialia*, vol. 7, no. 10, p. 3796-3803, **DOI:10.1016/j.actbio.2011.06.008**.

[10] Abutu, J., Lawal, S.A., Ndaliman, M.B., Araga, R.A.L., Adedipe, O., Choudhury, I.A. (2018). Effects of process parameters on the properties of brake pad developed from seashell as reinforcement material using grey relational analysis. *Engineering Science and Technology,an International Journal*, vol. 21, no. 4, p. 787-797, **DOI:10.1016/j.jestch.2018.05.014**.

[11] Gouda, K., Bhowmik, S., Das, B. (2020). Thermomechanical behavior of graphene nanoplatelets and bamboo micro filler incorporated epoxy hybrid composites. *Materials Research Express*, vol. 7, no. 1, art. ID 015328, **DOI:10.1088/2053-1591/ab67f8**.

[12] El Abbassi, F.E., Assarar, M., Ayad, R., Sabhi, H., Buet, S., Lamdouar, N. (2019). Effect of recycling cycles on the mechanical and damping properties of short alfa fibre reinforced polypropylene composite. *Journal of Renewable Materials*, vol. 7, no. 3, p. 253-267, **DOI:10.32604/jrm.2019.01759**.

[13] Li, X., Tabil, L.G., Panigrahi, S. (2007). Chemical treatments of natural fiber for use in natural fiber-reinforced composites: a review. *Journal of Polymers and the Environment*, vol. 15, p. 25-33, **DOI:10.1007/s10924-006-0042-3**.

[14] International Jute Study Group. (2005). Jute, Kenaf & Roselle Plants, from *http://www.jute.org/plant.htm*, accesed on 2019-09-26.

[15] Sakaguchi, M., Nakai, A., Hamada, H., Takeda, N. (2000). The mechanical properties of unidirectional thermoplastic composites manufacturing by a micro-braiding technique. *Composites Science and Technology*, vol. 60, no. 5, p. 717-722, **DOI:10.1016/S0266-3538(99)00175-X**.

[16] Shahzad, A. (2012). Hemp fiber and its composites-a review. *Journal of Composite Materials*, vol. 46, no. 8, p. 973-986, **DOI:10.1177/0021998311413623**.

[17] Alarifi, I.M. (2020). Structural analysis of hexagonal and solid carbon fibers composite. *Polymer Testing*, vol. 84, art. ID 106392, **DOI:10.1016/j.polymertesting.2020.106392**.

[18] Cavalcanti, D.K.K., Banea, M.D., Neto, J.S.S., Lima, R.A.A., da Silva, L.F.M., Carbas, R.J.C. (2019). Mechanical characterization of intralaminar natural fibre-reinforced hybrid composites. *Composites Part B: Engineering*, vol. 175, art. ID 107149, **DOI:10.1016/j.compositesb.2019.107149**.

[19] Kumar, N., Mireja, S., Khandelwal, V., Arun, B., Manik, G. (2017). Light weight high strength hollow glass microspheres and bamboo fiber based hybrid polypropylene composite: A strength analysis and morphological study. *Composites Part B: Engineering*, vol. 109, p. 277-285, **DOI:10.1016/j.compositesb.2016.10.052**.

[20] Pickering, K.L., Aruan Efendy, M.G., Le, T.M. (2016). A review of recent developments in natural fibre composites and their mechanical performance. *Composites Part A: Applied Science and Manufacturing*, vol. 83, p. 98-112, **DOI:10.1016/j.compositesa.2015.08.038**.

[21] Ichazo, M.N., Albano, C., Gonzalez, J., Perera, R., Candal, M.V. (2001). Polypropylene/wood flour composites treatments and properties. *Composites Structures*, vol. 54, no. 2-3. p. 207-214, **DOI:10.1016/S0263-8223(01)00089-7**.

[22] Mwaikambo, L.Y., Ansell, M.P. (2002). Chemical modification of hemp, sisal, jute and kapok fibers by alkalization. *Journal of Applied Polymer Science*, vol. 84, no. 12, p. 2222-2234, **DOI:10.1002/app.10460**.

[23] Sgriccia, N., Hawley, M.C., Misra, M. (2008). Characterization of natural fiber surfaces and natural fiber composites. *Composites Part A: Applied Science and Manufacturing*, vol. 39, no. 10, p. 1632-1637, **DOI:10.1016/j.compositesa.2008.07.007**.

[24] Venkateshwaran, N., Elaya Perumal, A., Alavudeen, A., Thiruchitrambalam, M. (2011). Mechanical and water absorption behaviour of banana/sisal reinforced hybrid composites. *Materials & Design*, vol. 32, no. 7, p. 4017-4021, **DOI:10.1016/j.matdes.2011.03.002**.

[25] Nam, T.H., Ogihara, S., Tung, N.H., Kobayashi, S. (2011). Effect of alkali treatment on interfacial and mechanical properties of coir fibre reinforced poly (butylene succinate) biodegradable composites. *Composites Part B: Engineering*, vol. 42, no. 6, p. 1648-1656, **DOI:10.1016/j.compositesb.2011.04.001**.

[26] Sepe, R., Bollino, F., Boccarusso, L., Caputo, F. (2018). Influence of chemical treatments on mechanical properties of hemp fibre reinforced composites. *Composites Part B: Engineering*, vol. 133, p. 210-217, **DOI:10.1016/j.compositesb.2017.09.030**.

[27] Cartié, D.D.R., Irving, P.E. (2002). Effect of resin and fibre properties on impact and compression after impact performance of CFRP. *Composites Part A: Applied Science and Manufacturing*, vol. 33, no. 4, p. 483-493, **DOI:10.1016/S1359-835X(01)00141-5**.

[28] Vyazovkin, S., Koga, N., Schick, C. (2018). *Handbook of Thermal Analysis and Calorimetry, Recent Advances, Techniques and Applications*. vol. 6, p. 1-842, Elsevier, Amsterdam, **DOI:10.1016/B978-0-444-64062-8.10000-2**.

[29] Mertani, B.MčB., Keskes, B., Tarfaoui, M. (2019). Numerical study on the compressive behaviour of an aluminium honeycomb core. *Materials and Technology*, vol. 53, no. 2, p. 199-206, **DOI:10.17222/mit.2018.028**.

[30] Gutiérrez, M.C., De Paoli, M.A., Felisberti, M.I. (2014). Cellulose acetate and short curaua fibers biocomposites prepared by large scale processing: Reinforcing and thermal insulating properties. *Industrial Crops & Products*, vol. 52, p. 363-372, **DOI:10.1016/j.indcrop.2013.10.054**.

[31] Arunachalam, K., Sundara Pandian, G. (2016). Modeling and analysis of clutch facing made up of biodegradable coir fibre based composite material. *Polymers &Polymer Composites*, vol. 24, no. 7, p. 463-468, **DOI:10.1177/096739111602400703**.

[32] Rao, B.R., Raju, V.R., Rao, K.M. (2015). Effect of fibre shape on transverse thermal conductivity of unidirectional composites. *Sadhana*, vol. 40, p. 503-513, **DOI:10.1007/s12046-014-0323-9**.

[33] Srinivasan, S.P., Raajarajan, L. (2017). Wear rate and surface coating optimization of coconut coir-based polymer using fuzzy logic. *Sadhana*, vol. 42, p. 281-290, **DOI:10.1007/s12046-017-0601-4**.

[34] Tanguy, M., Bourmaud, A., Beaugrand, J., Gaudry, T., Baley, C. (2018). Polypropylene reinforcement with flax or jute fibre; Influence of microstructure and constituents properties on the performance of composite. *Composites Part B: Engineering*, vol. 139, p. 64-74, **DOI:10.1016/j.compositesb.2017.11.061**.

[35] Sullins, T., Pillay, S., Komus, A., Ning, H. (2017). Hemp fiber reinforced polypropylene composites: The effects of material treatments. *Composites Part B: Engineering*, vol. 114, p. 15-22, **DOI:10.1016/j.compositesb.2017.02.001**.

Vsebina

Strojniški vestnik - Journal of Mechanical Engineering
letnik 67, (2021), številka 10
Ljubljana, oktober 2021
ISSN 0039-2480

Izhaja mesečno

Razširjeni povzetki (extended abstracts)

Strojniški vestnik - Journal of Mechanical Engineering 67(2021)10, SI 61

Prejeto v recenzijo: 2021-05-28
Prejeto popravljeno: 2021-08-17
Odobreno za objavo: 2021-08-18

Uspešnost samodejnega programiranja CAM s predlogami za strojno obdelavo v proizvodnji specialnih produkcijskih orodij

Maciej Kowalski[1,2] – Przemysław Zawadzki[1,*] – Adam Hamrol[1]
[1] Tehniška univerza v Poznanu, Fakulteta za strojništvo, Poljska
[2] MK-Tech, Poljska

Proizvodnja specialnih tehnoloških orodij je primer proizvodnje po naročilu (ang. ETO ~ engineering to order), kjer konstrukcija orodja bazira na kupčevem modelu izdelka. Proces je zamuden in pogosto tudi precej neučinkovit (pri proizvodnji skupin izdelkov), saj ga je treba izvesti v celoti za vsak model izdelka posebej, čeprav si izdelki delijo podobne proizvodne operacije. Avtorji so že razvili poseben postopek ACPUT (samodejno programiranje CAM s predlogami za obdelavo), ki zapolnjuje nekaj vrzeli v programiranju CAM in omogoča pohitritev tega procesa (vsaj v teoriji). Glavni cilj pričujoče raziskave je bil preučitev uspešnosti in učinkovitosti postopka ACPUT v primerjavi s tradicionalnim programiranjem CNC-strojev v industrijski praksi.

Uvedba metod za samodejno programiranje CAM kot je ACPUT v oddelkih za tehnologijo proizvodnih podjetij je načeloma možna, zahteva pa napredno znanje in veščine na področju CAM ter dostop do implicitnega znanja v podjetju. Priprava takih rešitev je težavna in časovno zamudna, zato je bilo treba preveriti, kdaj je avtomatizacija programiranja CAM sploh smiselna.

Opravljen je bil test za primerjavo učinkovitosti ACPUT in tradicionalnega programiranja. Sodelovalo je 10 programerjev CAM, od tega 5 strokovnjakov z več leti delovnih izkušenj in 5 začetnikov z le nekaj meseci izkušenj. V analizi so bili primerjani naslednji kazalniki:

1. potrebni čas za pripravo programa za obdelavo posameznega dela orodja T_i [min],
2. kumulativni čas za obdelavo, ki je potreben za pripravo skupine orodij T_c [min],
3. vsota stroškov programiranja in obdelave vsakega orodja C_m [EUR].

Za preizkuse je bilo izbrano orodje za montažo plastičnih cevi, ki je sestavljeno iz 50 delov in se izdeluje na CNC-rezkalnem stroju.

Preizkusi v industrijskih pogojih so pokazali, da lahko postopek ACPUT skrajša potrebni čas za razvoj programov za obdelavo, kar pozitivno vpliva na skupne stroške izdelave orodij. Uspešnost postopka ACPUT je bila preizkušena na osnovi analize potrebnega časa za pripravo CNC programov in samega časa izvajanja obdelovalnih operacij (na osnovi simulacij v paketu CAM). Čas priprave programa je neposredni (poleg kakovostnih zahtev) kazalec uspešnosti postopka ACPUT. Analiza rezultatov je pokazala, da samodejna rešitev prinaša signifikantne časovne prednosti, zlasti v primerjavi z manj izkušenimi tehnologi. Rezultati samodejne rešitve so bili celo boljši od rešitev izkušenih strokovnjakov. Poudariti pa je treba, da je uspešnost postopka ACPUT odvisna predvsem od izkušenj ljudi, ki pripravijo predloge.

V prihodnjih raziskavah bi bilo smiselno preveriti možnost ustvarjanja programov za specifične tipe CNC krmilnikov. Do tedaj pa bodo bolj neposredne raziskave osredotočene na razvoj metod za hitro oceno tehnološke podobnosti delov, ki so kandidati za pripravo predlog za obdelavo. Če so razlike med deli prevelike, priprava predlog in uporaba postopka ACPUT nista ekonomsko upravičeni – v tem primeru ima prednost tradicionalni postopek programiranja.

ACPUT je nova metoda programiranja v sistemih CAM, ki je osredotočena na avtomatizacijo ponavljajočih se opravil, zlasti v proizvodnji orodij. Metoda temelji na namensko ustvarjeni bazi znanja in na predlogah za obdelavo, ustvarjenih v sistemu CAM. Rezultati bodo zaradi praktične uporabnosti v industrijski proizvodnji uporabni tako za industrijske in procesne inženirje, kakor tudi za raziskovalce v proizvodnih podjetjih.

Ključne besede: generativni proces CAM, CNC programiranje, avtomatizacija tehnološke priprave, na znanju temelječi inženiring

*Naslov avtorja za dopisovanje: Tehniška univerza v Poznanu, Fakulteta za strojništvo, Piotrowo St. 3, 60-965 Poznan, Poljska, przemyslaw.zawadzki@put.poznan.pl

Strojniški vestnik - Journal of Mechanical Engineering 67(2021)10, SI 62

Prejeto v recenzijo: 2021-06-07
Prejeto popravljeno: 2021-08-17
Odobreno za objavo: 2021-09-09

Diagnosticiranje napak na reduktorjih RV za industrijske robote na osnovi konvolucijske nevronske mreže

Shuai Yang[1,*] – Xing Luo[2] – Chuan Li [2]

[1] Nacionalno raziskovalno središče za pametne proizvodne storitve, Tehniška in poslovna univerza v Chongqingu, Kitajska
[2] Šola za menedžment in inženiring, Tehniška in poslovna univerza v Chongqingu, Kitajska

Odpoved reduktorja kot ključne komponente mehanskega pogonskega sistema lahko povzroči veliko gospodarsko škodo, v izjemnih primerih pa tudi resne poškodbe ali smrt. V članku je opisana rešitev tega problema.

V eksperimentih je bil uporabljen senzor pospeška za zajem podatkov o obratovanju reduktorja v normalnem stanju in v stanju napake. Zbrani podatki so bili pretvorjeni iz časovne v frekvenčno domeno po metodi 2D-FFT, nato pa so bile z 2D konvolucijsko nevronsko mrežo (2D-CNN) samodejno pridobljene značilke signalov v frekvenčni domeni in opravljena je bila njihova klasifikacija s funkcijo Softmax. Opravljene so bile tudi eksperimentalne primerjave z drugimi prevladujočimi metodami za dodatno validacijo točnosti klasifikacije napak.

Predmet članka je reduktor z rotacijskim vektorjem (RV) za industrijske robote. Signali vibracij so bili pretvorjeni iz časovne v frekvenčno domeno po metodi 2D-FFT. Nevronska mreža 2D-CNN je bila uporabljena za samodejno pridobivanje značilk signala v frekvenčni domeni in klasifikacijo podatkov o napakah skladno z lastnostmi različnih signalov. Nato je bil uporabljen algoritem vzvratnega postopka učenja za posodobitev parametrov modela v 2D-CNN.

Predlagana metoda je bila uporabljena na reduktorju RV za industrijske robote, in sicer s podatki za en primer normalnega obratovanja in pet primerov stanj napak. Celotna točnost diagnosticiranja stanj je dosegla 99,67 %. Stopnja prepoznavanja napak št. 1, 3 in 4 je bila 100 %. Točnost prepoznavanja normalnega stanja je bila 99 %, točnost prepoznavanja napake št. 2 je znašala 99,3 %, napake št. 5 pa 99,67 %. Za primerjavo so bili uporabljeni modeli 1D-CNN, DBN, NN in SAE, katerih stopnja točnosti znaša 98,46 %, 58,08 %, 83,47 % in 83,05 %. Rezultati eksperimentov dokazujejo, da ima predlagani model v primerjavi z ostalimi modeli dobro točnost diagnosticiranja napak.

Predlagana metoda je bila uporabljena samo pri reduktorjih RV za industrijske robote, v prihodnje pa bodo raziskave za preverjanje univerzalnosti metode razširjene še na menjalnike za drugo mehansko opremo. Dodan bo tudi primerjalni model.

Model CNN za zaznavanje in klasifikacijo napak dosega obetavne rezultate na različnih področjih. Uporaba modela CNN pri reduktorjih RV za industrijske robote je danes še redka. V članku sta bili povezani metodi 2D-FFT in 2D-CNN za diagnosticiranje napak, predlagana metoda pa je bila uporabljena na reduktorju RV za industrijske robote.

Ključne besede: diagnosticiranje napak, konvolucijska nevronska mreža, reduktor RV

*Naslov avtorja za dopisovanje: Tehniška in poslovna univerza v Chongqingu, No .19 Xuefu Avenue, Chongqing, Kitajska, jerryyang@ctbu.edu.cn

Strojniški vestnik - Journal of Mechanical Engineering 67(2021)10, SI 63

Prejeto v recenzijo: 2021-06-24
Prejeto popravljeno: 2021-09-05
Odobreno za objavo: 2021-09-21

Analiza odziva strgalnega transporterja na odpoved verige na osnovi MBD-DEM-FEM

Zisheng Wang[1,2] – Bo Li[1,2] – Chao Liang[1,2] – Xuewen Wang[1,2,*] – Jiahao Li[1,2]

[1] Tehniška univerza v Taiyuanu, Kolidž za strojništvo in avtomobilsko tehniko, Kitajska
[2] Državni laboratorij za mehanizirano opremo za premogovnike v provinci Shanxi, Kitajska

Verige strgalnih transporterjev se pogosto kvarijo, te okvare pa je težko preučevati eksperimentalno. Večina simulacij odpovedi v objavljenih raziskavah je bila opravljena po metodah, ki le vprašljivo simulirajo resnična delovna stanja strgalnega transporterja. V članku je opisana analiza odgovora na odpoved po metodi sklopitve MBD-DEM-FEM (dinamika več teles/metoda diskretnih elementov/metoda končnih elementov).

Oblikovan je bil sklopljen model strgalnega transporterja MBD-DEM-FEM, ki je bil verificiran eksperimentalno in po točkovni metodi. Določen je bil odgovor verige in razsutega premoga v pogojih okvare in rezultati so bili delno verificirani. Končno so bile analizirane odvisnosti med faktorjem intenzitete napetosti in parametri zloma po metodi odzivnih površin.

Na podlagi testa transporta je bila uporabljena metoda odzivnih površin za optimizacijo kontaktnih parametrov premoga s silo in kotom zlaganja kot odzivnima spremenljivkama. Model DEM-MBD je bil verificiran po točkovni metodi, model verige po FEM (MKE) pa z nateznim preizkusom. Sklopljeni model je bil nato razrešen za določitev odgovora verige in premoga, rezultati pa so bili delno verificirani. Končno je bila uporabljena še metoda odzivnih površin za analizo odvisnosti med faktorjem intenzivnosti napetosti in parametri zloma.

Rezultati, ugotovitve:

(1) Sklopljeni model MBD-DEM-FEM je bil verificiran eksperimentalno in teoretično, relativna napaka pa je sprejemljiva.
(2) Ko veriga obtiči in se polomi, povzroči odklon transporterja neenakomerno obremenitev verig. Napetost in vibracije napete verige se hitro povečajo, medtem ko se napetost, hitrost in vibracije ohlapne verige zmanjšajo. Obremenitev verige ob okvari povzroči plastično deformacijo verige in zmanjša njeno utrujenostno trajnostno dobo. Obraba srednje plošče je koncentrirana na poti verige, okvare pa povzročijo novo obrabo na površini srednje plošče.
(3) Začetni kot z drugimi faktorji negativno vpliva na hitrost sprememb $K_{1\max}$, medtem ko imata globina razpok in natezna obremenitev pozitiven vpliv nanjo.

Omejitve raziskave, implikacije:

(1) Robovi in vogali kosov premoga niso bili jasno izoblikovani zaradi krajšega časa izvajanja simulacije. Z razvojem vzporednega računanja bo mogoče uporabiti modele kosov premoga z izoblikovanimi robovi in vogali za točnejše rezultate.
(2) Premog je krhek, toda drobljenje zaradi krajšega časa izvajanja simulacije ni bilo upoštevano. V prihodnjih raziskavah bo za združevanje kosov premoga mogoče uporabiti model spajanja.
(3) Veriga je upogljiva. V članku je bila izračunana le deformacija verige po izločitvi obremenitve zaradi okvare. V prihodnje bo mogoče uporabiti dinamični model upogljive verige za določitev vpliva deformacije verige na transport v realnem času.

Prispevek, novosti, vrednost:

(1) Kontaktni parametri za premog so bili umerjeni s silo in kotom zlaganja kot odzivnima spremenljivkama.
(2) S sklopljeno metodo MBD-DEM-FEM je bil simuliran realen prehodni odgovor verige in razsutega premoga v primeru, da veriga obtiči in se polomi. Napovedan je bil tudi vpliv okvare na obrabo in na utrujenostno trajnostno dobo verige.
(3) Odvisnosti med velikostjo napetosti in parametri zloma so bile analizirane po metodi odzivnih površin.

Pričujoči članek bo lahko uporaben za simulacije strgalnih transporterjev in mehanizmov okvar ter za optimizacijo konstrukcije verig.

Ključne besede: dinamika več teles, metoda diskretnih elementov, metoda končnih elementov, okvara verige strgalnega transporterja, faktor intenzivnosti napetosti, metoda odzivnih površin

*Naslov avtorja za dopisovanje: Tehniška univerza v Taiyuanu, Kolidž za strojništvo in avtomobilsko tehniko, Tajvan, Kitajska, wxuew@163.com

Strojniški vestnik - Journal of Mechanical Engineering 67(2021)10, SI 64

Prejeto v recenzijo: 2021-05-07
Prejeto popravljeno: 2021-08-30
Odobreno za objavo: 2021-09-07

Preiskava globine prijemanja zob zagozdnega obešala v zaščitne cevi in mehanskih lastnosti zaščitnih cevi pri različnih obesnih obremenitvah v zelo globokih vrtinah

Yong Chen – Jinjin Tan – Guoping Xiao
Jugozahodna univerza za nafto, Šola za strojništvo in elektrotehniko, Kitajska

Namestitveno obremenitev velikih zagozdnih obešal za zaščitne cevi, ki se uporabljajo na naftnih poljih na severozahodu Kitajske, je težko nadzorovati in zato jo je nujno treba pravilno izbrati. Z določitvijo mejne namestitvene obremenitve in z ustreznimi mehanskimi lastnostmi glave vrtine z velikimi zaščitnimi cevmi je mogoče preprečiti porušitev zaščitnih cevi.

Članek obravnava odvisnost med globino prijemanja zob zagozdnega obešala in obesno obremenitvijo obešala tipa WA velikosti Φ273 mm, kot se uporablja na naftnih poljih na severozahodu Kitajske. Odvisnost je bila določena eksperimentalno, s teoretičnimi izračuni in z analizo po metodi končnih elementov.

V članku je bila najprej uporabljena metoda opazovanja oz. opis operativnih težav, ki se pojavljajo na omenjenih naftnih poljih. Nadzorovanje namestitvenih obremenitev postaja vse težje zaradi velikih zaščitnih cevi, ki se vlagajo v vrtine pri globokih nahajališčih nafte. Čezmerna namestitvena obremenitev povzroča težave zaradi pogrezanja glav vrtin in resnih poškodb zaščitnih cevi, ki jih povzročijo zagozde, nezadostna namestitvena obremenitev pa lahko povzroči pomanjkljivo tesnjenje glav zaščitnih cevi.

V nadaljevanju je bila uporabljena raziskovalna metoda za potrjevanje dejstev in oblikovanje raziskovalne teme. Interakcije med zagozdami in zaščitno cevjo ter namestitev obešal za liner povzročijo spremembo porazdelitve napetosti v zaščitni cevi. V zadnjih dveh letih je bilo izvrtanih deset velikih vrtin na globokih nahajališčih in težave so nastopile pri inštalaciji treh glav vrtin.

Članek končno podaja še primerjalno analizo. Primerjava je pokazala dobro ujemanje rezultatov eksperimentov z rezultati numeričnih simulacij po metodi končnih elementov, s tem pa je bila dokazana kredibilnost raziskave.

Študija je pokazala, da so sledovi oprijema vložne zagozde na zaščitni cevi globlji v spodnjem delu. Ko se obesna obremenitev poveča s 1000 kN na 6000 kN, največja globina prijema vložnih zagozd v zaščitni cevi postopoma zrase z 0,07163 mm na 0,3947 mm. Povečanje globine prijema zagozd je večje v nižjih legah (manjše število). Ko se preostala porušitvena trdnost zmanjša na določeno vrednost, je mogoče določiti največjo obešalno silo, ki ustreza globini penetracije vložne zagozde. Na osnovi analize po metodi končnih elementov in izpeljave teoretične enačbe je bila določena porazdelitev napetosti v steni zaščitne cevi z najglobljo sledjo vložne zagozde.

Sila, s katero zobje zagozde delujejo na zaščitno cev, je težko določljiva in se spreminja pri različnih obesnih obremenitvah. To bo tudi predmet prihodnjih raziskav.

Večina objavljenih člankov obravnava predvsem zagozde, praktično nihče pa ni raziskoval delovanja sil na zaščitne cevi. V tej študiji je bila z analizo po metodi končnih elementov in s teoretičnimi izračuni opredeljena odvisnost med globino prijema vložne zagozde in obesno obremenitvijo zagozdnega obešala tipa WA, kot se uporablja na naftnih poljih na severozahodu Kitajske. Določena je bila mejna namestitvena obremenitev za glave velikih vrtin, ki preprečuje porušitev zaščitnih cevi. Izpeljana je bila formula za računanje porazdelitve notranjih napetosti v rizičnem predelu zaščitne cevi, ki bo lahko v pomoč pri projektiranju vrtin in pri obratovanju naftnih polj.

Ključne besede: zagozdno obešalo tipa WE, zaščitna cev, analiza po metodi končnih elementov, globina prijemanja zagozdnega obešala, preostala porušitvena trdnost, obesna obremenitev

*Naslov avtorja za dopisovanje: Jugozahodna univerza za nafto, Šola za strojništvo in elektrotehniko, Kitajska, chyswpu@163.com

Strojniški vestnik - Journal of Mechanical Engineering 67(2021)10, SI 65

Prejeto v recenzijo: 2021-05-06
Prejeto popravljeno: 2021-07-27
Odobreno za objavo: 2021-09-24

Optimizacija parametrov laserske obdelave in geometrije jamic po kombinirani metodi PCA-GRG

Saravanan Kandasamy Ganesan[1] – Thanigaivelan Rajasekaran[2,*]

[1] Tehniški kolidž Sona, Indija
[2] Tehniški kolidž Muthayammal, Indija

Raziskovalci modificirajo površine zlitin za različne aplikacije s pomočjo laserjev. Za optimalen proces laserske obdelave, ki zagotavlja učinkovito in visokonatančno izdelavo mikrojamic, je nujen ustrezen nadzor nad vhodnimi parametri. Čeprav se laserji uporabljajo za modifikacijo površine zlitin, pa ni sistematičnih študij na temo večciljne optimizacije laserskega procesa.

Mikrojamice so bile izdelane na površini jekla SS316L, vplivi dejavnikov laserskega procesa, kot so frekvenca (F), povprečna moč (P) in trajanje impulza (t) na povprečni premer jamic (φ), razdaljo jamic (d) in globino jamic (l), pa so bili preučeni z ortogonalnim poljem (OA) L_9. Optimizacija odgovorov na izhodu laserskega procesa je bila opravljena z analizo variance (ANOVA) in s tehnikami večciljne optimizacije, vključno s sivo relacijsko analizo (GRA) in analizo glavnih komponent (PCA). Parametri laserske obdelave morajo biti optimizirani za dano geometrijo, saj lahko sicer negativno vplivajo na izhodne performanse.

Za material obdelovanca je bila izbrana zlitina SS316L. Uporabljenih je bilo devet preizkušancev dolžine 25 mm, širine 25 mm in debeline 5 mm. V eksperimentih so bili zajeti naslednji faktorji: frekvenca (F) v kHz, povprečna moč (P) v vatih in trajanje impulza (t) v nanosekundah. Vrednosti faktorjev so bile izbrane na podlagi preliminarnih eksperimentov. Za vsakega od faktorjev so bile izbrane po tri stopnje, kot je opisano v preglednici 1. Ortogonalno polje je bilo izbrano glede na prostostne stopnje (DoF). Povprečni premer jamice (φ), razdalja jamic (d) in globina (l) so bili izmerjeni po trikrat.

Mikrojamice so bile uspešno izdelane na površini preizkušancev iz zlitine SS316L. Optimalne nastavitve laserske obdelave mikrojamic, primernih za tribološke aplikacije, so: frekvenca 15 kHz, povprečna moč 12 W in trajanje impulza 1500 ns. Na nastanek mikrojamic imata največji vpliv frekvenca in povprečna moč. Nadzorovani faktorji, ki vplivajo na različne karakteristike delovanja laserskega procesa, si po signifikantnosti sledijo takole: frekvenca, trajanje impulza in povprečna moč. S povečanjem moči laserja se zmanjšajo izhodne performanse.

V prihodnjih študijah bo razvit raziskovalni model za napovedovanje števila mikrojamic na danem območju na osnovi RSM.

Na površini jekla SS316L so bile izdelane mikrojamice, vplivi dejavnikov laserskega procesa, kot so frekvenca, povprečna moč in trajanje impulza na povprečni premer jamic, razdaljo jamic in globino jamic, pa so bili preučeni z ortogonalnim poljem L_9. Performančni kriteriji so bili optimizirani s kombinirano metodo PCA-GRG.

Ključne besede: laser, mikrojamica, analiza glavnih komponent, siva relacijska stopnja, nerjavno jeklo

*Naslov avtorja za dopisovanje: Tehniški kolidž Muthayammal, , Rasipuram, Indija, tvelan10@gmail.com

Strojniški vestnik - Journal of Mechanical Engineering 67(2021)10, SI 66

Prejeto v recenzijo: 2021-05-29
Prejeto popravljeno: 2021-09-29
Odobreno za objavo: 2021-10-01

Karakterizacija mehanskih lastnosti in strukturni atributi biohibridnih kompozitov na osnovi vlaken iz konoplje, bambusa in jute: alternativni pristop k uporabi naravnih vlaken za avtomobilske dele

Rajmohan Bose* – Arunachalam Kandavel
Univerza Anna, Kampus MIT, Indija

V pričujoči raziskavi so bile tri vrste naravnih vlaken iz jute, konoplje in bambusa skupaj s prahom školjčnih lupin in s polipropilensko smolo hibridizirane v biohibridne kompozite.

Obravnavanih je bilo devet preizkušancev z različnimi masnimi deleži bambusa, konoplje in jute. Prešanje je način predelave umetnih mas, pri katerem se vnaprej ogret material dozira v gnezdo odprtega in ogrevanega orodja. Omenjeni kompoziti so bili izdelani s prešanjem naravnih vlaken in polipropilena v razmerju 1 : 4. Kompoziti sestojijo iz 100 gramov vlaken, 400 gramov smole PP in 5 gramov školjčnih lupin v prahu. Opravljena je bila primerjava mehanskih lastnosti devetih preizkušancev, vključno z upogibno, udarno in natezno trdnostjo.

Rezultati so zelo dobri, zasluga za to pa gre predvsem prisotnosti jute in vzorcu polaganja. Preizkušanec št. 9 je namreč poleg 20 % konoplje in 20 % bambusa vseboval tudi 60 % jute, kar je več kot pri ostalih osmih preizkušancih. Natezna trdnost kompozitnega preizkušanca št. 9 je bila za 64,1 % (29,74 MPa) višja kot pri obstoječem materialu (18,1 MPa) in je znašala 47,84 MPa. Upogibna trdnost preizkušanca št. 9 je znašala 239,36 MPa, oz. za 150,96 % več kot pri obstoječem materialu (68,2 MPa). Udarna energija preizkušanca št. 9 je bila petkrat večja (18,33 J) kot pri obstoječem materialu (3,6 J). To pomeni, da lahko material vzdrži nenadne udarce brez deformacij, kar je ključna lastnost za avtomobilske dele. Na preizkušancu št. 9 so bile opravljene tudi morfološke analize, termogravimetrična analiza in analiza po metodi končnih elementov. Z morfološko analizo je bilo raziskano oblikovanje struktur in spajanje materialov na vmesnih ploskvah.

Rezultati SEM kažejo, da na zgornji površini in v notranjih slojih ni votlin, zračnih mehurčkov ali razpok. Zmes smole in vlaken je bila enakomerna pri vseh biohibridnih kompozitih. Preizkušanec št. 9 je bil termogravimetrično analiziran skupaj z obstoječim materialom za določitev masnih izgub pri povišanih temperaturah. Obstoječi material je imel povprečno temperaturo 536,3 °C, preizkušanec št. 9 pa je imel povprečno temperaturo 430,6 °C, kar je za 19,4 % manj kot pri obstoječem materialu.

Zmanjšanje mase je mogoče pojasniti s sestavo kompozita, ki vsebuje vlakna naravnega izvora. Delovna temperatura notranjih in zunanjih delov avtomobilov je nižja od 460,6 °C in material je zato primeren za avtomobilske dele. Primerjava rezultatov eksperimentov z rezultati analize po metodi končnih elementov (MKE) je pokazala dobro ujemanje in odsotnost večjih odstopanj.

Kompoziti z vlakni naravnega izvora, kot so vlakna iz jute, konoplje in bambusa, so glede na rezultate primerni za proizvodnjo različnih avtomobilskih delov. Ti materiali so lahko cenovno ugodni in boljši od obstoječega materiala.

Ključne besede: termogravimetrična analiza, morfološka analiza, juta, konoplja, bambus, analiza po metodi končnih elementov

*Naslov avtorja za dopisovanje: Univerza Anna, Kampus MIT, Indija, rajmohanbose1990@gmail.com

Guide for Authors

All manuscripts must be in English. Pages should be numbered sequentially. The manuscript should be composed in accordance with the Article Template given above. The maximum length of contributions is 12 pages (approx. 5000 words). Longer contributions will only be accepted if authors provide justification in a cover letter. For full instructions see the Information for Authors section on the journal's website: http://en.sv-jme.eu .

SUBMISSION:

Submission to SV-JME is made with the implicit understanding that neither the manuscript nor the essence of its content has been published previously either in whole or in part and that it is not being considered for publication elsewhere. All the listed authors should have agreed on the content and the corresponding (submitting) author is responsible for having ensured that this agreement has been reached. The acceptance of an article is based entirely on its scientific merit, as judged by peer review. Scientific articles comprising simulations only will not be accepted for publication; simulations must be accompanied by experimental results carried out to confirm or deny the accuracy of the simulation. Every manuscript submitted to the SV-JME undergoes a peer-review process.

The authors are kindly invited to submit the paper through our web site: http://ojs.sv-jme.eu. The Author is able to track the submission through the editorial process - as well as participate in the copyediting and proofreading of submissions accepted for publication - by logging in, and using the username and password provided.

SUBMISSION CONTENT:

The typical submission material consists of:

- A **manuscript** (A PDF file, with title, all authors with affiliations, abstract, keywords, highlights, inserted figures and tables and references),
- Supplementary files:
  - a **manuscript** in a WORD file format
  - a **cover letter** (please see instructions for composing the cover letter)
  - a ZIP file containing **figures** in high resolution in one of the graphical formats (please see instructions for preparing the figure files)
  - possible **appendicies** (optional), cover materials, video materials, etc.

Incomplete or improperly prepared submissions will be rejected with explanatory comments provided. In this case we will kindly ask the authors to carefully read the Information for Authors and to resubmit their manuscripts taking into consideration our comments.

COVER LETTER INSTRUCTIONS:

Please add a **cover letter** stating the following information about the submitted paper:

1. Paper **title**, list of **authors** and their **affiliations**. **One** corresponding author should be provided.
2. **Type of paper**: original scientific paper (1.01), review scientific paper (1.02) or short scientific paper (1.03).
3. A **declaration** that neither the manuscript nor the essence of its content has been published in whole or in part previously and that it is not being considered for publication elsewhere.
4. State the **value of the paper** or its practical, theoretical and scientific implications. What is new in the paper with respect to the state-of-the-art in the published papers? Do not repeat the content of your abstract for this purpose.
5. We kindly ask you to suggest at least two **reviewers** for your paper and give us their names, their full affiliation and contact information, and their scientific research interest. The suggested reviewers should have at least two relevant references (with an impact factor) to the scientific field concerned; they should not be from the same country as the authors and should have no close connection with the authors.

FORMAT OF THE MANUSCRIPT:

The manuscript should be composed in accordance with the Article Template. The manuscript should be written in the following format:

- A **Title** that adequately describes the content of the manuscript.
- A list of **Authors** and their **affiliations**.
- An **Abstract** that should not exceed 250 words. The Abstract should state the principal objectives and the scope of the investigation, as well as the methodology employed. It should summarize the results and state the principal conclusions.
- 4 to 6 significant **key words** should follow the abstract to aid indexing.
- 4 to 6 **highlights;** a short collection of bullet points that convey the core findings and provide readers with a quick textual overview of the article. These four to six bullet points should describe the essence of the research (e.g. results or conclusions) and highlight what is distinctive about it.
- An **Introduction** that should provide a review of recent literature and sufficient background information to allow the results of the article to be understood and evaluated.
- A **Methods** section detailing the theoretical or experimental methods used.
- An **Experimental section** that should provide details of the experimental set-up and the methods used to obtain the results.
- A **Results** section that should clearly and concisely present the data, using figures and tables where appropriate.
- A **Discussion** section that should describe the relationships and generalizations shown by the results and discuss the significance of the results, making comparisons with previously published work. (It may be appropriate to combine the Results and Discussion sections into a single section to improve clarity.)
- A **Conclusions** section that should present one or more conclusions drawn from the results and subsequent discussion and should not duplicate the Abstract.
- **Acknowledgement** (optional) of collaboration or preparation assistance may be included. Please note the source of funding for the research.
- **Nomenclature** (optional). Papers with many symbols should have a nomenclature that defines all symbols with units, inserted above the references. If one is used, it must contain all the symbols used in the manuscript and the definitions should not be repeated in the text. In all cases, identify the symbols used if they are not widely recognized in the profession. Define acronyms in the text, not in the nomenclature.
- **References** must be cited consecutively in the text using square brackets [1] and collected together in a reference list at the end of the manuscript.
- **Appendix(-icies)** if any.

SPECIAL NOTES

Units: The SI system of units for nomenclature, symbols and abbreviations should be followed closely. Symbols for physical quantities in the text should be written in italics (e.g. *v*, *T*, *n*, etc.). Symbols for units that consist of letters should be in plain text (e.g. ms^{-1}, K, min, mm, etc.). Please also see: http://physics.nist.gov/cuu/pdf/sp811.pdf .

Abbreviations should be spelt out in full on first appearance followed by the abbreviation in parentheses, e.g. variable time geometry (VTG). The meaning of symbols and units belonging to symbols should be explained in each case or cited in a **nomenclature** section at the end of the manuscript before the References.

Figures (figures, graphs, illustrations digital images, photographs) must be cited in consecutive numerical order in the text and referred to in both the text and the captions as Fig. 1, Fig. 2, etc. Figures should be prepared without borders and on white grounding and should be sent separately in their original formats. If a figure is composed of several parts, please mark each part with a), b), c), etc. and provide an explanation for each part in Figure caption. The caption should be self-explanatory. Letters and numbers should be readable (Arial or Times New Roman, min 6 pt with equal sizes and fonts in all figures). Graphics (submitted as supplementary files) may be exported in resolution good enough for printing (min. 300 dpi) in any common format, e.g. TIFF, BMP or JPG, PDF and should be named Fig1.jpg, Fig2.tif, etc. However, graphs and line drawings should be prepared as vector images, e.g. CDR, AI. Multi-curve graphs should have individual curves marked with a symbol or otherwise provide distinguishing differences using, for example, different thicknesses or dashing.

Tables should carry separate titles and must be numbered in consecutive numerical order in the text and referred to in both the text and the captions as Table 1, Table 2, etc. In addition to the physical quantities, such as *t* (in italics), the units [s] (normal text) should be added in square brackets. Tables should not duplicate data found elsewhere in the manuscript. Tables should be prepared using a table editor and not inserted as a graphic.

REFERENCES:

A reference list must be included using the following information as a guide. Only cited text references are to be included. Each reference is to be referred to in the text by a number enclosed in a square bracket (i.e. [3] or [2] to [4] for more references; do not combine more than 3 references, explain each). No reference to the author is necessary.

References must be numbered and ordered according to where they are first mentioned in the paper, not alphabetically. All references must be complete and accurate. Please add DOI code when available. Examples follow.

Journal Papers:

Surname 1, Initials, Surname 2, Initials (year). Title. Journal, volume, number, pages, DOI code.

[1] Hackenschmidt, R., Alber-Laukant, B., Rieg, F. (2010). Simulating nonlinear materials under centrifugal forces by using intelligent cross-linked simulations. *Strojniški vestnik - Journal of Mechanical Engineering,* vol. 57, no. 7-8, p. 531-538, DOI:10.5545/sv-jme.2011.013.

Journal titles should not be abbreviated. Note that journal title is set in italics.

Books:

Surname 1, Initials, Surname 2, Initials (year). Title. Publisher, place of publication.

[2] Groover, M.P. (2007). *Fundamentals of Modern Manufacturing*. John Wiley & Sons, Hoboken.

Note that the title of the book is italicized.

Chapters in Books:

Surname 1, Initials, Surname 2, Initials (year). Chapter title. Editor(s) of book, book title. Publisher, place of publication, pages.

[3] Carbone, G., Ceccarelli, M. (2005). Legged robotic systems. Kordić, V., Lazinica, A., Merdan, M. (Eds.), Cutting Edge Robotics. Pro literatur Verlag, Mammendorf, p. 553-576.

Proceedings Papers:

Surname 1, Initials, Surname 2, Initials (year). Paper title. Proceedings title, pages.

[4] Štefanić, N., Martinčević-Mikić, S., Tošanović, N. (2009). Applied lean system in process industry. *MOTSP Conference Proceedings*, p. 422-427.

Standards:

Standard-Code (year). Title. Organisation. Place.

[5] ISO/DIS 16000-6.2:2002. *Indoor Air – Part 6: Determination of Volatile Organic Compounds in Indoor and Chamber Air by Active Sampling on TENAX TA Sorbent, Thermal Desorption and Gas Chromatography using MSD/FID.* International Organization for Standardization. Geneva.

WWW pages:

Surname, Initials or Company name. Title, from http://address, date of access.

[6] Rockwell Automation. Arena, from *http://www.arenasimulation.com,* accessed on 2009-09-07.

EXTENDED ABSTRACT:

When the paper is accepted for publishing, the authors will be requested to send an **extended abstract** (approx. one A4 page or 3500 to 4000 characters or approx. 600 words). The instruction for composing the extended abstract are published on-line: http://www.sv-jme.eu/information-for-authors/ .

COPYRIGHT:

Authors submitting a manuscript do so on the understanding that the work has not been published before, is not being considered for publication elsewhere and has been read and approved by all authors. The submission of the manuscript by the authors means that the authors automatically agree to transfer copyright to SV-JME when the manuscript is accepted for publication. All accepted manuscripts must be accompanied by a Copyright Transfer Agreement, which should be sent to the editor. The work should be original work by the authors and not be published elsewhere in any language without the written consent of the publisher. The proof will be sent to the author showing the final layout of the article. Proof correction must be minimal and executed quickly. Thus it is essential that manuscripts are accurate when submitted. Authors can track the status of their accepted articles on http://en.sv-jme.eu/.

PUBLICATION FEE:

Authors will be asked to pay a publication fee for each article prior to the article appearing in the journal. However, this fee only needs to be paid after the article has been accepted for publishing. The fee is 380 EUR (for articles with maximum of 6 pages), 470 EUR (for articles with maximum of 10 pages), plus 50 EUR for each additional page. The additional cost for a color page is 90.00 EUR (only for a journal hard copy; optional upon author's request). These fees do not include tax.

Strojniški vestnik -Journal of Mechanical Engineering
Aškerčeva 6, 1000 Ljubljana, Slovenia, e-mail: info@sv-jme.eu

9 770039 248001
ISSN 0039-2480

http://www.sv-jme.eu

Contents

Papers